Bimodal waveguide interferometer device based on silicon photonics technology for label-free and high sensitive biosensing

Ana Belén González Guerrero

2012

Facultat de Ciencies
Departament de F sica

2012

Research Center on Nanoscience and Nanotechnology (CIN2)
Consejo Superior de Investigaciones Científica (CSIC)

PhD Thesis presented by:

Ana Belén González Guerrero

Ana Belén González
Author

Prof. J. Pascual
Tutor

Prof. L. M. Lechuga Gómez
Director

A mi familia
i a Xavier

Agradecimientos

Esto ya se acaba y hay tanta gente a la que darle las gracias que no se por donde empezar. En primer lugar, agradecerle a mi directora Laura Lechuga que me brindara la oportunidad de realizar esta tesis. Su dedicacion me ha hecho aprender mucho, sobretodo durante las correcciones de los art culos y la tesis. La finalizacion de este trabajo, despues de tantos tropiezos por el camino, es producto de sus empujones en la buena direccion.

En segundo lugar, agradecerle a mi grupo de trabajo los buenos momentos pasados tanto dentro como fuera del lab. Stefaaaaniaaaaaaa; que te voy a decir que tu no sepas; Mar, mi toma de tierra; Borja, frisby, playa, paella; Laurita, te ire a visitar; Daphne, MZI team ; Cesar, un liante, como me recuerdas a mi de joven; Sam, un buen fichaje, Irais; otro buen fichaje; Maria, otra liante; Carmen, Bert y Farina. A los que se fueron: Orlando, ya nadie me dice "Hola mi amol" (bueno, Stefania s , pero con otro acento...); Regatos, ahora los mojitos los hace Xavi, y les echa sal en vez de azucar; Laura F., ahora nunca se que albaran le tengo que dar a quien; Daniel, vuelve pronto. Muchas gracias por vuestro apoyo en todo momento y por los ratos divertidos que nunca podre olvidar. Los que trabajaron conmigo durante sus practicas o trabajos de master: Jay, Adrian y Emma. No solo fue un placer conoceros si no que yo he aprendido tanto de la experiencia como vosotros.

Gracias tambien a toda la gente externa del grupo que ha participado en este trabajo. Kirill, gracias por disenar estos dispositivos magicos y Carlos, gracias por mejorar su fabricacion.

Por supuesto, gracias a mis amigos de toda la vida que han estado conmigo en los buenos y malos momentos: Edu, Eli, Carl, Joan, Jordi B., Jordi A., Natalia, Jonson, Raimon, Alex y Martina. Hace mucho que nos conocemos y espero que sigais a mi lado durante mucho tiempo mas.

Muchas gracias a mi familia por el apoyo recibio y los buenos consejos; papa, mama, Naza y MariJou. Y para finalizar pero no por eso el menos importante; gracies Xavi, ets el millor.

List of publications related with the doctoral thesis

Articles in peer-reviewed international journals

A comparative study of in- ow and micro-patterning biofunctionalization protocols for nanophotonic silicon-based biosensors Ana Belen Gonzalez-Guerrero, Mar Alvarez, Andres Garc a Castano, Carlos Dom nguez, Laura M. Lechuga. Submitted to J. Colloid Interface Sci.

Label-free detection of the human growth hormone at femtomolar level by a nanophotonic silicon biosensor Ana Belen Gonzalez-Guerrero, Jose Miguel Rodr guez-Frade, Mario Mellado and Laura M. Lechuga. Submitted to Anal. Chim. Acta.

Integrated bimodal waveguide interferometric biosensor for label-fee analysis Kirill E. Zinoview, Ana Belen Gonzalez-Guerrero, Carlos Dom nguez and Laura M. Lechuga. J. Lightwave Technol., 2011, 29, 1926-1932.

Nanophotonic lab-on-a-chip platforms including novel bimodal interferometers, micro uidics and grating couplers Daphne Duval, Ana Belen Gonzalez-Guerrero, Stefania Dante, Johann Osmond, Rosa Monge, Luis J. Fernandez, Kirill E. Zinoviev, Carlos Dom nguez and Laura M. Lechuga. Lab Chip, 2012, 12, 1987-1994.

All-optical phase modulation for integrated interferometric biosensors Stefania Dante, Daphne Duval, Borja Sepulveda, Ana Belen Gonzalez-Guerrero, Jose Ramon Sendra and Laura M. Lechuga. Opt. Express, 2012, 20 (7), 7195-7205.

Improved biosensing capability with novel suspendend nanodisks Marinus A. Otte, M.-Carmen Estevez, Laura G. Carrascosa, Ana B. Gonzalez-Guerrero, Laura M. Lechuga and Borja Sepulveda. J. Phys. Chem. C, 115 (13), 5344-5351.

Discriminating the carboxylic groups from the total acidic sites in oxidized multi-wall carbon nanotubes by means of acid-base titration Ana Belen

Gonzalez-Guerrero, Ernest Mendoza, Eva Pellicer, Francesc Alsina, Cesar Fernandez-Sanchez and Laura M. Lechuga. Chem. Phys. Lett., 2008, 462, 256-259.

Assessment of catalyst particle removal in multi-wall carbon nanotubes by highly sensitive magnetic measurements Eva Pellicer, Ana Belen Gonzalez-Guerrero, Josep Nogues, Laura M. Lechuga and Ernest Mendoza. Carbon, 2009, 47 (3), 758-763.

Scalable fabrication of immunosensors based on carbon nanotube polymer composites Ernest Mendoza, Jahir Orozco, Cecilia Jimenez-Jorquera, Ana Belen Gonzalez-Guerrero, Ana Calle, Laura M. Lechuga and Cesar Fernandez-Sanchez. Nanotechnology, 19 (7), 075102.

Articles in peer-reviewed national journals

Towards a complete Lab-On-Chip system using integrated Mach-Zehnder interferometers Stefania Dante, Daphne Duval, Ana Belen Gonzalez-Guerrero, Johann Osmond, Kirill Zinoviev, Borja Sepulveda, Carlos Dom nguez, Laura M. Lechuga. Revista Optical Pura y Aplicada, vol. 45 N2, Special Section: VII Reunion Nacional de Optoelectronica - Optoel'11, 2012.

Conference proceedings

"Advanced photonic biosensors for point-of-care diagnostics", Ana Belen Gonzalez-Guerrero, Stefania Dante, Daphne Duval, Johann Osmond and Laura M. Lechuga. EUROSENSORS XXV, Procedia Engineering, 25, 2011.

Interferometric waveguide biosensors based on Si-technology for point-of-care diagnostic Daphne Duval, Ana Belen Gonzalez-Guerrero, Stefania Dante, Carlos Dom nguez and Laura M. Lechuga. SILICON PHOTONICS AND PHOTONIC INTEGRATED CIRCUITS III, Proceedings of SPIE, 8431, 2012.

Silicon photonic based biosensors: the future of lab-on-a-chip diagnostic devices Daphne Duval, Ana Belen Gonzalez-Guerrero and Laura M. Lechuga. IEE Photonics Society Newsletter, 2012, 26 (4), 5-8.

Contents

List of Figures

List of Tables

Motivation, aim, and thesis outline

Conventional diagnostics tests employed in clinical setting suffer from important limitations: usually require labeling of the sample or the reagents and need from bulky instrumentation operated by trained personnel. Although a prompt detection is essential to apply the treatment in the early stages of the disease, analytical methodologies are laborious, expensive, and time-consuming which hinder the access of the patient to an effective diagnosis of the illness. Thus, there is a need of developing new ultra-sensitive clinical tools able to provide a label-free and real-time detection, opening up possibilities to detect the minimum concentrations of a specific clinical biomarker by a user-friendly analysis in a short turnaround time.

In this context, the interest of the scientific community for the development of novel biosensor devices has witnessed an impressive increase over the years. Biosensors meet the appropriate features to replace current detection methodologies as clinical diagnostics tools. In particular, photonic biosensors enable the real-time detection by using a label-free scheme. Among them, interferometric transducers have demonstrated the highest sensitivity, thereby meeting together all the desired characteristics to become an extremely efficient biosensing device. Moreover, they can be miniaturized which entails several advantages such as; i) the mass-production of the sensor by standard microfabrication techniques which significantly reduces the cost and ii) the possibility of integrating them in more complex platform called lab-on-a-chip devices, in where the sample handling, the bioreaction, and the signal processing are included.

However, conventional interferometric transducers are based on complex

structures in order to split or recombine the light, the most essential process in order to obtain highly coherent devices. Therefore, these devices usually evidence a poor reproducibility which hinder in their commercialization and translation to the clinic environment.

This PhD thesis presents the research efforts towards the development of a novel interferometric device able to carry out high-sensitive and high-performance detections. Then, the presented work focuses on the development, characterization, and evaluation as biosensor of a new straight-waveguide interferometric transducer based on two-mode interference. To achieve this purpose, the following objectives have been pursued:

1. Design, fabrication, and optical characterization of the transducer.
2. Development and optimization of biofunctionalization strategies to anchor the bioreceptor layer on the transducer surface.
3. Evaluation of the transducer operating as biosensor.

This thesis is divided in six chapters outlined below.

The chapter 1 describes the basic concepts that are relevant for this work. The basic types of biosensors are described, with particular attention to the integrated devices based on waveguides.

The second chapter deals with the process of design, fabrication, and optical characterization of the presented device. We present the simulations and optimization of this structure, the microfabrication process to mass-produce the device, and the required pretreatment of the chips. The optical characterization of the BiMW device is also introduced, including the optical set-up and the fluidic system. At last, an evaluation of the bulk and surface sensitivity is provided.

The chapter 3 presents the chemical protocols developed to immobilize the bioreceptor layer on the sensor area surface. We explore the covalent strategy by the use of silane linkers between the silicon surface and the biomolecules. Finally, we demonstrate the covalent attachment of the bioreceptor molecules to the sensor area of the surface by the analysis of the real-time interferometric signals.

The chapters 4 is devoted to the use of the device as label-free biosensor. We investigate the detection limits of the device for proteomics applications, the detection of the human growth hormone (hGH) and the microorganism detection.

Chapter 5 investigates the genomic applications of the device to the detection of the fas gene, involved in the programmed cell-death routes related with the carcinogenesis process. These chapters are divided in an introduction explaining the state-of-the-art of the detection of the corresponding analyte, followed by a description of the methods used, and finally, the results obtained.

In chapter 6, we present a future look at the integration of the device in a complete LOC by the implementation of the grating couplers, the phase modulation, and the microfluidic system.

Chapter 1

Introduction

> "The future belongs to those who believe in the beauty of their dreams."
>
> Eleanor Roosevelt

1.1 Biosensors

1.1.1 De nition and classi cation

The International Union of Pure and Applied Chemistry (IUPAC) defines biosensor as a device that uses specific biochemical reactions mediated by isolated enzymes, immunosystems, tissues, organelles, or whole cells to detect chemical compounds usually by electrical, mechanical, or optical signals [1]. Therefore, a biosensor is a compact device incorporating a biological receptor integrated within or intimately associated with a physicochemical transducer or sensor as illustrated in Figure 1.1. The biological element linked on specifically recognizes a substance (chemical or biological) in a sample, inducing a change in the transducer which produces either discrete or continuous digital electronic signals, that are proportional to the concentration of the analyte or a related group of analytes. When the biospecific interaction takes place, a physicochemical change is induced such as a redox, mass, resonant frequency, absorption, or a refractive index change.

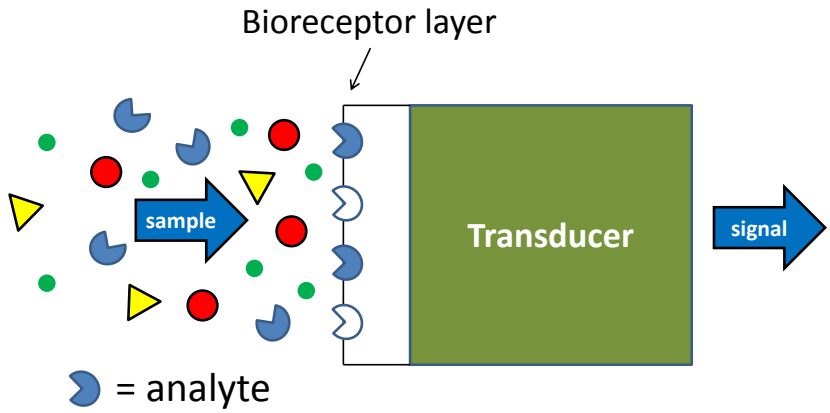

Figure 1.1: Schematic diagram showing the main components of a biosensor; the bioreceptor layer and the transducer.

The ideal biosensor characteristics are exposed as following:

High sensitivity to detect the minimum concentration required by the application.

High selectivity is needed to exclusively detect the compound to be analyzed. This property is achieved by the incorporation of specific biological recognition elements.

A **wide dynamic range** of operation is required to detect in a broad interval of concentration of the analyte.

The **response time** of the biosensor must be short enough to detect the analyte in a direct and fast way. The development of robust systems that allow the detection of the analyte from untreated samples significantly reduces the time of analysis.

Easy to use, the operation of the biosensor must not require skilled personnel.

The **reliability** of the biosensor must assure the performance of its function under stated conditions for a specified period of time. For this reason, the transducer must not be altered and must assure a low-level noise.

The **versatility** of the biosensor by selecting a specific bioreceptor to satisfy a specific analytical problem. Such flexibility makes possible to design the biosensor for the detection of a wide range of analytes.

The capacity of the transducer for **miniaturization** will allow its integration in reduced platforms and the possibility to develop portable systems as well as to work with reduced volumes of sample.

Low cost fabrication of the biosensor, as an important requirement in order to be mass-produced.

In addition to these properties, the **automation** of the systems could allow to incorporate biosensors in automated processes.

The **multiplexing** ability is a desired characteristic to simultaneously detect different analytes from the same sample.

Although the archetypal biosensor must satisfy the maximum number of these requirements, to find current biosensing technologies fulfill all of them is a complex task.

Biosensors can be classified from different points of view of their application, (i.e. in food safety, environmental monitoring, clinical analysis, and medical diagnosis), on the basis of their chemical and biological-recognition element used for sensing (i.e. enzymes, antibody/antigen, nucleic acids and whole cells), the scheme of the detection (labeled or label-free), or according to mode of physicochemical signal transduction.

Regarding the biodetection, the signal can be obtained by the direct interaction of the bioreceptor with the analyte or by the generation of a product that the transducer can detect due to the recognition event. Depending on that, biosensors can be generally divided into two main types: catalytic biosensors and affinity biosensors [2].

In **catalytic biosensors**, the bioreceptors are able to recognize (bio)chemical species and to transform them into a product. Such is the case of the enzymes, cellular organelles, entire cells, or tissues that catalyze chemical reactions by increasing its rate. Thus, the analyte is transformed into a product mediated by the bioreceptors, such as changes in proton concentration, release or uptake of gases such as ammonia or oxygen, light emission, or heat emission brought by the reaction catalyzed by the enzyme obtaining the signal.

A nity biosensors use the specific capabilities of an analyte to bind to a biorecognition element. Immunosensors (based on specific interactions between an antibody and an antigen) or DNA biosensors (based on the affinity

between complementary oligonucleotide chains) are the main examples of affinity biosensors. Other examples include the use of aptamers, cellular receptors, or microorganisms. In affinity biosensors, the signal is obtained by the direct interaction of the bioreceptor due to induced changes in the optical or electrical properties or a variation in the mass on the surface of the transducer.

Another interesting classification for biosensors can be made by sorting them depending on the general scheme used for the biodetection, the labeled and the label-free.

The **label-based detection methods** are the most employed up to now, consisting in the indirect detection of the biorecognition process between the receptor layer and the analyte by a tag. It is necessary to chemically modify any of the biomolecules (the analyte or the bioreceptor) involved in the interaction. In this scheme, the signal obtained by the biorecognition is given by an enzymatic, radioactive, magnetic, luminescence, or fluorescence label. Although labeling can augment selectivity and enhance sensitivity, labeling of bioreceptor elements can present some issues such as an increase in the complexity and the cost. Moreover, labels can interfere with an assay by perturbing the native interaction of the biospecies through steric hindrance or occlusion of the binding sites.

In the **label-free scheme**, the analyte is detected in a direct way without the need of further modifications. It is evident that label-free detection techniques represent a saving in the quantity of time and cost of the analysis in comparison with labeled techniques. In addition to that, the label-free scheme enables the real-time detection of the binding process. In this way, time averaging of binding/unbinding events can improve measurements accuracy by allowing the determination of affinity constants (by curve-fitting the sensor output vs. time), diffusion rates, and steric hindrances.

The capacity of the sensing system to operate in a label-free scheme is intimately linked to the physico-chemical signal transduction employed. Due to the mentioned improved features, the transducers able to operate in a label-free scheme are attracting increasing attention among the scientific comunity.

1.1.2 The transducer

The transducer element of a biosensor converts the variations of the physical or chemical properties of the biological interaction in a signal that can be analyzed. According with the main employed transducers, biosensors can be divided in: electrochemical, piezoelectric, mechanical, and optical biosensors. Among them, the electrochemical biosensors have experienced the major impact in the market due to their low manufacturing cost and the possibility of being mass-produced. However, the past few years have witnessed impressive progress in the development of optical biosensors mainly due to their superior sensitivity and the possibility of operating in a label-free scheme.

Electrochemical biosensors

An electrochemical biosensor is a device capable of transforming a biological interaction into an electrical signal.The formal definition is that an electrochemical biosensor is a device able to provide specific quantitative or semi-quantitative analytical information using a biological recognition element in contact with an electrochemical transduction element [3]. Typically, in electrochemical sensors, enzymes are used as bioreceptor providing electroactive substances for the detection by the physico-chemical transducer providing the measurable signal (see Figure 1.2). In addition, enzymes can be used as labels bound to antibodies, antigens, and oligonucleotides with a specific sequence, thus providing affinity-based sensors [4]. Based on their operating principle, the electrochemical biosensors can employ potentiometric, amperometric, and impedimetric transducers converting the chemical information into a measurable amperometric signal. Among the different sensors, electrochemical biosensors are the most common in the clinical field, due to their high sensitivity and selectivity, portability, rapid response time, and low cost. Nevertheless, the high sensitivity is mostly based on the amplification of enzyme label of either antibody or antigen to the immunosensor response which incorporates several pretreatment steps to the sample [5]. Recently, novel nanomaterials such as the carbon nanotubes have been employed as transducer surface for electrochemical biosensors due to their exceptional physicochemical properties. In this direction, our group has published several works involving the functionalization and the use of carbon nanotubes as electrochemical biosensors [6 8].

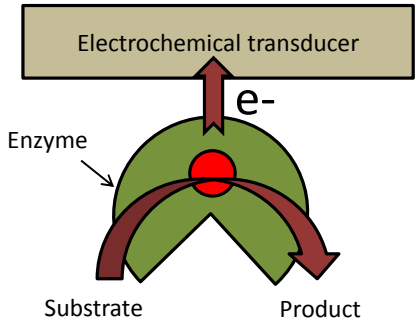

Figure 1.2: Electrochemical transducers based on catalytic recognition.

Piezoelectric biosensors

The piezoelectric effect occurs in crystals without a center of symmetry. In piezoelectric biosensors, this type of crystal is sandwiched between two electrodes and and an alternating electric field is applied. This voltage leads to the arising of a dipole moment in the deformed crystal lattice and the physical orientation of the crystal lattice is distorted. This results in a mechanical oscillation of a standing shear wave across the bulk of the quartz disk at a characteristic vibration frequency (i.e. the crystal's natural resonant frequency). Piezoelectric transducers deliver mechanical and electrical forces to a biological medium usually in the form of progressive or standing acoustic waves resulting in a one-dimensional plane-parallel flow velocity profile (see Figure 1.3). When a bioreaction takes place in the surface of the piezoelectric transducer the density, viscosity, elasticity, electric conductivity, or dielectric constant of the sensing element undergo changes, which in turn modify the acoustic field quantities of the acoustic wave transducer enabling the label-free detection. Piezoelectric biosensors have several attractive features such as multi-domain sensing mechanisms, the frequency as an output sensor signal, and good temperature stability. However, due to the mechanical nature of the piezoelectric sensing mechanism (i.e. mechanical/acoustic motion) the enclosure of a biosensor as well sample handling system (like microfluidics) can interfere with the sensing mechanical motion leading to an unfavorable impact of the sensor performance [9].

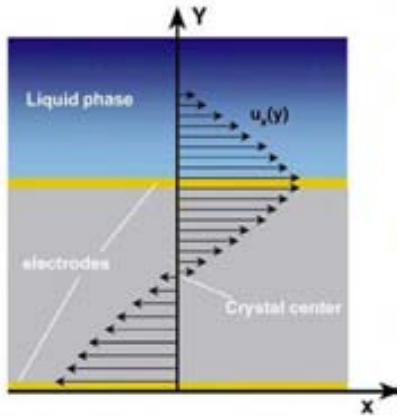

Figure 1.3: Fundamental aspects of quartz crystal sensors: acoustic wave propagating in the fluid.

Mechanical biosensors

Microcantilevers translate molecular recognition of biomolecules into nanomechanical motion that is commonly coupled to an optical or piezo-resistive readout detector system. Most of nanomechanical biosensors measure the difference in surface stress between the opposite sides of the cantilever, which must be different in composition. Thus, molecules will adsorb on each surface differentially, and the difference of surface stresses will be balanced via unequal changes of area of both surfaces giving a cantilever bending [10]. Mechanical sensors achieve high level of sensitivity and are amenable for array multiplexing (see Figure 1.4 B) and its integration in compact platforms without any need for labeling [11]. Moreover, repulsive intermolecular interactions between the bound target molecules and structural changes of the adsorbed biological molecules can affect the surface stress providing extra information about the surface processes. However, most of the existing drawbacks of this transduction technique are related with the necessity of working in liquid environments. The complex relationship between the binding event and the cantilever response, the effect of

the surrounding media on the binding detection (pH or ionic strength changes, damping...), or the sensing layer formation over the cantilever surface (reproducibility, packaging, cleanness...) are some of the current constraints [12].

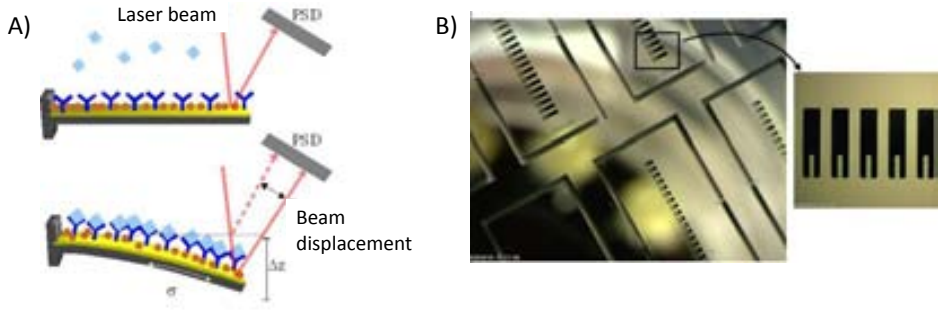

Figure 1.4: Scheme of a mechanical biosensor, A) sensing principle and B) array of cantilevers.

Optical biosensors

In optical biosensors, the biorecognition produces a change in the optical properties of propagated light, such as wavelength, intensity (due to changes in the absorption or dispersion of light), polarization, or phase velocity (changes in the refractive index) [13].

In comparison to electrochemical transducers, optical sensors allow greater sensitivity in a label-free scheme and have a wider dynamic range. Moreover, they have more mechanical stability and are freedom from electromagnetical interferences. Optical biosensors enable the miniaturization of the devices, facilitating their integration in more complex and multiplexed biosensing platforms. For all these reasons, the number of optical biosensor employed for biosensing applications have witnessed a marked increase in the past years in several areas such as environmental monitoring, industrial and food processing, healthcare, biomedical technology, and clinical analysis.

Generally, optical biosensors can be classified in bio-optodes and evanescent wave sensors. In the **bio-optodes**, light is guided to the measurement chamber where the recognition event occurs producing a change in the optical properties of light (absorption, fluorescence, refractive index, bioluminescence,

or dispersion). Usually, optical labels are required in this type of sensors, such as pH or $[O_2]$ sensitive dyes, fluorescence molecules, or bio/quimio-luminescence biomolecules.

The optical transducers based on **evanescent wave detection** consist in structures in which electromagnetic waves can be confined. In this type of sensors, the detection is due to the interaction of the electromagnetic field extending in the external medium with the biomolecular recognition event, allowing high sensitivity and label-free detection.

1.2 Guided-mode evanescent wave biosensors

Depending on the way in which the evanescent field modifies the propagated light, the guided-mode evanescent wave biosensors can be classified as linear or nonlinear. In linear sensors, the polarization, the amplitude or the phased of the light are modified. In nonlinear sensors, the guided modes are generated with a wavelength different to the incident light, (e.g. the Raman effect or the luminiscence).

In a linear sensor, the analyte interacting with the transducer surface induces a change in the refractive index of the external medium. When the change affects the totality of the evanescent field, it is named a change in the bulk refractive index. However, the variation of the refractive index can be produced in a small region affecting only partially the evanescent field, named change in the surface refractive index. This is due to the deposition of molecules of nanometer size with a refractive index on the core surface. There are two different types of linear sensors depending on the way of modifying the refractive index. In adsorption sensor, the change is produced in the imaginary part of the refractive index inducing a modification of the light intensity at the end of the device. If the change is produced in the real part of the refractive index, a variation in the propagation velocity of the guided light is produced, or in its effective refractive index. In order to measure the variation in the propagation velocity of the guided light different devices have been developed, described as following. Previously, the terminology employed to compare the sensitivities of the different sensors is presented.

Terminology

Specifically for optical biosensors based on guided modes, the limit of detection (the minimum concentration of a measurand which is detectable, LOD) can be determined by: (i) according to the bulk sensitivity (expressed as refractive index units, RIU). This LOD is dependent not only on the sensor, but also on the noise of the system. The signal to noise ratio (SNR) is related to the type of sensing modality and the environment around the sensor; (ii) according to the surface sensitivity, which is an evaluation of the real biosensing capabilities of a transducer, normally expressed as surface mass density (pg/mm^2). The detection limit can also be expressed as analyte concentration (i.e. in ng/ml or molarity), but this value is not directly comparable among different sensors since it will depend on the target molecule and its affinity constant. The best resolutions for bulk refractive index changes (bulk sensitivity) are within the range of 10^{-5} to 10^{-8} RIU, which depending on the analyte and transducer mechanism means that concentrations down to ng/ml or pg/ml can be determined.

1.2.1 Surface Plasmon Resonance Sensors

Surface plasmon resonance biosensor is the most employed evanescent wave biosensor for label-free analysis in areas such as environmental monitoring, drug discovery, and biomedical research. Several commercial SPR have been launched in the last decades, the first one was Biacore currently commercialized by GE Healthcare. Nowadays, different companies such as Xan Tec bioanalytics, Horiba scientific, and Mivitecre commercialize the SPR biosensor due to the increasingly widespread use of this device.

Surface plasmon resonance sensors (SPR) measure changes in the refractive index occurring at the interface of a metal film and a dielectric material. A light wave can couple to a surface plasmon at a metal-dielectric interface if the component of light's wavevector that is parallel to the interface matches the propagation constant of the surface plasmon. The wavevector of light can be increased to match that of the surface plasmon by the attenuated total reflection or diffraction. This enhancement and the coupling between light and a surface plasmon are performed by a coupling device.

The most common coupler devices used in SPR sensor include a prism coupler, a waveguide coupler, and a grating coupler. Prims couplers represent the most frequently used method for optical excitation of surface plasmons. In the

Kretcschmann configuration of the attenuated total reflection method (see Figure 1.5), a light wave passes through a high refractive index prim and is totally reflected at the base of the prism, generating an evanescent wave penetrating a thin metal film. The evanescent wave propagates along the interface with the propagation constant, which can be adjusted to match that of the surface plasmon by controlling the angle of incidence. Thus, the matching condition

$$k = \frac{2\pi}{\lambda} \quad _p \sin \tag{1.1}$$

can be fulfilled, allowing the evanescent wave to be coupled to the surface plasmon. denotes the angle of incidence, n_p denotes the refractive index of the prism, and k denotes the propagation constant of the surface plasmon.

A change in the refractive index of the dielectric gives rise to a change in the propagation constant of the surface plasmon, which through the coupling condition, alters the characteristics of the light wave coupled to the surface plasmon (e.g., coupling angle, coupling wavelength, intensity, phase). On the basis of which characteristic of the light wave modulated by a surface plasmon is measured, SPR sensors are classified as sensors with angular, wavelength, intensity, or phase modulation [14].

This type of sensor can be applied to detect antigen-antibody interactions and DNA hybridization. The possibility of measuring in direct and real-time allows the evaluation of the kinetic of the reaction. Usually, the reported detection limit for bulk changes of refractive index for this device is around 10^{-5}. This sensor is one of the less sensitive guided-mode biosensor as can be checked in Table 1.1, however, due to its robustness and simplicity is the most frequently employed label-free devices to monitor biomolecular interactions.

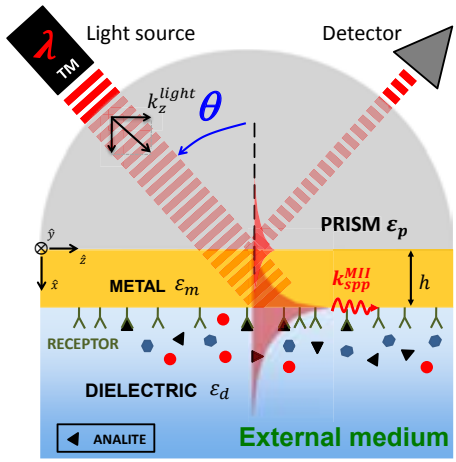

Figure 1.5: Surface plasmon resonance sensing principle by coupling the light by a prism coupler.

Our group developed a 2-channel SPR biosensor based on the Kretcschmann configuration in which the angle modulation is used for biosensing. This device has been successfully employed for several diagnostics applications such as the determination of human growth hormone in serum samples [15] achieving a LOD in the range of ng/ml, the detection of environmental pollutants in river water samples obtaining a LOD of 15 ng/l, and the detection of DNA mutations related with the inherited breast cancer showing LOD of 50 nM. This device is currently commercialized by Sensia.

1.2.2 Grating couplers

Grating-coupled biosensors are one of the first waveguide transducers earlier developed [16]. A grating coupler is a system of periodic disturbance in a planar single-mode waveguide that allows the excitation of a guided mode of the waveguide at a certain angle of incidence when the coupling condition is fulfilled:

$$n_{eff} = C \cdot \sin\alpha + l\frac{\lambda}{\Lambda} \tag{1.2}$$

Where n_{eff} is the effective index of the waveguide, C is the refractive index of the air, α is the angle of incidence of the light, l is the diffraction order, λ is

the wavelength and $\wedge$ is the grating period. As it can be deduced from equation 1.2, the incoupling angle is sensitive to any variation in the refractive index at the surface of the waveguide n_{eff} within the evanescent field region. Therefore, induced changes in the coupled angle can be used for label-free biosensing by evaluating the outcoupling angle of the guided light. The operating principle of the input grating biosensor is sketched in Figure 1.6 in where a collimated laser beam is incident at an angle α onto a waveguide deposited on a substrate. When the coupling conditions are satisfied, the light beam is coupled into the waveguide and propagates.

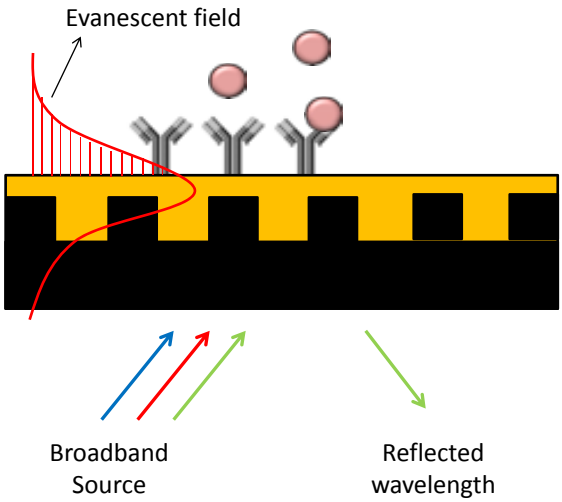

Figure 1.6: Sketch of a grating coupler biosensors sensing principle.

The in- and output grating configurations were initially developed by Nellen and Lukosz in the early nineties, the initial biosensing evaluation was performed using model system as IgG/antiIgG showing moderate sensitivities [16]. A different configuration in which only an input grating coupler is used has been also reported. In this design, the changes in the guided light are detected at the edge of the waveguide [17].

Although this device is suitable for multiplexing and integrating in a biosensing platform, it is relatively insensitive demonstrating bulk refractive index around the 10^{-5} RIU [18], comparable to the SPR sensor. However, due to its

simplicity and the possibility of measuring in a label-free scheme this technology has been commercialized by different companies. For example, MicroVacuum Ltd. launched the OWLS 210 whereas the company axela^x developed the Dotlab R that enables the simultaneous detection of 8 samples. Corning launched the Epic R incorporating a 380 well microplate with a rate analysis of 6 s/microplate.

1.2.3 Ring resonator sensors

In a ring resonator configuration, light is coupled by an input waveguide into a circular waveguide. Coupled light propagates through the loop in the form of whispering gallery modes (WGM) which results from the TIR of the light along the curved surface in such a way that a constructive interference is generated in the multiple round-trips over the ring circumference, considerably enhancing the sensitivity. The WGM is a surface mode, and it circulates along the resonator surface and interacts repeatedly with the analytes on its surface through the WGM evanescent field. Detection in a ring resonator is based on a refractive index change, which is related to the WGM spectral position through the resonant condition:

$$\lambda = 2 \cdot \pi \cdot n_{eff} \frac{r}{m} \tag{1.3}$$

where m is an integer describing the WGM angular momentum, λ is the wavelength, r is the radius of the ring, and n_{eff} is the effective refractive index experienced by the WGM. A change in the effective refractive index of the ring environment (see Figure 1.7 A) shifts the resonance spectrum, which can be monitored by scanning the wavelength or by measuring the intensity profile at a fixed wavelength (see Figure 1.7 B). Contrary to straight waveguides, in ring resonators interaction is no longer determined by the length of the waveguide but rather by the number of revolutions within the ring, which is indicated by the resonator quality factor (Q factor). The effective length (L_{eff}) is related to the Q factor by:

$$L_{eff} = Q \cdot \frac{\lambda}{2\pi n} \tag{1.4}$$

Where λ is the wavelength and n is the refractive index of the ring resonator. High Q factors indicate low optical losses and long photon lifetimes, which is translated into narrow line- widths and high peak resolution (which means a high sensitivity). Relatively high Q factors of 10^6 can be achieved in resonators

of few μm (typically around 50-200 μm), which is equivalent to have planar waveguides of several cm.

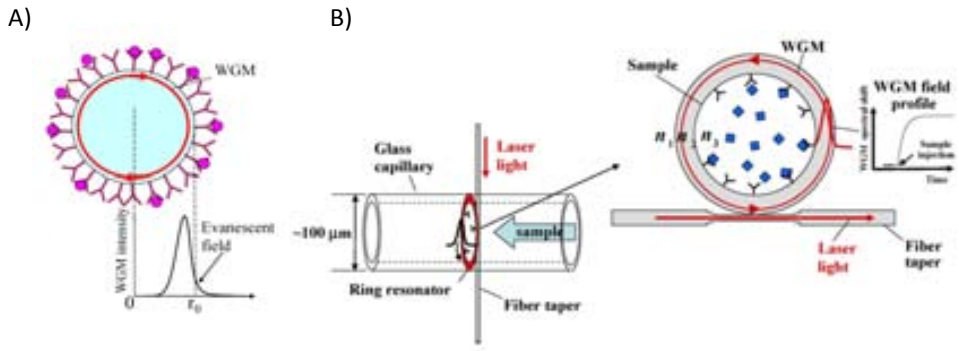

Figure 1.7: Working principle of a ring resonator biosensor: A) evanescent field and B) intensity variation due to a biointeraction.

Ring resonator transducers are increasingly being used for biosensing due to their high sensitivity (that can achieve 10^{-7} RIU for bulk changes of refractive index) and their potential to be produced in highly dense arrays for multiplexed analysis. New types of integrated optical-based resonating structures have being explored for biosensing, as the planar microring resonators based on microdisks [19], microrings [20], or microtoroids [21, 22]. Toroidal-shaped based microcavities offer resolution levels significantly higher than previous structures, since they exhibit ultrahigh Q factors [22] while preserving the same advantages for mass production and integration capabilities as planar ring resonators. Recently, Genalyte has commercialized the Maverick Detection System based on microring resonator array sensors allowing end-point measurements of 96-well plate or 16 real-time detections.

1.2.4 Photonic crystal waveguide sensors

Photonic crystals are well defined nanostructures with periodically repeated variations in the refractive index in one, two, or three orthogonal directions generating one, two, or three dimensional photonic crystals (1D, 2D, or 3D PhC). The lattice structure is generated on the length scale of the light wavelength, which generates photonic bandgaps where light cannot propagate in the

crystal. In this way, light is localized in the region of the linear defect (and its surroundings), leading to an increased interaction with the biorecognition process by the evanescent field. To obtain a high reflection for the light incident of wavelength λ in the interfaces of the periodic structure, the Bragg condition must be fulfilled:

$$m\lambda = 2n_{eff}d \tag{1.5}$$

where m is the diffraction order, λ the wavelength of the reflected light, n_{eff} the effective refractive index of the periodic structure, and d the lattice period of the crystal in the direction of propagation of light.

Cunningham's Group has pioneered the development of bulk photonic crystal based biosensors. For these structures, a variation of the refractive index of the surrounding medium provokes a shift of the position of the photonic bandgap (PBG) edge, which is used to perform the sensing. However, in this configuration, light is not well localized on the in-plane direction of the structure. To solve this problem, linear or punctual defects are introduced on the bulk structure to enhance the localization of the optical field in the active region. The position of the guided band edge (either lower band edge or upper band edge) is used for sensing, as it is dependent on the refractive index variations of the surrounding media. For photonic crystal cavity based sensors, a punctual or area defect is created in the bulk photonic crystal, leading to the formation of a resonator with a strong localization of the optical field within this region. In this direction, most of the work is focused on hole-array PhC as showed in Figure 1.8 A.

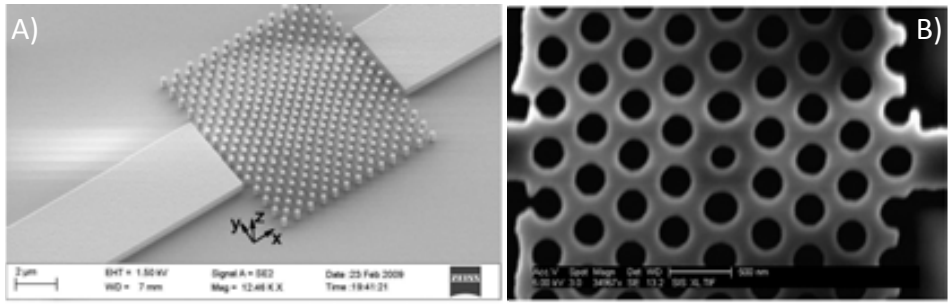

Figure 1.8: SEM micrographs of A) a heterogeneous pillar-array microcavity [23] and B) photonic crystal microcavity sensor showing input and output ridge waveguides [24].

They still remain as a promising type of transducers due to present moderate sensitivities (10^{-5} RIU) as compared with other label free photonic sensors. Better features could be achieved by optimizing the crystal and defect dimensions and also by positioning the bioreceptor only in the holes (by controlled immobilization) where the confinement is maximum, therefore resulting in highest resonant shifts. In fact, a growing number of examples are appearing in the literature focused on single particle detection by trapping them at the holes; single virus or small pathogens could be detected in this way [25 27]. SRU Biosystems, Inc. has developed the BIND® Biosensor, based on the use of photonic crystals in a grating configuration. The platform offers high multiplexed capabilities for end-point detection in a microplate format (up to 1536 wells).

1.2.5 Interferometric waveguide sensors

In the interferometric waveguide sensors, an interference pattern is created when two or more light waves that travels confined in a waveguide are superimposed. The different velocities of the light waves, due to the different interactions of their evanescent field with the external medium, can be studied by the analysis of this interference pattern, and correlated with the processes occurring at the external medium (i.e., a biological interaction or a change in the bulk refractive index of flowing solutions). Mach-Zehnder (MZI) and Young (YI) interferometers as well as dual polarization (DPI) are the most usual interferometric configurations based on waveguides employed for biosensing.

In the integrated version of a **Mach-Zehnder Interferometer** (MZI), an input optical waveguide supporting a single-mode of light is split into two arms (the sensing and the reference) by a Y-junction. After a certain distance, the two arms are recombined again in an output optical waveguide (see Figure 1.9 for general structure). In the sensing arm, the protective layer is opened exposing a portion of the core to the external medium, the sensor area. When a biological interaction is occurring on the sensor area, the variation in the refractive index is detected by the evanescent field of light, that cause a variation in the effective refractive index of the waveguide, inducing a phase difference when light is recombined again.

The interferometric modulation at the device output is described by:

$$\Delta\phi = \frac{2\pi}{\lambda} \cdot L \cdot (N_S - N_R) \tag{1.6}$$

$$I_T = I_S + I_R + 2 \cdot \sqrt{I_S \cdot I_R} \cdot \cos[\Delta\phi(t)] \tag{1.7}$$

where E is the electric field propagating along the waveguide, N is the effective refractive index, ϕ is the phase, L is the detection length and λ is the light wavelength. The labels S and R stand for the sensing and the reference arm, respectively. An attractive aspect of this device is the possibility of using long interaction lengths, thereby increasing the sensitivity. The optimization of the signal-to-noise ratio implies maximizing the transfer functions and hence maximizing all partial sensitivities (e.g. $\partial\Delta\phi/\partial N$, etc.) and, at the same time, minimizing all the perturbing effects, e.g. temperature or wavelength drift.

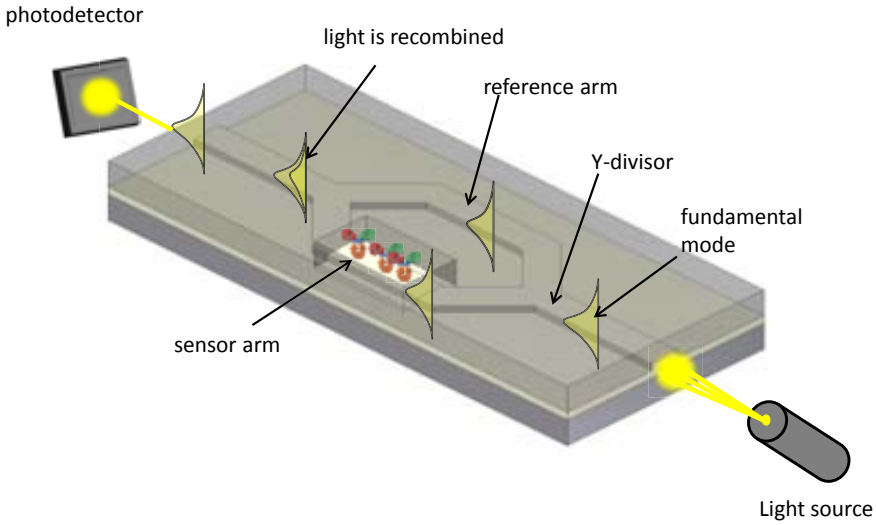

Figure 1.9: Scheme of an interferometer based on Mach-Zehnder configuration.

As can be deduced from equation 2.4, one main drawback of the interferometric sensors is that due to the cosine dependency, the sensitivity will depend on the position of the interferometric curve, with higher sensitivity at the quadrature points and strongly decreasing near the maximum or minimum of the curve

(see Figure 1.10). Modulation system should be an option in order to track the response to the quadrature position.

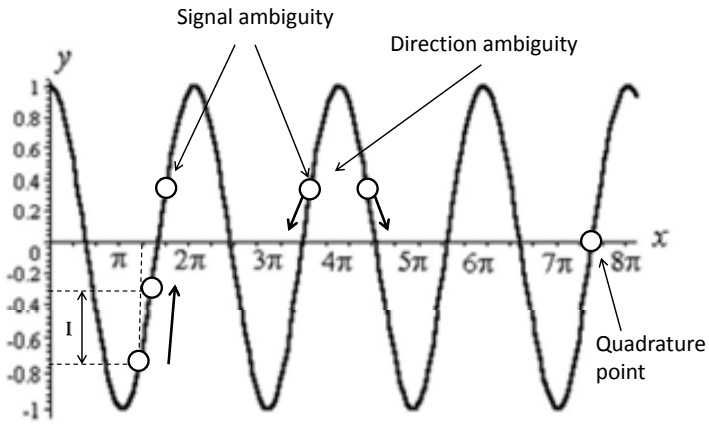

Figure 1.10: Cosine dependence of interferometric signals.

An essential condition of a Mach-Zehnder interferometer for biosensing application is the single mode behavior of the waveguides. Different modes propagate at different velocities in a waveguide involving different evanescent field interactions with the external medium. Hence, if several modes, each one having a different sensitivity, simultaneously propagate in the waveguide, the information carried by them interferes, resulting in an erroneous signal. In addition, for dense packaging of devices or for defining complex devices (such as Mach-Zehnder interferometer), the waveguides must have 2D-confinement; light should remain confined in the cross-section assuring a single mode behavior in both directions.

Our group has developed a biosensor based on a rib-waveguide Mach-Zehnder configuration, the devices are fabricated by silicon-based technology in a Clean Room facilities using standard microfabrication processes at wafer level. Initial works were addressed to optimize the MZI device based on ARROW configuration [28, 29]. In these devices, the optical confinement of light is based on antiresonant reflections rather than total internal reflections; these waveguides exhibited low losses and permitted larger dimensions (micrometers) for

achieving single mode behavior. These features make this technology totally compatible with standard microfabrication techniques which results in highly reproducible devices. However, the sensitivity of the device was low due to the high confinement of the mode within the core, obtaining a LOD of 10^{-5} RIU for bulk changes of the refractive index.

To achiever a higher sensitivity, research efforts were focused on the design of total internal reflection (TIR) devices. Using TIR waveguides in a MZI configuration, the LOD obtained for bulk refractive index were significantly improved obtaining 7 $\times 10^{-6}$ RIU [30]. However, to obtain a single-mode waveguide and a high sensitivity, the rib depth should be around several nanometers and the core thickness of the waveguide of hundreds of nanometers. The drawbacks of the TIR-MZI configuration are related with the reproducibility of this small structures during the fabrication process, specially the Y-junction element, essential to equally divide the input light in each branch of the interferometer.

In **Young Interferometer** configuration, light is confined in a waveguide supporting one mode of light that is split into two arms by an integrated Y-junction acting as a beam splitter. On the contrary that in the case of the MZI, light is not recombined by an output waveguide but the exiting light from both arms is projected onto a CCD camera giving an interference pattern (see Figure 1.11). When a biomolecular interaction takes place on the sensing arm, it induces a variation of the effective refractive index in this arm respect to the reference one ($N_S - N_R$). The phase difference of the two interfering rays is given by:

$$\Phi = \frac{2\pi}{\lambda}\left(\frac{d \cdot x}{f} - (N_S - N_R) \cdot L\right) \tag{1.8}$$

where d is the distance between the two branches, f is the distance between the output sensor and the read-out camera, and x denotes the position on the camera. As an output, the fringe pattern moves laterally. One disadvantage of the YI device is the distance required from the output to the detector to get a maximum resolution. Advantages of the YI include the simplicity of the arrangement, the detection of the complete intensity distribution and the identical length of the arms which avoids side effects arising from temperature and wavelength drifts.

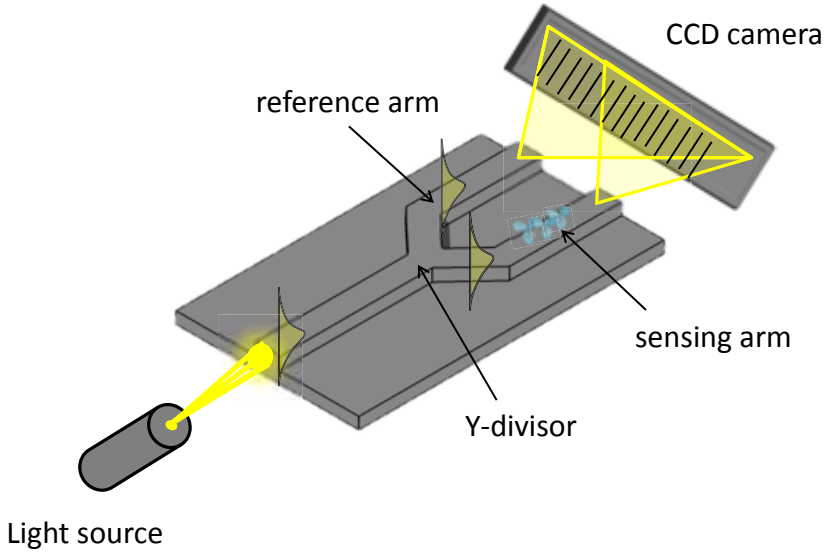

Figure 1.11: Optical arrangement of a Young interferometric biosensor.

Brandenburg et al. [31, 32] developed a free-space YI based on 154 nm thick Ta_2O_5 waveguide with single mode behavior. In this configuration, two separate beams are coupled into the sensing chip via a grating coupler. After propagating through the channels, light from both beams are coupled out by a second grating and diffracted by a double slit. The interference pattern is monitored on a CCD camera. A detection limit based on adsorbed molecules on the surface reached values of 0.75 pg/mm^2 and a resolvable variation of effective refractive index of $9 \cdot 10^{-8}$ RIU [31].

In the **dual polarization interferometry** (DPI), the polarization of the laser is alternated so that two polarization modes of the waveguide are excited in succession to modulate the signal. In applying DPI to MZI or YI configuration, the thickness of the adsorbed protein layer can be calculated.

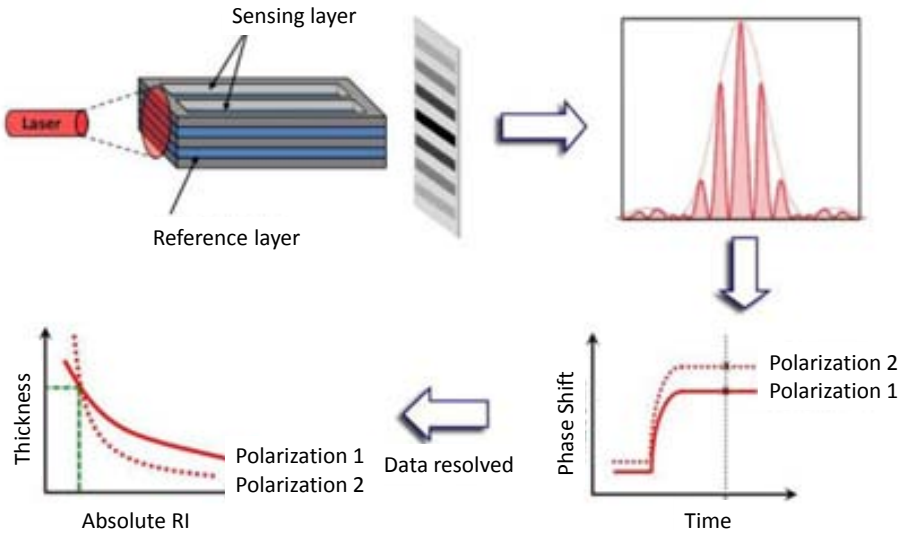

Figure 1.12: Schematic of a dual polarization interferometry sensor chip and the interference pattern produced when light is applied onto the side of a chip. The phase shift of the fringes (TM and TE) is recorded in real-time and data is resolved.

A simple design using DPI and the sensing configuration are sketched in Figure 1.12. This consists of a stack of dielectric layers with reference and sensing layers separated by a layer of cladding that mimics Young's 2-slit experiment [33].

1.2.6 Comparison of the limits of detection for the di erent guided-mode evanescent wave transducers

The interest in the use of optical biosensors based on guided-mode evanescent wave transducers is the result of obtaining high sensitivities in a label-free scheme together with the possibility of miniaturizing the device which facilitate the integration of several of them in a reduced area, allowing the development of multiplexing platforms. Therefore, the choice of a transducer is a key point to obtain a highly sensitive biosensing system. Table 1.1 shows a comparison of the LOD (in RIU and pg/mm^2) for the integrated optical sensors described

in this section. It is largely accepted that interferometric transducers show the maximum sensitivity and among them, Mach-Zehnder and Young interferometer have demonstrated the lowest detection limits. Nevertheless, considering a particular bioapplicaton, the LOD for the analyte is related not only to the transduction principle but to the number of available binding sites, the stability of the linker between the biomolecule and the surface, and the specificity of the bioreceptor layer. Thus, the selection of an appropriate bioreceptor and the development of reliable protocols to immobilize the bioreceptors on the sensor area surface are crucial in the development of an interferometric biosensor for a given application.

1.3 The bioreceptor layer

The most important capabilities that must be into account in the selection of a bioreceptor for a given analyte are: i) the biorecognition element must be high specific toward the analyte, ii) it must have a high affinity for the analyte, ii1) the element must form a reasonably stable complex with the analyte, iv) the interaction event between the element and the analyte must be detectable by the optical transducer, and v) the specificity and affinity of the bioreceptor must not be altered significantly by its immobilization on the surface of the transducer [48].

The most common bioreceptors for optical transducers based on evanescent wave detection are proteins [15], antibodies, or nucleic acids [49]. Due to continuing improvements in the fields of biotechnology, other biological recognition has been engineered such as the aptamers. These recognition molecules are usually nucleic acid sequences that have been engineered through repeated rounds of in vitro selection or equivalently, SELEX (systematic evolution of ligands by exponential enrichment) to bind to an specific target. Aptamers have molecular recognition properties comparable to the antibodies. However, they offer several advantages over antibodies as they can be engineered completely in a test tube and possess desirable storage properties.

An interesting alternative when a recognition element cannot be found with the correct properties is the use of molecular imprinting to form "pockets"' that are highly specific (similar to that of antibody-antigen interactions) [50]. This technique is performed by coating the surface of the transducer with a solution containing both plastic monomers and the measurand and allowing interacting

Table 1.1: Comparison of the limit of detections (LOD) of the different guided-mode evanescent wave biosensors.

Device	Mass detection limit (pg/mm^2)	RI detection limit (RIU)	References
SPR	1-5 [1]	10^{-5} - 10^{-7}	[14]
grating couplers	n.d. [2]	2-5 $\times$ 10^{-6}	[16]
Interferometers			
Mach Zehnder	n.d.	7×10^{-6}	[30]
	0.06	1×10^{-7}	[?]
	0.01 [3]	2×10^{-8} [3]	[34]
	n.d.	9.2×10^{-7}	[35]
Young	n.d.	5×10^{-6}	[36]
	0.75	9×10^{-8}	[31]
	0.013[3]	9×10^{-9}	[37]
	0.02[3]	8.5×10^{-8}	[38]
Hartman	n.d.	10^{-6}	[39]
Dual polarization	0.1	10^{-7}	
Microring resonator	n.d.	10^{-5}	[40]
	3.4 [3]	n.d.	[41]
	15/1.5 [3]	7.6 $\times$ 10^{-7}	[42] [20]
Photonic crystals	0.42	3.4 $\times$ 10^{-5}	[43]
	500	10^{-3}	[44]
	2.1 [3]	6×10^{-4}	[45]
	7.5 [3]	7×10^{-5}	[46]
	1000	n.d.	[47]

[1]averaged [2]n.d. not determined [3]estimated

to create a low-energy network. The coating is polymerized and finally the analyte can be removed by elution, living behind a rigid polymer structure with a template "`pocket"' that can be used to bind the analyte.

1.4 Immobilization of biomolecules on the transducer surface

An immobilization procedure employed in a biosensor device must assure the attachment of the biomolecules to a surface maintaining their three-dimensional structure, functionality, and binding sites to fully preserve its biological activity. Generally, the choice of a suitable immobilization strategy is determined by the physicochemical and chemical properties of both surface transducer and bioreceptor. Several routes can be used to biofunctionalize the sensor surface: (i) physical adsorption by direct deposition of the biomolecule; (ii) self-assembled monolayers, (iii) covalent binding of the biomolecule to the surface (using a cross-linker previously immobilized on the surface or following more complex strategies); (iv) non-covalent interactions to a previously deposited active layer, either by non-specific electrostatic interactions or by non-covalent affinity binding (i.e. biotin-avidin systems, His-Tag systems, Protein A/G for antibodies); (v) physical entrapment in a polymer layer.

Physical adsorption (Figure 1.13 A), is the most simple strategy in which biomolecules are adsorbed on surfaces via intermolecular forces; electrostatic, hydrophobic, and/or polar interactions. However, this strategy suffers from important drawbacks when dealing with biosensors; it can lead to desorption of the active receptors during a flow-through assay and also when high/low pH solutions, high salt concentration, or organic solvents are employed. Additionally, the proximity of the biomolecules to the surface can cause undesired folding of them, and the ensuing loss of its affinity for the antigen.

Self-assembled monolayers can be used to functionalized the transducer surface via amphiphilic molecules that self-organize to form a 2-dimentsional structure. The hydrophilic "`head group"' has a special affinity for the surface while the hydrophobic tail has a functional group that can be attached to the bioreceptor. Monolayers of this type can be formed from heterobifunctional polymers, such as polyethylene glycol (PEG) subunits with different terminations, as well as dendrimer-terminated n-alkylthiols.

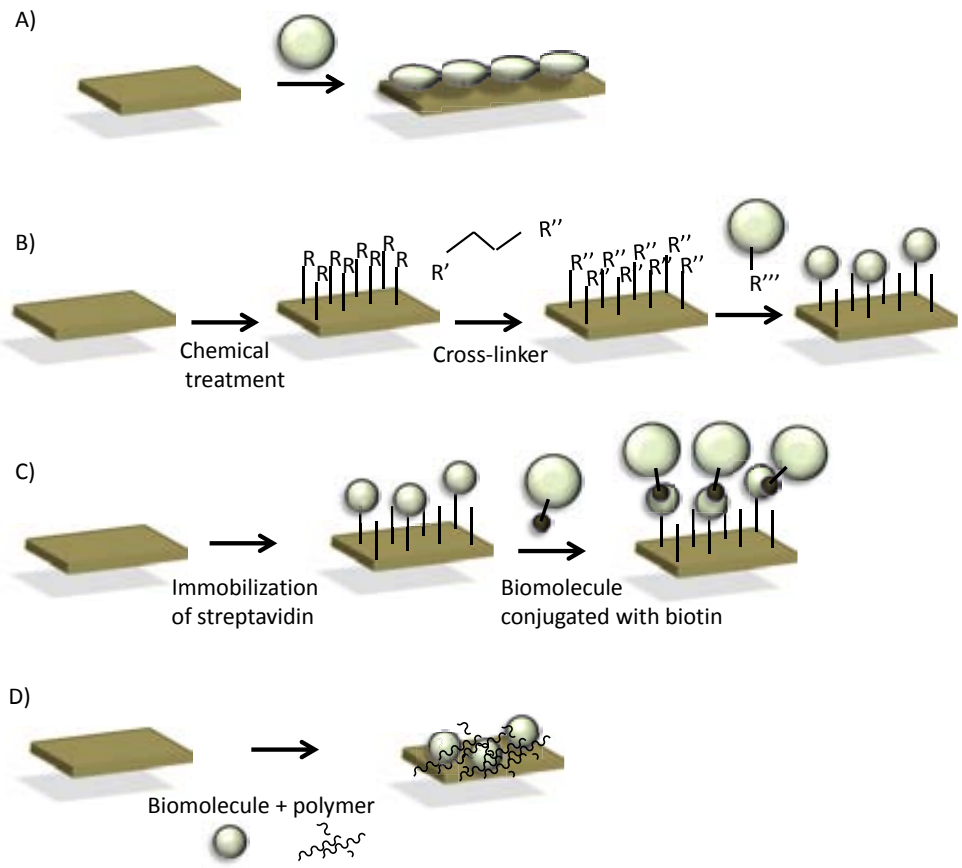

Figure 1.13: Main types of biofunctionalization processes; A) physical, B) covalent, C) bioaffinity immobilization, and D) polymer entrapment (R", R"' = NH_2, SH, COOH)

Covalent binding (Figure 1.13 B) consists in the irreversible binding of the biomolecules to a surface by chemical bonds. To achieve this, the generation of functional groups on the surface is a required task. Following, it is usual the assembly of linker molecules to the surface. In addition to covalently react with the bioreceptor, the linker molecules place the bioreceptor away from the surface avoiding changes in their structure. The most reactive functional groups

in proteins are amine groups from lysine residues, carboxyl groups from aspartic and glutamic acid, and thiol groups from cysteines. These functional groups are used as anchoring points by linker molecules such as succinimide esters or carbodiimides, that at the same time, can be linked to surfaces previously modified with carboxyl, amino, or thiol groups groups. To immobilize nucleic acid, it is possible to take advantage of the versatility of the DNA synthesis which allows the direct incorporation of reactive groups at the end of the sequence.

In all the steps, immobilization efficiency is depending on a number of parameters (i.e. pH, concentration, ionic strength, and reaction time) that must be optimized to obtain the highest yield of bioreceptors on the surface. Much less explored is the photoactive chemistry used to immobilize biomolecules lacking active functional groups. Photoactive reactions can be carried out at mild conditions, independent of pH and temperature, and requires from the presence of heterobifunctional photolinker molecules having one photoreactive group and one chemical reactive group. Click chemistry is an increasingly popular approach to the covalent coupling of recognition elements [51]. It is used to "'click"' the azide-modified recognition element to the alkyne-modified substrate via a cycloaddition reaction. The drawback of this technique is that the recognition element must be modified prior to the attachment. Although, covalent immobilization strategies introduce more steps and complexity than physical adsorption methods, the bioreceptor layers immobilized in this way present a higher stability, allowing harsh temperature, pH, or salt conditions.

By other hand, **non-covalent interactions to a previously deposited layer** will allow the immobilization of bioreceptors in an oriented way (leaving the affinity binding sites free). An example of this is the use of the biotin-avidin system, in which avidin is immobilized on the surface (by physical adsorption or covalent binding) and biotin can be selectively coupled to a region of the bioreceptor not involved in the recognition process (Figure 1.13 C).

Finally, the **physical entrapment** of bioreceptors in a polymer matrix allows the incorporation of guest molecules within the polymer matrix in a single step. This procedure obviates the need for covalent attachment of biomolecules and the inclusion of specific charges on either the biomolecule or polymer surface required for the physical adsorption. The most common polymers as matrices to entrap biomolecules are polyaniline, polythiophene, polypyrrole and its derivatives (Figure 1.13 D).

Bibliography

[1] Milton Abramowitz and Irene A. Stegun. *IUPAC. Compendium of Chemical Terminology.* Blackwell Scientific Publications, Oxford (1997)., 2nd ed. (the "gold book") edition, 2006.

[2] Ed. L. Gorton., editor. *Biosensors and Modern Biospeci c Analytical Techniques.* Comprehensive Analytical Chemistry Series Elsevier Science BV., Amsterdam (The Netherlands), 2005.

[3] D. R. Thevenot, K. Toth, R. A. Durst, and G. S. Wilson. Electrochemical biosensors: recommended definitions and classification. *Biosens. Bioelectron.*, 16:121 131, 2001.

[4] Miroslav Pohanka and Petr Skladal. Electrochemical biosensors principles and applications. *J. Appl. Biomed.*, 6(1):57 64, 2008.

[5] Celine I. L. Justino, Teresa A. Rocha-Santos, and Armando C. Duarte. Review of analytical figures of merit of sensors and biosensors in clinical applications. *Trends Anal. Chem.*, 29:1172 1183, 2010.

[6] Ana Belen Gonzalez-Guerrero, Ernest Mendoza, Eva Pellicer, Francesc Alsina, Cesar Fernandez-Sanchez, and Laura M. Lechuga. Discriminating the carboxylic groups from the total acidic sites in oxidized multiwall carbon nanotubes by means of acid-base titration. *Chem. Phys. Lett.*, 462:256 259, 2008.

[7] Eva Pellicer, Ana Belen Gonzalez-Guerrero, Josep Nogues, Laura M. Lechuga, and Ernest Mendoza. Assessment of catalyst particle removal in multi-wall carbon nanotubes by highly sensitive magnetic measurements. *Carbon*, 47:758 763, 2009.

[8] Ernest Mendoza, Jahir Orozco, Cecilia Jimenez-Jorquera, Ana Belen Gonzalez-Guerrero, Ana Calle, Laura M. Lechuga, and Cesar Fernandez-Sanchez. Scalable fabrication of immunosensors based on carbon nanotube polymer composites. *Nanotechnology*, 19:075102, 2008.

[9] Ryszard M. Lec. Piezoelectric biosensors: recent advances and applications. *IEEE*, 7(1):419 429, 2001.

[10] Mar Alvarez, Ana Calle, Javier Tamayo, Laura M. Lechuga, Antonio Abad, and Angel Montoya. Development of nanomechanical biosensors for detection of the pesticide DDT. *Biosens. Bioelectron.*, 18:649 653, 2003.

[11] L. G. Carrascosa, M. Moreno, M. Alvarez, and L. M. Lechuga. Nanomechanical biosensors: a new sensing tool. *Trends Anal. Chem.*, 25(3):417 423, 2006.

[12] Mar Alvarez and Laura M. Lechuga. Microcantilever-based platforms as biosensing tools. *Analyst*, 135:827 836, 2010.

[13] P. N. Patel, Vivekanand Mishra, and A.S. Mandloi. Optical biosensors: Fundamentals & trends. *JERS*, 1(1):15 34, 2010.

[14] Jir Homola. Surface plasmon resonance sensors for detection of chemical and biological species. *Chem. Rev.*, 108:462 493, 2008.

[15] Juan Trevi no, Ana Calle, Jose Miguel Rodr guez-Frade, Mario Mellado, and Laura M. Lechuga. Surface plasmon resonance immunoassay analysis of pituitary hormones in urine and serum samples. *Clin Chim Acta*, 403:56 62, 2009.

[16] M. Nellen, K. Tiefenthaler, and W. Lukosz. Integrated optical input grating couplers as biochemical sensors. *Sens. Actuators B*, 15(3):285 295, 1988.

[17] Sonia Grego, Jonathan R. McDaniel, and Brian R. Stoner. Wavelength interrogation of grating-based optical biosensors in the input coupler configuration. *Sens. Actuators B*, 131:347 355, 2008.

[18] N. Darwish, D. Caballero, M. Moreno, A. Errachid, and J. Samitier. Multianalytic grating coupler biosensor for differential binding analysis. *Sens. Actuators B*, 144:413 417, 2010.

[19] Shinyoung Lee, Seok Chan Eom, Jee Soo Chang, Chul Huh, Gun Yong Sung, and Jung H. Shin. Label-free optical biosensing using a horizontal air-slot sinx microdisk resonator. *Opt. Express*, 18(20):20638 20644, 2009.

[20] Matthew S. Luchansky, Adam L. Washburn, Teresa A. Martin, Muzammil Iqbal, L. Cary Gunn, and Ryan C. Bailey. Characterization of the evanescent field profile and bound mass sensitivity of a label-free silicon photonic microring resonator biosensing platform. *Biosens. Bioelectron.*, 26:1238 1291, 2010.

[21] Xiaomin Zhang, Hong Seok Choi, and Andrea M. Armani. Ultimate quality factor of silica microtoroid resonant cavities. *App. Phys. Lett.*, 96:153304, 2010.

[22] D. K. Armani, T. J. Kippenberg, S. M. Spillane, and K. J. Vahala. Ultra-high-q toroid microcavity on a chip. *Nature*, 421:925 928, 2003.

[23] Tao Xu, Ning Zhu, Michelle Y.-C. Xu, Lech Wosinski, J. Stewart Aitchison, and H. E. Ruda. Pillar-array based optical sensor. *Opt. Express*, 18(6):5420, 2010.

[24] Sanja Zlatanovic, Laura W. Mirkarimi, Mihail M. Sigalas, Maggie A. Bynum, Edmond Chow, Karla M. Robotti, Geoffrey W. Burr, Sadik Esener, and Annette Grot. Photonic crystal microcavity sensor for ultracompact monitoring of reaction kinetics and protein concentration. *Sens. Actuators B*, 141:13 19, 2009.

[25] Mindy R. Lee1 and Philippe M. Fauchet. Nanoscale microcavity sensor for single particle detection. *Opt. Lett.*, 32(22):3284, 2007.

[26] Sudeep Mandal, Xavier Serey, and David Erickson. Nanomanipulation using silicon photonic crystal resonators. *Nano Lett.*, 10:99 104, 2010.

[27] Mindy R. Lee1 and Philippe M. Fauchet. Nanomanipulation using near field photonics. *Lab Chip*, 11:995, 2011.

[28] F. Prieto, L. M. Lechuga, A. Calle, A. Llobera, and C. Dominguez. Optimized silicon antiresonant reflecting optical waveguides for sensing applications. *J. Lightwave Technol.*, 19(1):75, Jan 2001.

[29] F Prieto, B Sepulveda, A Calle, A Llobera, C Dominguez, and L.M Lechuga. Integrated mach zehnder interferometer based on arrow structures for biosensor applications. *Sensors and Actuators B: Chemical*, 92(1-2):151 158, 2003.

[30] F Prieto, B Sepulveda, A Calle, A Llobera, C Dom nguez, A Abad, A Montoya, and L M Lechuga. An integrated optical interferometric nanodevice based on silicon technology for biosensor applications. *Nanotechnology*, 14:907 912, 2003.

[31] Albrecht Brandenburg, Ralf Krauter, Christa Kunzel, Monika Stefan, and Heinrich Schulte. Interferometric sensor for detection of surface-bound bioreactions. *Appl. Opt.*, 39(34):6396 6405, Dec 2000.

[32] Katrin Schmitt, Bernd Schirmer, Christian Hoffmann, Albrecht Brandenburg, and Patrick Meyrueis. Interferometric biosensor based on planar

optical waveguide sensor chips for label-free detection of surface bound bioreactions. *Biosens. Bioelectron.*, 22:2591 2597, 2007.

[33] Graham H Cross, Andrew Reeves, Stuart Brand, Marcus J Swann, Louise L Peel, Neville J Freeman, and Jian R Lu. The metrics of surface adsorbed small molecules on the young's fringe dual-slab waveguide interferometer. *J. Phys. D: Appl. Phys.*, 37:74 80, 2004.

[34] P. Lambeck. Integrated optical sensors for the chemical domain. *Meas. Sci. Technol.*, 17:R93, 2006.

[35] J. J. Lillie, M. A. Thomas, N. Jokerst, S. E. Ralph, K. A. Dennis, and C. L. Henderson. Multimode interferometric sensors on silicon optimized for fully integrated complementary-metal-oxide-semiconductor chemical-biological sensor system. *J. Opt. Soc. Am. B*, 23:642 651, 2006.

[36] David Hradetzky, Claas Mueller, and Holger Reinecke. Interferometric label-free biomolecular detection system. *J. Opt. A: Pure Appl. Opt.*, 8:S360 S364, 2006.

[37] Katrin Schmitt, Bernd Schirmer, Christian Hoffmann, Albrecht Brandenburg, and Patrick Meyrueis. Interferometric biosensor based on planar optical waveguide sensor chips for label-free detection of surface bound bioreactions. *Biosens. Bioelectron.*, 22:2591 2597, 2007.

[38] Aurel Ymeti, Jan Greve, Paul V. Lambeck, Thisjs Wink, Stepahn W. F. M. van Hovell, Tom A. M. Beumer, Robert R. Wijn, Rene G. Heideman, Vinod Subramaniam, and Johannes S. Kanger. Fast, ultrasensitive virus detection using a young interferometer sensor. *Nano Lett.*, 7(2):394 397, 2006.

[39] Jie Xu, David Suarez, and David S. Gottfried. Detection of avian influenza virus using an interferometric biosensor. *Anal Bioanal Chem*, 2007(2 3):1193 1199, 2000.

[40] Katrien De Vos, Irene Bartolozzi, Etienne Schacht, Peter Bienstman, and Roel Baets. Silicon-on-insulator microring resonator for sensitive and label-free biosensing. *Opt. Exp.*, 15:7610, 2007.

[41] K. De Vos, J. Girones, T. Claes, Y. De Koninck, S. Popelka, E. Schacht, R. Baets, and P. Bienstman. Multiplexed antibody detection with an array of silicon-on-insulator microring resonators. *IEEE Photon. J.*, 1:225, 2009.

[42] Muzammil Iqbal, Martin A. Gleeson, Bradley Spaugh, Frank Tybor, William G. Gunn, Michael Hochberg, Tom Baehr-Jones, Ryan C. Bailey, and L. Cary Gunn. Label-free biosensor arrays based on silicon ring resonators and high-speed optical scanning instrumentation. *IEEE J. Sel. Top. Quant.*, 16(3):654 661, 2010.

[43] Brian Cunningham, Peter Li, Bo Lin, and Jane Pepper. Colorimetric resonant reflection as a direct biochemical assay technique. *Sens. Actuators B*, 81(2-3):316 328, 2002.

[44] D. F. Dorfner, T. Hurlimann, T. Zabel, L. H. Frandsen, G. Abstreiter, and J. J. Finley. Silicon photonic crystal nanostructures for refractive index sensing. *Appl. Phys. Lett.*, 93:181103, 2009.

[45] Jaime Garc a-Ruperez, Veronica Toccafondo, Mar a Jose Banuls, Javier Garc a Castello, Amadeu Griol, Sergio Peransi-Llopis, , and Angel Maquieira. Label-free antibody detection using band edge fringes in soi planar photonic crystal waveguides in the slow-light regime. *Appl. Phys. Lett.*, 93:181103, 2009.

[46] Sudeep Mandal1 and David Erickson. Nanoscale optofluidic sensor arrays. *Appl. Phys. Lett.*, 16:1623, 2008.

[47] Sudeshna Pal, Elisa Guillermain, Rashmi Sriram, Benjamin L. Miller, and Philippe M. Fauchet. Silicon photonic crystal nanocavity-coupled waveguides for error-corrected optical biosensing. *Biosens. Bioelectron.*, 26:4024, 2011.

[48] Heather K. Hunt and Andrea M. Armani. Label-free biological and chemical sensors. *Nanoscale*, 2:1544 1559, 2010.

[49] L. G. Carrascosa, A. Calle, and L. M. Lechuga. Label-free detection of dna mutations by spr: application to the early detection of inherited breast cancer. *Anal Bioanal Chem*, 393:1173 1182, 2009.

[50] Lei Ye and Klaus Mosbach. Molecular imprinting: synthetic materials as substitutes for biological antibodies and receptors. *Chem. Mater.*, 20:859 868, 2008.

[51] Brent S. Sumerlin and Andrew P. Vogt. Macromolecular engineeering through click chemistry and other efficient transformantions. *Macromolecules*, 43:1 13, 2010.

Chapter 2

Design, fabrication, and characterization of a Bimodal Waveguide (BiMW) interferometric device

"Why must our bodies be so large compared with the atom?"

Erwin Schrodinger, What is life?

2.1 Light con ned in material mediums

For the comprehension of lightwave propagation in optical waveguides, the fundamentals of electromagnetic wave theory must be introduced. The first concept to discuss is the refractive index n of a material; a number that describes how light propagates through this medium. The index of refraction is a value calculated from the ratio of the speed of light in a vacuum to that in a second

medium of greater density [1]. The Snell's law is used to analytically describes the refractive index of a material. It defines the relationship between the angles of incidence and refraction, referring to light or other waves passing through a boundary between two different isotropic media. Snell's law stated that the ration of the sines of the angle of incidence and refraction is equivalent to the ration of phase velocities in the two media, or equivalent to the opposite ration of the refraction index (see Figure 2.1).

$$\frac{\sin\ _1}{\sin\ _2} = \frac{v_1}{v_2} = \frac{n_2}{n_1} \tag{2.1}$$

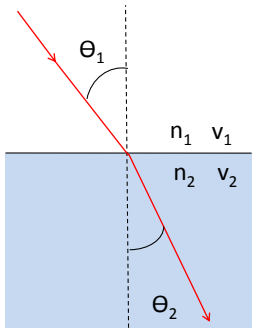

Figure 2.1: Refraction of light at the interface between two media of different refractive index, with n_2 n_1.

2.1.1 Optical waveguide

In an optical waveguide, light is confined in a high refractive index media surrounded by a media with lower refractive indices. A waveguide classification can be done by considering the number of dimensions in which the light is confined. A planar waveguide confines radiation in one dimension while a channel waveguide confines light in two dimensions, and photonic crystals can confine light in three dimensions [2].

The most common structures are shown in Figure 2.2. In a planar waveguide (Figure 2.2 A), light is confined in a film (dashed region) called core, that must have a refractive index higher than the refractive indices corresponding

to the upper and lower media, called claddings. In a channel waveguide, the light propagates within a rectangular channel (dashed region in Figure 2.2 B) embedded in a planar substrate. To confine light in the channel, the refractive index must be higher than of the substrate and the upper medium, that is usually air. Figure 2.2 C shows the geometry of an optical fiber, which can be considered as a cylindrical channel waveguide.

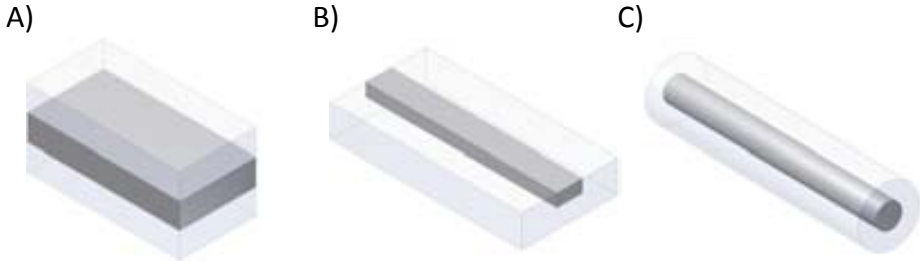

Figure 2.2: Basic waveguides geometry: A) planar waveguide, B) channel waveguide, and C) optical fiber.

In an optical waveguide, the light is usually confined by total internal reflection (TIR). Light incident in the interface between two media with different refractive indexes will be partially reflected and partially refracted (see Figure 2.3). However, when light incidences at a angle larger than a particular critical angle ($_c$) with respect to the normal to the surface, all the light will be reflected suffering TIR at the interfaces and will remain confined inside the film.

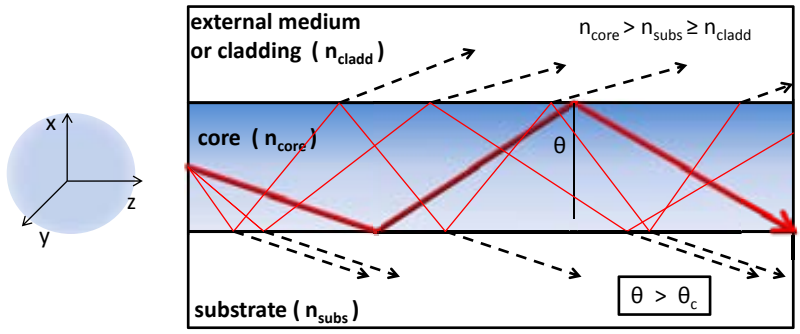

Figure 2.3: Scheme of light confined in a waveguide by TIR.

2.1.2 Maxwell's equation

Light behavior in an optical micron-waveguide must be analyzed by electromagnetic theory. An electromagnetic wave is defined in any point of space and time by the electric field $\vec{E}(\vec{r},t)$ and magnetic field $\vec{H}(\vec{r},t)$ vectors, where $\vec{r}$ is the position vector and t is the time. The behavior of an electromagnetic wave is govern by the Maxwell's equations [3]:

$$\nabla \times \vec{H} = \frac{\partial \vec{D}}{\partial t} \tag{2.2}$$

$$\nabla \times \vec{E} = -\frac{\partial \vec{B}}{\partial t} \tag{2.3}$$

$$\nabla \cdot \vec{D} = 0 \tag{2.4}$$

$$\nabla \cdot \vec{B} = 0 \tag{2.5}$$

where $\vec{E}$ is the electric field strength,
$\vec{H}$ is the magnetic field strength,
$\vec{B}$ is the magnetic flux density,
$\vec{D}$ is the electric displacement,
$\vec{J}$ is the electric current density,
ρ is the electric charge density.

The four basic quantities $\vec{E}$, $\vec{B}$, $\vec{H}$, and $\vec{D}$ are vectors in the three-dimensional space and they are generally functions of both space and time. These fields are

related to the electric field and magnetic field vectors by the constitutive relations, that in a linear medium, are given by:

$$\vec{D} = \varepsilon_0 \varepsilon \cdot \vec{E} \tag{2.6}$$

$$\vec{B} = \mu_0 \mu \cdot \vec{H} \tag{2.7}$$

where ε_0 and μ_0 represent the electric and magnetic permittivity in the vacuum, respectively. The tensors electric permittivity and magnetic permeability, ε and μ, are introduced to describe the electromagnetic properties of the material mediums. Considering $\mu = 1$ for high frequencies such as infrared or visible region of the spectrum and supposing that the fields have a harmonic temporal dependence given by:

$$\vec{E}(\vec{r}, t) = \vec{E}(\vec{r}) e^{-i \ t} \tag{2.8}$$

$$\vec{H}(\vec{r}, t) = \vec{H}(\vec{r}) e^{-i \ t} \tag{2.9}$$

If the constitutive relations are introduced in the equations 2.3 and 2.4 the following expressions are obtained:

$$\nabla \times \vec{H} = -i\omega\varepsilon_0 \varepsilon \vec{E} \tag{2.10}$$

$$\nabla \times \vec{E} = -i\omega\mu_0 \vec{H} \tag{2.11}$$

Moreover if the dielectric tensor does not present spatial dispersion, it is not dependent of position:

$$\varepsilon = \varepsilon(\vec{r}) \tag{2.12}$$

then, equations 2.10 and 2.11 can be combined to obtain the Helmholtz vectorial equations:

$$\nabla^2 \vec{E} + \frac{\omega^2}{c^2} \varepsilon \vec{E} = 0 \tag{2.13}$$

$$\nabla^2 \vec{H} + \frac{\omega^2}{c^2} \vec{H} = 0 \tag{2.14}$$

where c is the light velocity in the vacuum, given by:

$$c = \frac{1}{\sqrt{\varepsilon_0 \mu_0}} \tag{2.15}$$

2.1.3 Light transmission in a waveguide

The solution of the differential equations with the appropriated boundary conditions will provide the field distribution of the electromagnetic modes propagating in a waveguide. First, the simplest case in which the electromagnetic wave is propagating in the z direction where the guide is identical in each direction z and y (plane waveguide) is considered (see Figure 2.3). This allows simplifying the solution of the problem by considering unnecessary the y coordinate. Moreover if all the mediums are isotropic, the dielectric tensor ε can be expressed as a scalar, called dielectric constant. In this case, the following type of solutions can be imposed:

$$\vec{E}(r,t) = \vec{E}(x)e^{i(wt- \ z)} \tag{2.16}$$

$$\vec{H}(r,t) = \vec{H}(x)e^{i(wt- \ z)} \tag{2.17}$$

where β is the propagation constant. By combining these solutions in the equations 2.13 and 2.14, the following equations can be obtained:

$$\frac{\partial^2 \vec{E}(z)}{\partial z^2} + k_0^2(n_i^2 - N^2)\vec{E}(z) = 0 \tag{2.18}$$

$$\frac{\partial^2 \vec{H}(z)}{\partial z^2} + k_0^2(n_i^2 - N^2)\vec{H}(z) = 0 \tag{2.19}$$

In these equations k_o is the wave vector of the electromagnetic radiation in the vacuum, defined as $k_0 = \frac{}{c}$, n_i is the refractive index of the medium ($n_i = \overline{\varepsilon_i}$), whereas N is the effective refractive index, and is defined as $N = \frac{k_x}{k_0}$. It can be also be defined that:

$$k_z = k_0 \overline{n_i^2 - N^2} \tag{2.20}$$

Hence, k_x and k_z represent the components x and z of the wave vector of the electromagnetic radiation. This means that the wave propagation is described inside the XZ plane, being constant along the y direction.

The invariance of the waveguide in the y direction allows uncoupling certain components of the electromagnetic field in the Maxwell equations. This separation will determine the possibility of independent propagation of two polarizations of electromagnetic radiation, named transversal electric (TE) and transversal magnetic polarization (TM).

The electromagnetic modes TE are characterized by having only the y component of the electric field (E_y), meaning that the electric field is perpendicular to the propagation plane of the radiation (the XZ plane). Through Maxwell equations it can be seen that these modes will only present H_x and H_z of the magnetic field as it is shown in Figure 2.4 A. On the other hand, TM modes have the magnetic field perpendicular to the propagation plane which means that only have the component H_y of the magnetic field as is shown in Figure 2.4 B. It can be observed that these modes only exhibit the E_x and E_y components of the electric field. Therefore, in the case of TE modes, only the calculation of E_y is needed while in the case of TM modes, only H_y. The other components can be obtained from Maxwell equations. An additional requirement is that the

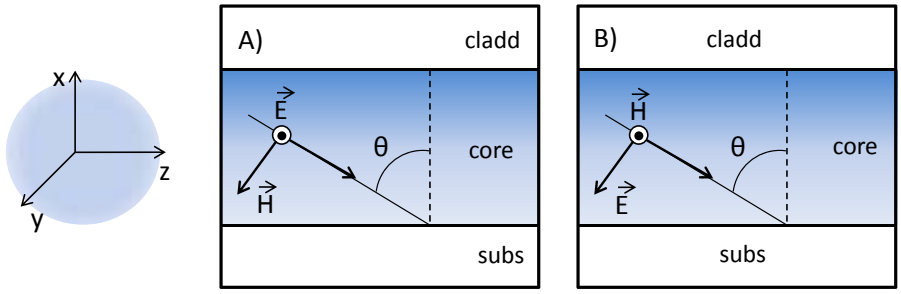

Figure 2.4: Propagation of polarized electromagnetic radiation. A) Transversal electric (TE) and B) transversal magnetic (TM) polarizations.

solutions must obey the continuity conditions from the Maxwell equation. Due to these conditions, the vector of components $\vec{E}(\vec{r},t)$ and $\vec{H}(\vec{r},t)$ parallel to a discontinuity must be continuous. As a consequence, the x and y components must be continuous along the whole structure. Another continuity condition derived from the Snell's law is that the component x of the wave vector (k_x) must be preserved along all the structure.

Now, the illustrated layers scheme (Figure 2.5) in which the core layer has a refractive index higher than the substrate and the external medium will be consider. The solution of the equations will depend on the boundary conditions. In the case of conventional waveguides (composed of dielectric layers) a condition is that the electric fields tend to 0 when the x coordinate tends to $\pm\infty$. With

this boundary condition, the solution of the differential equations 2.18 and 2.19 is going to be formed by a discrete and finite collection of connected solutions and an infinite and continuous collection of free solutions that form the radiative spectrum. Moreover, it can be demonstrated that in the case of isotropic mediums and, in general, for any medium that obey the reciprocity theorem, all these solutions form an orthogonal collection.

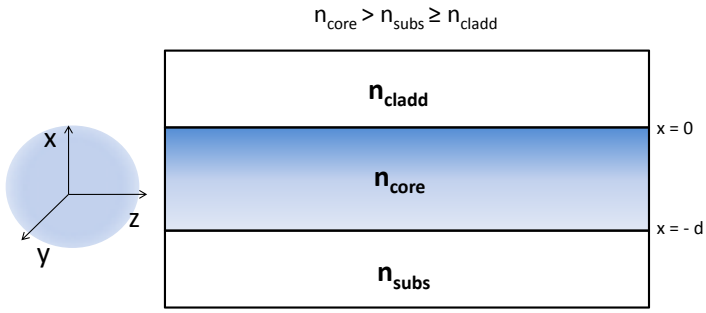

Figure 2.5: Scheme of an optical waveguide.

For the waveguide shown in the figure, plane wave solutions can be imposed as for equation 2.19. For TE polarization and taking into account the boundary conditions, $\vec{E_y}$, $\vec{H_x}$, and $\vec{H_z}$ must be determined. By incorporating equation 2.17 in Maxwell's equations 2.3 and 2.4, the following equations are obtained:

$$\vec{H}_x = -\frac{\beta}{\omega \cdot \mu_0}\vec{E}_y \tag{2.21}$$

$$\vec{H}_z = \frac{i}{\omega \cdot \mu_0} \cdot \frac{\partial \vec{E}_y}{\partial x} \tag{2.22}$$

$$i \cdot \omega \cdot \vec{H}_z + \frac{\partial \vec{H}_z}{\partial x} = -i \cdot \omega \cdot \varepsilon_0 \cdot n^2(x) \cdot \vec{E}_y \tag{2.23}$$

If the components $\vec{H_x}$ and $\vec{H_z}$ from the equations 2.21 and 2.22 are introduced in equation 2.23, an equation that only contains the $\vec{E_y}$ component can be obtained:

$$\frac{\partial \vec{E}_y(x)}{\partial x^2} + [k_0^2 \cdot n^2(x) - \beta^2] \cdot \vec{E}_y(x) = 0 \tag{2.24}$$

where $k_0 = \frac{2}{0}$ and λ_0 is the wavelength of the light in the free space, related with the angular frequency by $\omega = \frac{2 \ c}{0}$. The proposed solution for the wave equation 2.24 contains $\vec{E}_y$ and has the shape:

$$\vec{E}_j(x) = A_j e^{i \ _j x} + B_j e^{-i \ _j x} \tag{2.25}$$

where $\vec{E}_j(x)$ represents the y component of the electric field for the wave propagating in the j region that can be the core, the substrate or the cladding. A_j and B_j are complex constant that could be calculated after including the bondaring conditions. It can be demonstrated that the expression 2.25 satisfies the wave equation 2.24 if $_j$ is given by:

$$_j = \overline{k_0^2 n_j^2 - \beta^2} \tag{2.26}$$

where $_j$ is different for each region and is characterized by the refractive index n_j. The propagation constant β can be related with the effective refractive index by:

$$\beta \quad k_0 N \tag{2.27}$$

According with this definition, the effective refractive index N represents the refractive index that experiences the mode propagating along the z axis. The solutions given by equation 2.25 depend on the refractive index N of the mode and the refractive index n_j of the considered region. Two cases can be found:

> If the propagation constant β is lower that $k_0 n_j$ (o $N < n_j$) then $_j$ is a real number and the proposed general solution in 2.25 corresponds to a sinusoidal function.
>
> On the contrary, if the propagation constant satisfies $\beta > k_0 n_j$ (o $N > n_j$), the parameter $_j$ is a pure imaginary number and then the solution given by 2.25 is described by exponential functions.

If each region of the waveguide must be considered separately, the wave equation for TE modes is given by:

$$\frac{d^2 \vec{E}_y(x)}{dx^2} + [k_0^2 \cdot n^2 - \beta^2] \cdot \vec{E}_y(x) = 0 \tag{2.28}$$

To find the solutions for the guided modes, the propagation constant β associated to a determined mode must satisfy the following condition:

$$k_0 n_{subs} < \beta < k_0 n_{core} \tag{2.29}$$

It means that the refractive index, N, of the guided mode must be comprised between the refractive index of the core and the refractive index of the substrate.

$$n_{subs} < N < n_{core} \tag{2.30}$$

Taking this into account, the wave equation 2.28 can be written for every homogeneous region as:

$$\frac{d^2\vec{E}_y}{dx^2} - \ {}^2_{cladd} \cdot \vec{E}_y = 0 \qquad x \quad 0 \quad (cladding) \tag{2.31}$$

$$\frac{d^2\vec{E}_y}{dx^2} + k^2_{core} \cdot \vec{E}_y = 0 \qquad 0 > x > -d \quad (core) \tag{2.32}$$

$$\frac{d^2\vec{E}_y}{dx^2} - \ {}^2_{subs} \cdot \vec{E}_y = 0 \qquad x \quad -d \quad (substrate) \tag{2.33}$$

where the three parameters $_{cladd}$, k_{core} and $_{subs}$ are given by:

$$\begin{aligned} {}^2_{cladd} &= \beta^2 - k_0^2 n^2_{cladd} && (2.34)\\ k^2_{core} &= k_0^2 n^2_{core} - \beta^2 && (2.35)\\ {}^2_{subs} &= \beta^2 - k_0^2 n^2_{subs} && (2.36) \end{aligned}$$

Solving differential equations from 2.31 to 2.33 and applying the boundary conditions that required that $\vec{E}_y$ and $\frac{dE_y}{dx}$ are continuous at the interface between the core and the cladding or external medium ($x = 0$) and in the frontier core-substrate ($x = -d$), the relation of dispersion or transversal resonance equation is:

$$tan(k_{core}d) = \frac{\frac{_{cladd}}{k_{core}} + \frac{_{subs}}{k_{core}}}{1 - \ \frac{_{cladd}}{k_{core}} \quad \frac{_{subs}}{k_{core}})} \tag{2.37}$$

The equation 2.37 allows a finite number of solutions as the tangent function is periodical for a period of π. It means that the waveguide will support a finite number of guided modes forming an orthogonal base and independently propagating in the waveguide. Considering the planar waveguide of Figure 2.6

where the thickness of the guiding film is in the order of the wavelength of the radiation, the light propagation will be only allowed for a discrete set of angles due to the interference produced by the reflected wave coming from the TIR at the upper boundary and the reflected wave from the lower interface. Light propagating with the same angle is named mode of light, if the dispersion relation only allows one solution, the waveguide is named single-mode waveguide. If the dispersion relation allows two solutions, the waveguide is named bimodal waveguide (see Figure 2.6). It could be possible that the equation will not have any solution (for a given wavelength λ), in this case the guide will not support any mode.

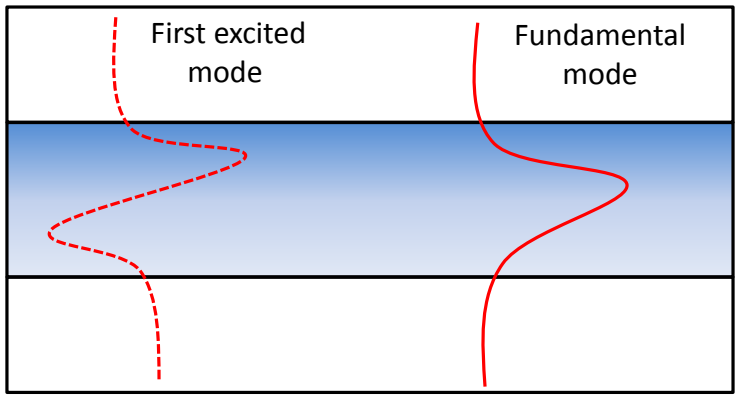

Figure 2.6: Different modes of light propagating in a waveguide: the fundamental and first modes.

The waveguide coefficients $_{cladd}$, k_{core}, and $_{subs}$ will be defined after calculating the propagation constant β for a determined mode. Then, the electric field ($\vec{E}_y$) in the three regions will be determined by:

$$\begin{array}{rll} & A \cdot e^{-\ _{cladd}x} & x \quad 0 \\ A \cdot \ cos(k_{core}x) - \dfrac{cladd}{k_{core}} \cdot sen(k_{core}x) & & -d < x < 0 \\ A \cdot \ cos(k_{core}d) + \dfrac{cladd}{k_{core}} senk_{core}d \ \cdot e^{\ _{subs}(x+d)} & & x \quad -d \end{array} \tag{2.38}$$

Using the same procedure, the solution for the magnetic field (H_y) associated to the polarized TM modes is expressed by:

$$\begin{array}{rll} & A \cdot e^{-\ cladd\, x} & x \quad 0 \\ A \cdot \ cosk_{core}x - \dfrac{n_{core}^2}{n_{cladd}^2}\dfrac{cladd}{k_{core}} & \cdot senk_{core}x & d < x < 0 \\ A \cdot \ cosk_{core}d + \dfrac{cladd}{k_{core}} \cdot \dfrac{n_{core}^2}{n_{cladd}^2} senk_{core}d & \cdot e^{\ subs(x+d)} & x \quad -d \end{array} \tag{2.39}$$

According with this expression the electric field exponentially decreases in the cladding and in the substrate. Inside the core, the electric field exhibits a sinusoidal dependence, as a confined mode. This exponentially decrease and its penetration depth is determined by the parameters $\frac{1}{cladd}$ and $\frac{1}{subs}$. Moreover, for a given mode, the penetration depth in the cladding is smaller than in the substrate due to $n_{cladd} < n_{subs}$ and therefore $cladd > subs$.

This part of the electromagnetic field that travels through a region that extends outward, around a hundred of nanometers, into the medium surrounding the waveguide is named as "evanescent field" (see Figure 2.7). When a receptor layer with a refractive index (n_0) immobilized on the sensor surface interacts with a analyte, the refractive index of the waveguide surface changes (n_0') producing a change in the effective refractive index of the waveguide due to the interaction with the evanescent field. The extent of the change in the refractive index will depend on the concentration of the analyte and on the affinity constant of the interaction, obtaining, in this way, a quantitative sensor of such interaction. The evanescent wave decays exponentially as it penetrates the outer medium, thus, it can exclusively detect changes that take place on the surface of the waveguide due to the intensity of the evanescent field is much higher in this region.

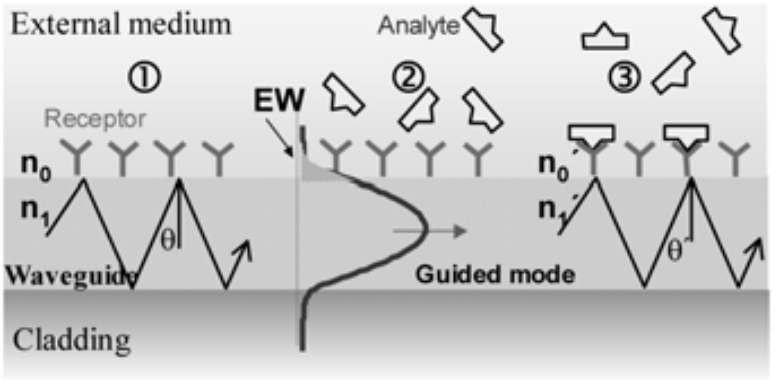

Figure 2.7: Biomolecular interaction sensing by the evanescent wave detection principle in an optical waveguide sensor.

The penetration of the evanescent field can be expressed as [4]:

$$d_{evanescentfield} = \frac{\lambda}{2\pi \sqrt{n_{core}^2 - n_j^2}} \left(\frac{n_j}{n_{core}} \right)^2 \tag{2.40}$$

where j = substrate or cladding and $\rho = 0$ for TE modes and $\rho = 1$ for TM modes.

The waveguide under study is confining the light in one dimension. However, in integrated photonic devices the light usually propagates in channels confined in two spaces dimension. The most common different ways of lateral confining of the light into a channel waveguide are: the stripe waveguide (Figure 2.8 A), the rib waveguide (Figure 2.8, B) and the buried waveguide (Figure 2.8 C). In a channel waveguide, the lateral confinement in the light propagation can be achieved with an increment of the thickness or the refractive index of the core with respect to the adjacent medium [5].

2.1.4 Theoretical analysis of bidimensional waveguides

The design of functional optical waveguides requires accurate tools for their analysis in order to find the propagation constants and field profiles of all the modes that supports. In the waveguides with lateral confinement, the refractive index is a function of the coordinates x and y (n = n(x,y)). Therefore, the

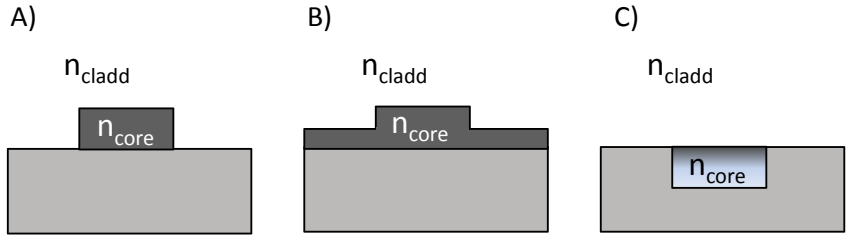

Figure 2.8: Three main types of channel waveguides: A) stripe waveguide, B) rib waveguide, and C) buried waveguide.

modal analysis of these structures entails more complexity than in the case of unidimensional waveguides for which exact closed form solution exist. To treat the modal behavior of light in the 2D waveguides semi-analytical methods are widely used such as the Marcatili, perturvative, variational, or the effective index methods [**?**]. Semi-analytical methods make certain approximations to the structure under consideration and then solve the resulting, simplified problem analytically.

The use of the effective index methods allows a simple and precise solution in the case of rib waveguides when the channel depth is in the order of microns or nanometers, transforming a two-dimensional field problem into a problem for a one-dimensional effective waveguide. In this method, besides of the modal transversal solution, a solution in the orthogonal direction is required. It consists of solving the problem in one dimension, described by the x coordinate, in such a way that the other coordinate (the y coordinate) acts as a parameter. In this way, it can be obtained a y-dependent effective index profile; this generated index profile is considered once again as a one-dimensional problem from which the effective index of the propagating mode can be deduced.

The method involves the division of the bidimensional problem into two unidimensional problems:

1. The waveguide is divided into three regions (see Figure 2.9) that are independently analyzed considering each one as a planar waveguide. The thickness of the core in the region I and III is $(d_{core} - h)$, whereas in the region II is d_{core}.

2. Once the effective refractive index of the regions I and II are calculated (N_I and N_{II}, since $N_{III} = N_{II}$), a planar waveguide structure is formed with a core thickness "w". The effective index of this equivalent waveguide corresponds to the effective refractive index of the rib waveguide.

This approximated method allows calculating the effective refractive index of the light propagating by the rib waveguide.

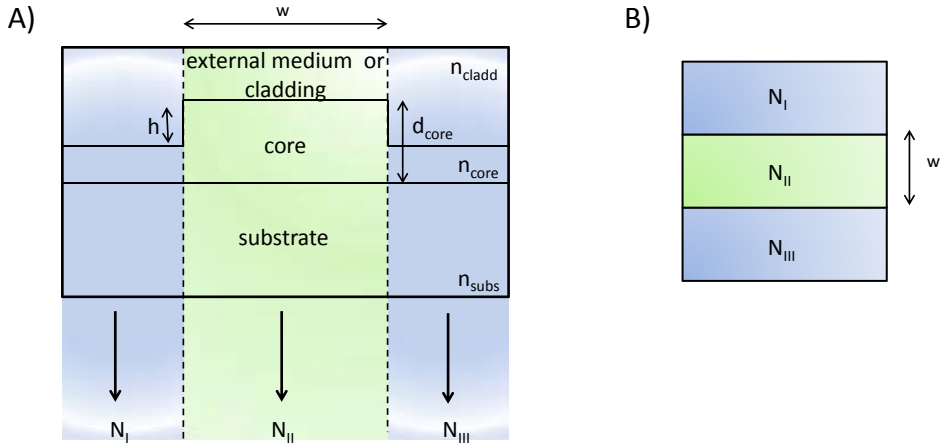

Figure 2.9: Scheme of the refractive index method, A) the structure is divided into three regions treated as independent waveguides and B) an equivalent waveguide is formed using the refractive index obtained.

For a conventional rib waveguide the modal behavior depend on the working wavelength, the thickness of the core, the width and high of the rib, and the contrast of the refractive index between the core and the substrate is defined as:

$$\Delta n = \frac{n_{core}^2 - n_{subs}^2}{n_{core}^2} \tag{2.41}$$

The working wavelength chosen is 632 nm, that is transparent for the biomolecules, and thus, suitable for biosensing purposes. Additionally, this is the wavelength of the commercial He-Ne laser, that can be easily incorporated as light source

in the experimental set-up.

Regarding the thickness of the core and the cladding of the rib waveguides, a waveguide supporting one single mode can be obtained in the following situations:

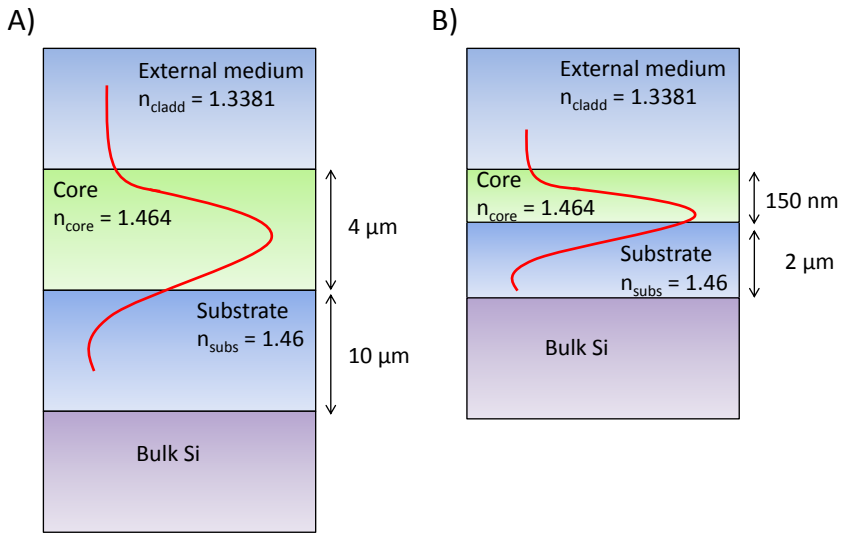

Figure 2.10: Layer structure to obtain a single mode waveguide in the case of A) low index contrast and B) high index contrast.

1. When the index contrast is low (n_{core}-n_{subs} 0.5 %), a single-mode waveguide is obtained using core thickness of several microns. These waveguides have the advantage of having low loses of light when coupling from am optical fiber due to be similar in size. However, the fabrication processes are more complex due to require long times for the growing of the layers that affect the homogeneity of the refractive index. A sketch of a single-mode waveguide with low contrast refractive index is shown in Figure 2.10 A.

2. When the index contrast is high ($\Delta n = 0.1$), the thickness of the layers can be smaller, of the same length that the penetration of the evanescent field.

This implies an advantage from the technological point of view due to a reduction in the fabrication time. However, it is associated to high coupling losses in introducing light in these layers. A sketch of a single-mode waveguide with high contrast refractive index is shown in Figure 2.10 B.

To obtain single mode behavior in the lateral direction, the height and the width of the rib are studied for low and high contrast index. In both cases, the effective index method has been employed to calculate the number of modes supported by varying the width (w) for each value of the height of the rib (h) [6].

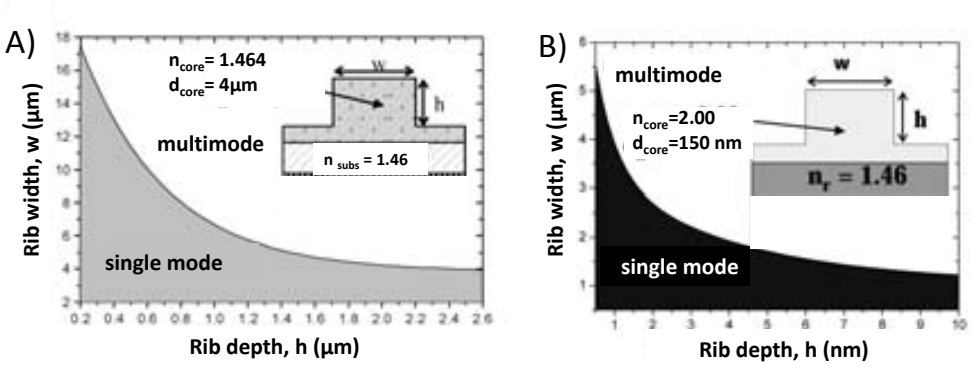

Figure 2.11: Modal behavior as a function of the height and width of the TIR waveguide for a wavelength $\lambda = 632.8$ nm for TE polarization. A) Low index contrast and B) high index contrast waveguides. See inset for the waveguide parameter details.

1. When the index contrast is low (n_{core}-n_{subs} 0.5 %), the height and the width of the rib are in the order of microns. Figure 2.11 A shows the particular case in which the cladding has a thickness of 5 μm and the index contrast is (n_{core} - $n_{subs} = 4 \times 10^{-3}$).

2. When the index contrast is high (n_{core} - n_{subs} 0.1), the depth values for the rib are of few nanometers. In Figure 2.11 B, the thickness core is considered as 150 nm and the index contrast of 0.54. From a technological point of view, the fabrication of a rib of few nanometers adds complexity to the process.

The penetration length of the evanescent field determines the degree of modification of the optical properties of the guided mode, or in its effective refractive index, when a biointeraction occurs on the sensor surface. In this point, the sensitivity can be defined as the refractive index variation of the guided mode produced by a change at the external medium. The transducer must be optimized for maximizing its sensitivity towards the changes to detect. Two different sensitivities can be distinguished depending on the way that the evanescent field senses the change in the external refractive index: the bulk sensitivity and the surface sensitivity, illustrated in Figure 2.12.

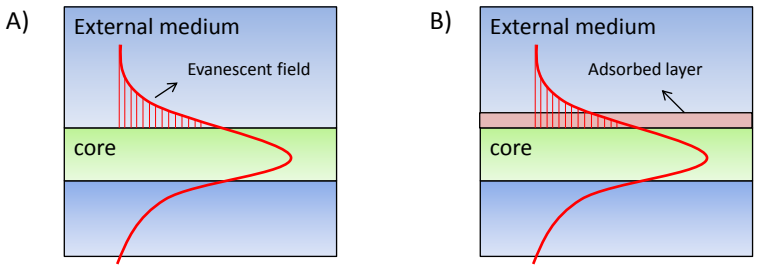

Figure 2.12: Fundamental mode propagating by a TIR plane waveguide to calculate A) the homogeneous sensitivity and B) the surface sensitivity. Note the fraction of the mode traveling through the external medium (the evanescent field).

The bulk sensitivity is obtained when the change of the refractive index is homogeneous in all the region interrogated by the evanescent field. It is defined as the change in the effective refractive index induced by the change in the bulk refractive index of the external medium, n_e:

$$l \quad \frac{\partial N}{\partial n_e} \tag{2.42}$$

If the refractive index variation happens in the core surface, in a region smaller than the penetration depth of the evanescent field in the external medium, it is called surface sensitivity. This is the case when the molecules are adsorbed on the sensor surface or when a biomolecule is detected after immobilizing the receptor layer on the surface. So, the surface sensitivity is defined as the change in the effective refractive index induced by the change in the thickness of a

biomolecule layer, d_l, adsorbed on the waveguide surface.

$$_{surf} \quad \frac{\partial N}{\partial d_l} \tag{2.43}$$

Considering the thickness of a biological receptor layer adsorbed with a refractive index n_l on the waveguide surface, the surface sensitivity is determined by:

$$_{surf} \quad \frac{\partial N}{\partial d_l} = \frac{k_n^2}{k_0^2 d_{ef} N} \frac{\frac{n_l}{n_e}^{2p} \; \frac{2}{e} - \frac{n_e}{n_l}^{2p} \; \frac{2}{l}}{\frac{n_n}{n_e}^{2p} \; \frac{2}{e} + \frac{n_e}{n_n}^{2p} k_l^2} \tag{2.44}$$

In this equation, it is supposed that the thickness of the immobilized biological layer on the sensor surface is much smaller that the wavelength employed. This is a valid condition for the biological reactions, for an example, the thickness of a hybridized DNA layer is about 1 nm and a complex antibody/antigen is about 10 nm, negligible values as compared to 633 nm of the wavelength.

Thus, there is a value of the effective core thickness for which the surface sensitivity take a maximum value [5]:

$$d_{ef\ min} = \frac{0.7\lambda}{\sqrt{n_n^2 - n_r^2}} \tag{2.45}$$

The highest sensitivity levels are reached for a thickness close to the minimum effective thickness. It implies that the surface sensitivity will be higher when the thickness of the core is smaller which corresponds to a high index contrast. In optical waveguides, a large refractive index contrast between the waveguide core material and the cladding material is crucial for enabling strong confinement and large-scale integration of optical components. For sensing purposes, a high index contrast in single-mode waveguides also means that a higher sensing field intensity can be obtained for a given excitation power [7]. Thus, the choice of the material for the waveguide fabrication is an important issue as its refractive index determines the evanescent field and hence, the sensitivity.

2.1.5 Materials for the fabrication of optical waveguides

The substrates most commonly used for the fabrication of optical waveguides are glasses, lithium niobate, silica on silicon, III-V semiconductor compounds, and polymers [2]. The methods most widely used in the definition of optical

waveguides over a substrate are deposition and diffusion techniques.

The **glass-based integrated optical devices** have the great advantage of the low cost of the starting material. The method used for producing waveguides in glass substrates is the exchange of alkali ions from the glass matrix (usually Na^+ ions) for monovalent cations such as K^+, Ag^+, Cs^+ or Tl^+. The refractive index increase due to the ionic exchange typically varies in the range 0.01 to 0.1 which implies a low index contrast, unsuitable for biosensing.

One of the materials most widely used in the fabrication of integrated optical devices is **lithium niobate ($LiNbO_3$)**. It has interesting characteristics due to the advantage of the control of the light due to its valuable acousto-optic, electro-optic, and piezo-electric effects. The techniques for waveguide fabrication in $LiNbO_3$ are based on metallic diffusion, protonic exchange, or even ion implantation. The resulting waveguides have very low losses but the index contrast obtained is very low.

The use of **III-V compounds** (mainly GaAs and InP) in integrated optics drives from the fact that they offer the possibility of a high level of monolithic integration. Optical waveguide fabrication is quite straightforward by modifying the dopant concentration during the deposition process. The main problem concerning this technology is the high losses of waveguides made of these materials.

The most used material for biosensing applications is the silicon-based materials; the main advantage of the **silicon-based photonic waveguides** is the low price and good optical quality of the silicon substrates. Moreover, it takes benefit of the widely developed experience of micro-electronic technology. Silicon wafers are provided with a silicon dioxide layer by deposition or also by oxidation of the silicon at high temperature. The waveguide core is formed by further deposition of a high index silicon nitride layer usually via the chemical vapor deposition (CVD). The refractive index of the silicon nitride core layer can vary from 1.45 to 2.1, so very high index contrast between the waveguide core and the surrounding media can be obtained. Additionally, silicon microelectronics allows a high homogeneity of the waveguide material and the possibility of final integration in a LOC device taking benefit of the experience in microelectronics and semiconductor technology.

Polymer-based integrated optical devices exhibit some very useful

physical properties, such as electro-optic and non-linear effects. Also, they can be designed with organic groups in the polymeric compound to link biomolecules. However, high index contrast polymers are difficult to obtain.

At the light of these considerations, the use of standard silicon microelectronics is the better option to obtain high index contrast between the cladding and the core. Thus, Si_3N_4 (n = 2) is chosen as core layer for the interferometric device presented in this word and SiO_2 (n=1.46) as substrate and cladding layer. Moreover, Si_3N_4 is not only appropriated as core layer by its high refractive index but also by the chemical properties that it owns such as high density and chemical inertness that make it resistant to ion species, oxygen, and moisture permeation [8] and the possibility of covalently modifying this surface.

2.2 The two-mode interference: the Bimodal Waveguide device

Although the research efforts conducted toward the development of interferometric transducers for diagnosis, these have evidenced a limited translation to clinical environment. Usual interferometric configurations such as the MZI are based on the Y-divisor component to split or recombine light that is an essential process to obtain high performance devices. To obtain a maximum visibility factor (that gives the contrast of the interference signal which means the difference between the maximum and minimum intensity), it is important to design a Y-divisor in where input light will be equally divided in each branch of the interferometer. Moreover, propagation losses in the sensor and reference arm should be identical [7]. Unfortunately, standard microfabrication techniques are not capable to provide the reproducibility required for the effective production of this splitter element.

Thus, the design and development of a new interferometric configuration overcoming these problems would constitute a milestone in the field of label-free biosensors. In this direction, we have developed a simpler configuration using a single waveguide where two modes of the light interfere, so-named bimodal waveguide interferometer (BiMW) [9, 10]. Figure 2.13 shows both interferometric configurations; Mach-Zehnder and BiMW, for a direct comparison. It can be observed that the Y-splitter employed in the MZI device (Figure 2.13 A is replaced in the BiMW by a modal splitter consisting in a jump of the thickness of the waveguide core of several nanometers (Figure 2.13 B, a simple process

totally compatible with standard fabrication techniques. The incorporation of the step-junction element leads to obtain an interferometric configuration in a straight waveguide which highly simplify the fabrication, giving rise to more reproducible devices.

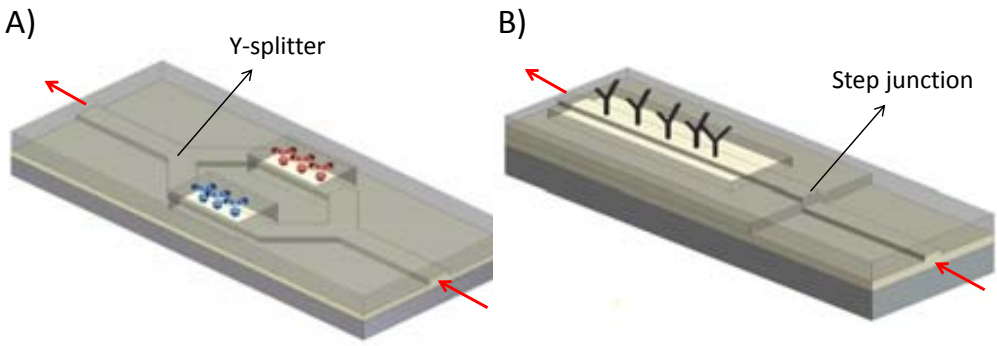

Figure 2.13: Comparison between the different configurations of the Mach-Zehnder interferometer and the Bimodal Waveguide device.

2.2.1 Working principle of a BiMW transducer

In the presented BiMW device, light is confined into a rib waveguide designed to support a single transversal mode. After some distance this fundamental mode is coupled into another rib waveguide which supports two transversal modes. Due to the vertical asymmetry introduced in the junction, the first order mode is excited and both modes (the fundamental and the first order modes) propagate till the output of the chip. A scheme of this device is shown in Figure 2.14.

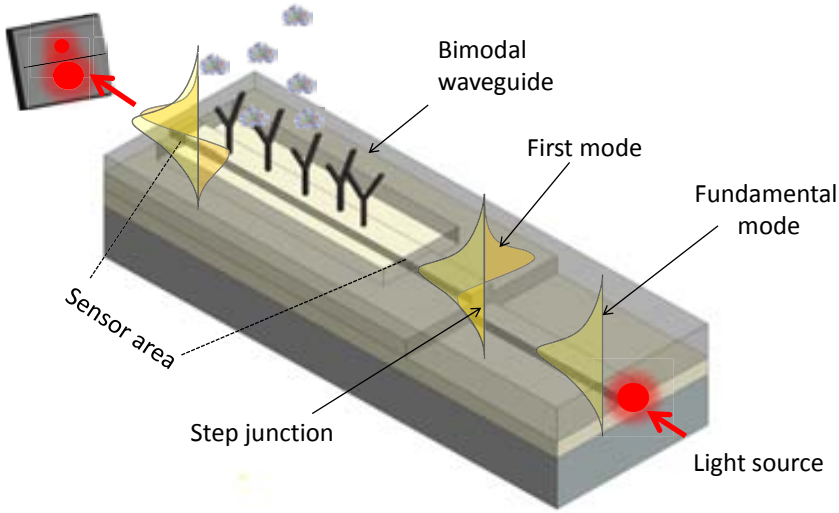

Figure 2.14: Scheme of the BiMW device

The sensing window is opened at the bimodal part of the waveguide to allow the interaction of the evanescent field of the with the external medium. On the sensor surface, a bioreceptor layer with a refractive index n_0 is immobilized. When a biorecognition process occurs in the sensor area of the device, the refractive index of the surface changes (n_0') as it is shown in Figure 2.15. This variation of the external refractive index affects the effective refractive index of the modes (N_{TE0} and N_{TE1}) by the evanescent field of each one.

Due to the different confinement of each mode in the core of the waveguide, they are differently affected by the change in the external refractive index, thus creating an interference pattern at the exit of the waveguide according with the equation 2.46.

$$\Delta\Phi = 2 \cdot \pi \frac{L}{\lambda} \Delta N_{eff} = 2\pi \frac{L}{\lambda} (N_{TE1} - N_{TEO}) \tag{2.46}$$

where L is the length of the sensor area, N_{eff} is the effective refractive index of the waveguide, N_{TE0} and N_{TE1} the effective refractive index of fundamental and first modes respectively, and λ is the working wavelength.

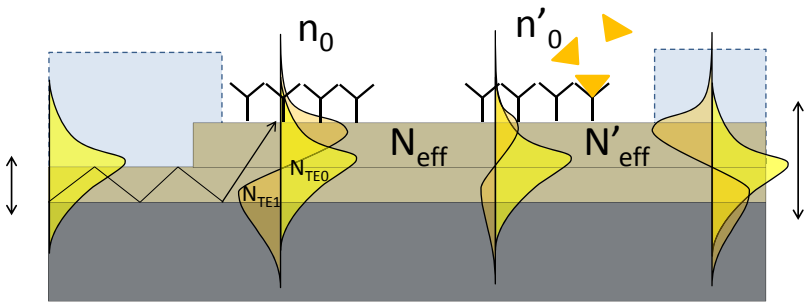

Figure 2.15: Sensing principle of a BiMW biosensor.

The refractive index of a material is highly dependent of the temperature. So, the BiMW device has an intrinsic sensitivity to temperature changes due to the effective refractive index of both modes (N_{TE0} and N_{TE1}) is differently affected. This is a drawback in comparing with the MZI configuration in which the reference arm and the sensing arm are equally affected by a temperature change. However, it can be easily solved by incorporating a temperature controller to the system.

2.3 Design of the device

Due to the 3-dimensional structure of the waveguide constituting the BiMW device, a rigorous analytical calculation is not possible and approximated methods can be used. The device parameters such as materials and thickness of the layers have been chosen to obtain a high contrast in the output signal, by performing numerical simulations. One approach can be found in the transfer matrix approach (TMM). TMM can be used for both evaluation of electric field profile in each layer of the waveguide and for propagation along the structure. The transfer-matrix method is based on the continuity of the electric field across boundaries from one medium to the next, according to Maxwell's equations. The reflection and transmission occurring at each interface are taken into account as matrix coefficients. First, the electric field eigenvalues of each reaction are found as a function of the refractive indexes of each layer ($n_{cladd} = n_{subs} = 1.46$, $n_{core} = 2.00$, $n_{water} = 1.33$) and the thickness, and finally, the reflectivity and transmission coefficients are evaluated for each interface between consecutive sections along propagation direction.

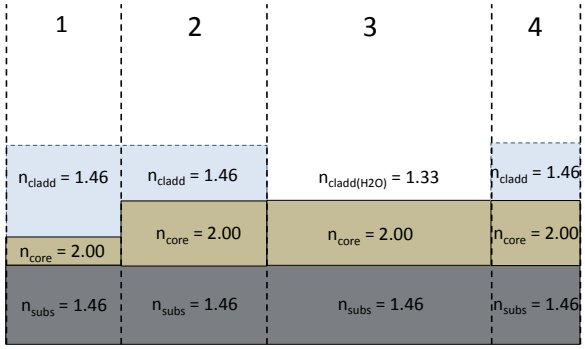

Figure 2.16: Different sections of the BiMW device employed to simulate the profiles of the electric field by the matrix transfer approach.

Using this method, it is possible to simulate the profiles of the electric field in the bimodal waveguide section (see Figure 2.17 A) and the device output as a function of the thickness of the core in the single-mode and bimodal section. By integrating the intensities of the fields at the exit over the upper and the lower half-planes (see Figure 2.17 B), a signal equivalent to the experimentally measured can be plotted. Thus, the modulation of the output signal due to a phase shift of π between modes can be calculated as a function of the thickness of the layers. The thickness of the waveguide core is calculated for obtaining more than 70% modulation, obtaining that the single mode part must have a thickness below 150 nm and the bimodal part a thickness of 340 nm.

The coupling efficiency of the fundamental and the first order mode of the bimodal part are estimated by overlap integrals from the equations of the electric field in the three regions of the waveguide. Using these integrals, the confinement factors for both the fundamental and first order modes in the bimodal part are evaluated as 0.94 and 0.67, respectively. The values indicate that the fundamental mode is less sensitive to the upper cladding layer parameters, as more energy is located inside the core of the waveguide than for the first order mode. As a result, the interaction of the first mode with the external medium when traveling along the sensor area is higher than for the fundamental that is more confined in the core.

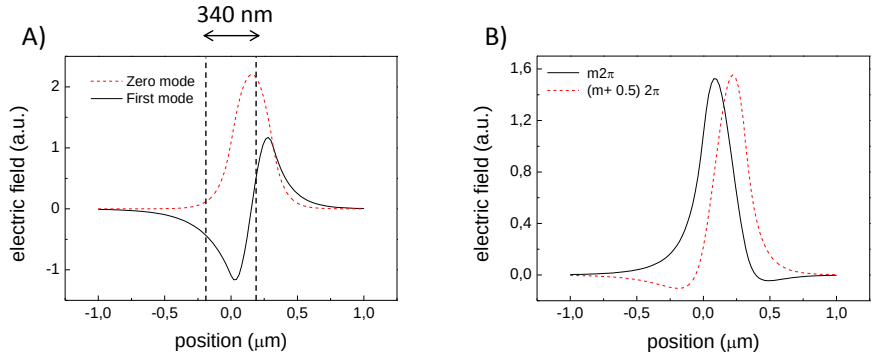

Figure 2.17: Representation of the modes in the waveguide by the transfer matrix approach. A) Electric field profiles for zero and first order modes in the bimodal section of the waveguide and B) output electric field profiles for different phase difference of π between the modes.

In summary, i) Si_3N_4/SiO_2 materials have been chosen due to the high index contrast that they offer ($\Delta n = 0.5$), ii) the depth values for the rib are of few nanometers and the values for the width are around 4 μm to obtain a single mode behavior in the y coordinate, and iii) the thickness of the core in the single-mode section mus be 150 nm to obtain a 70% of modulation at the output of the device. Figure 2.18 A shows the structure of the rib waveguide while Figure 2.18 B shows the final layer composition of the BiMW device.

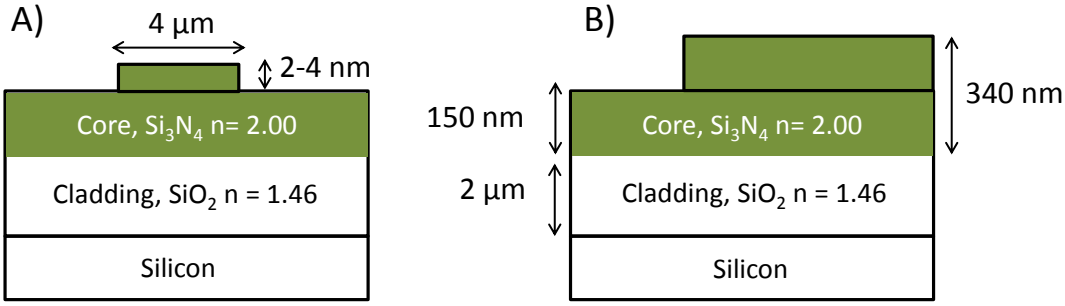

Figure 2.18: Selected layer waveguide structure of a BiMW transducer. A) The rib waveguide dimensions and B) the thickness of the layers.

Due to the abrupt height variation between the waveguides, the light losses in the modal splitter region must be studied. For that purpose, different computational electrodynamics modeling algorithms, the beam propagation method (BPM) and the finite-difference time-domain method (FDTD) were employed. Unlike semi-analytical methods, these numerical methods solve Maxwell's equations exactly and the results are often achieved at the expense of long computational times.

The BPM describes the evolution of the total field propagating along a guide. It represents the total field as a superposition of plane waves that propagate in a homogeneous medium. The field that propagates in an inhomogeneous media is calculated by integrating the fields in the spectral domain and applying the phase correction in spatial domain at each propagation step. The BPM algorithm for the propagation along an arbitrary distance z is realized through several discrete steps of distance Δz. The propagation of the wave for a distance Δz causes an index variation n(x, y, z) that can be described by incorporating a lens corrector operator. Discrete Fourier transform is used to numerically implement this method. The FDTD method is a type of grid-based differential time-domain method. It is based on the fact that a temporal change of the electric field is related to a spatial change in the magnetic field across space. The electric field vector components are solved at a given instant in time; the magnetic field vector components in the same spatial volume are solved at the next instant in time, and the process is repeated until the electromagnetic field is totally evolved.

The results for the simulation of the light behavior around the modal splitter are shown in Figure 2.19 with the conditions specified in Table 2.1 .

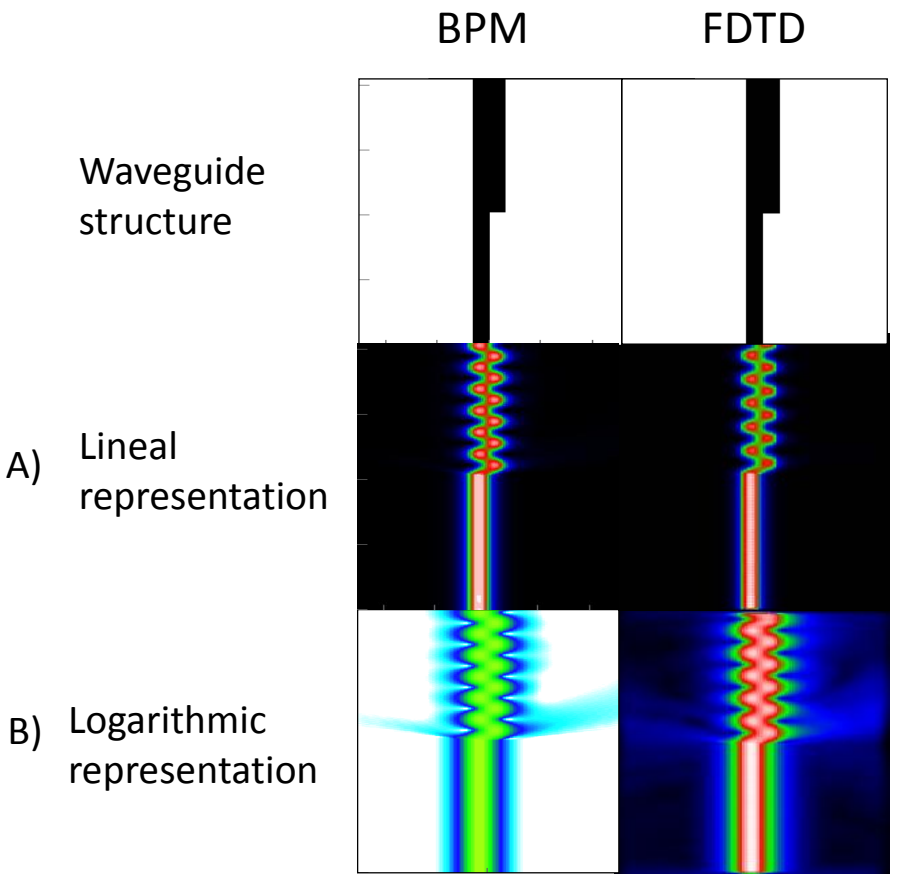

Figure 2.19: Simulation of the light losses in the modal splitter region of a BiMW by BMP and FDTD methods. Linear and logarithmic representations of electromagnetic field are shown.

Table 2.1: Conditions used to calculate the light losses in the modal splitter region.

Conditions	values
wavelength	633 nm
point size	20 nm×40 nm
window points	128×512
cover refractive index	1.33
substrate refractive index	1.46
substrate index increase	0.54
waveguide width	160 nm
attenuation	0.000001 nm^{-1}

In both methods, it can be observed that the first mode is generated in the bimodal waveguide section. As BMP is a paraxial method, only light dispersed in an angle smaller than 30 - 40° in the propagation direction is shown. On the contrary, FDTD shows dispersed light for higher angles as well as retro-dispersion. Logarithmic representation of electromagnetic fields (see Figure 2.19 B) shows that the quantity of dispersed light is very small, light is well-confined and that the retro-dispersed light is negligible.

Once the device has been designed, lithographic masks are required to transfer geometric patterns from the mask to the wafers. Four different masks are employed in the fabrication of the BiMW devices, the masks are used in different lithographic steps such as to open the sensor area and to define the single-mode section or the rib waveguide. The set of masks is shown in Figure 2.20 in which 12 different chips are allocated. Additionally, we have to include micro-metric marks to line up the different masks during the fabrication process as shown in the inset.

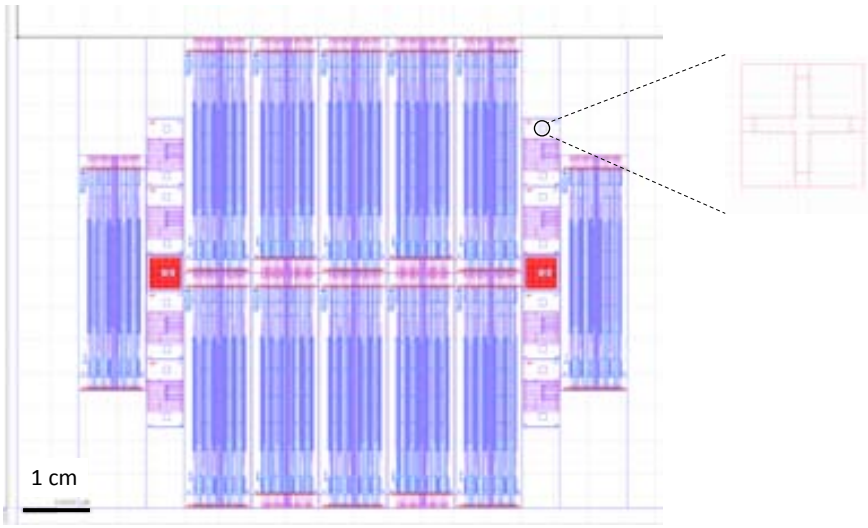

Figure 2.20: Set of masks for the fabrication of the BiMW devices. In the inset: micro-marks are included to align the different masks.

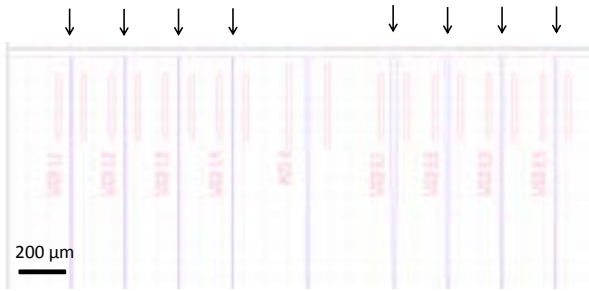

Figure 2.21: Alignment marks to aid in the coupling of light into the BiMW rib waveguides.

Due to the nanometric size of the rib, it can not be observed by eye neither by optical microscope. Therefore, it is necessary to include alignment marks to couple light into the rib waveguide. In Figure 2.21, we show the alignment

marks indicating the position of the different BiMW rib waveguides as pointed out with arrows.

The total length of the chip including both single and bimodal parts is 30 mm. The total length of the bimodal part is 25 mm, which included the sensing window with a length of 15 mm, placed 5 mm off the chip exit. The sensing window has an area of 15 × 0.05 mm^2. The chip is 30 × 10 mm^2 in size and contained 16 independent interferometers divided in groups of four as illustrated in Figure 2.22. In each group of four, the BiMW interferometers are separated 250 μm to assure a null light coupling between the devices.

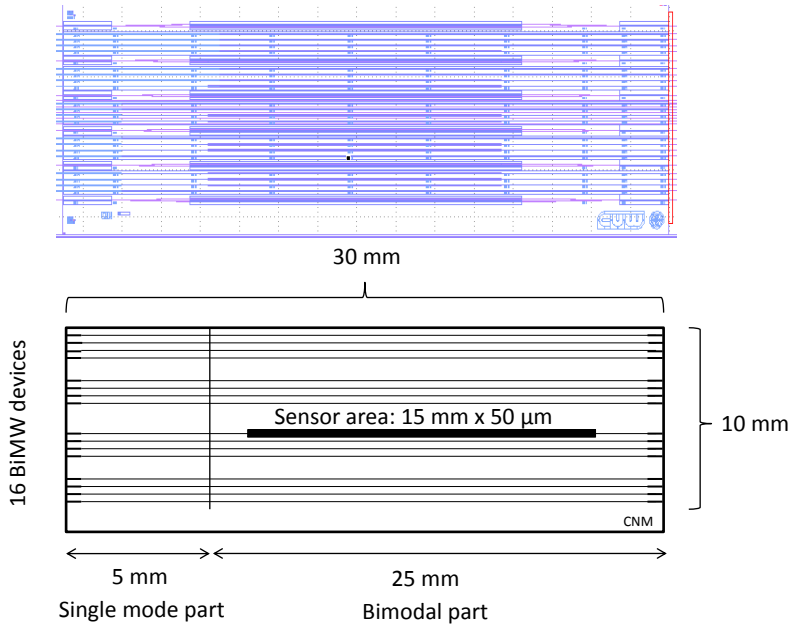

Figure 2.22: BiMW chip layout.

2.4 Fabrication of the devices

The BiMW devices are fabricated at the Clean Room facilities of the Centro Nacional de Microelectronica (CNM) in Barcelona. The materials employed are low pressure chemical vapor deposition (LPCVD) silicon nitride (Si_3N_4, $n_{Si_3N_4}$

= 2.00) and, thermally grown silicon oxide by plasma enhanced chemical vapour deposition (PECVD) (SiO_2, $n_{SiO_2} = 1.46$) that are transparent to the working wavelength (632.8 nm). Microfabrication based on silicon allows for the growth of amorphous oxide layers, with a good adhesion to the substrate and good mechanical and chemical stability. Moreover, the refractive index of the grown layers is uniform and reproducible and the roughness is low. A scheme of the different steps in the fabrication of a BiMW device is shown in Figure 2.23. The fabrication process starts from a 4-inch (p-type) silicon wafer with a thickness of 500 μm. A 2 μm layer of SiO_2 (n = 1.46) is thermally growth covering the silicon wafer (Figure 2.23 A).

This layer is required to confine the light in the core and to isolate it of the silicon substrate that adsorbs visible light. In the next step, a 340 nm core layer (Si_3N_4, n = 2) layer is deposited by LPCVD (Figure 2.23 B). After that, the thickness of the core layer is reduced in the single-mode region of the device from 340 nm to 150 nm by a photolithography process using a borophosphosilicate glass (BPSG) as protecting layer (Figure 2.23 C). Thus, the waveguides are defined by reactive-ion etching (RIE) of the rib using a photolithography process (Figure 2.23 D). An adsorbent layer of 100 nm is deposited by LPCVD on a SiO_2 layer of 200 nm previously deposited to improve the adhesion (Figure 2.23 D). In a third photolithography process, the adsorbent layer is opening (Figure 2.23 E), and afterwards, a 2 μm SiO_2 cladding layer is deposited by PECVD (Figure 2.23 E). Finally, the sensor area is opening by etching the SiO_2 cladding layer. After the fabrication is covered with a protected resist layer and the individual chips are cut at the Clean Room by using a dicing machine. As 12 chips are produced and every chip has 16 devices, a total number of 192 BiMW devices are available per wafer.

A picture of the final chip is shown in Figure 2.24 A. In Figure B, we show an image of a chip in comparison with a coin to notice its size. Figure C shows an optical microscope image with a magnification of 4× of the alignment marks employed to couple the light in the devices. Figure D shows a 4× magnification optical microscope image of the sensor areas of a group of four devices.

The fabrication of the rib is one of the most critical steps in the fabrication process due that the rib size is very close to the maximum resolution allowed by this technique. Hence, a slight variation in the size of the rib can lead to a high dispersion of results in terms of transducer sensitivity. The morphology of the rib is obtained by atomic force microscopy (AFM), shown in Figure 2.25.

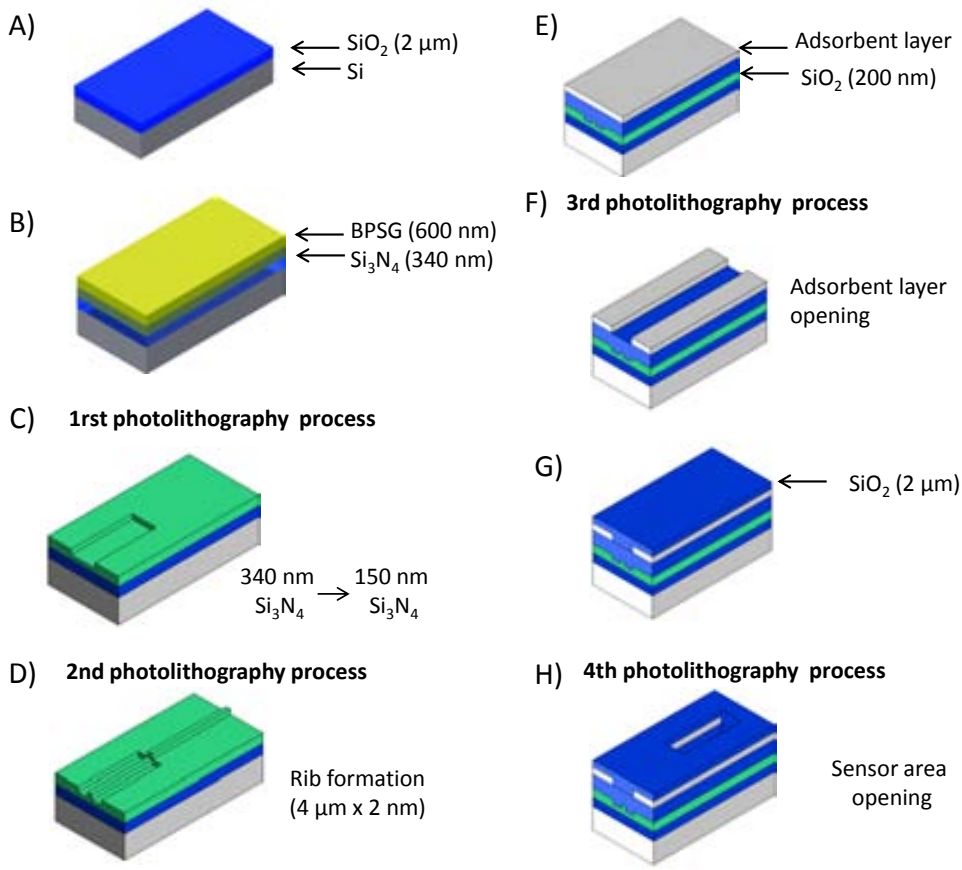

Figure 2.23: Sketch of the different steps in the fabrication process of the BiMW. A) A 2 μm SiO_2 cladding layer is thermally growth over a silicon wafer, B) 340 nm of Si_3N_4 is deposited by LPCVD, C) the thickness of the core is reduced to 150 nm for the single mode part of the waveguide, D) a rib 4 μm width and 1 nm height is generated, E) 200 nm layer of SiO_2 and 1 μm adsorbent layer are deposited and F) the adsorbent layer is opened, G) a 2 μm SiO_2 cladding layer is deposited and H) the sensor area is opened.

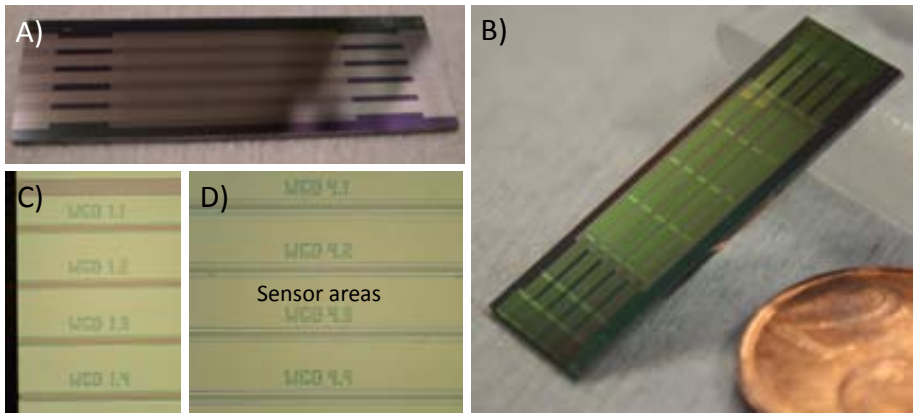

Figure 2.24: Picture of a final BiMW sensing chip.

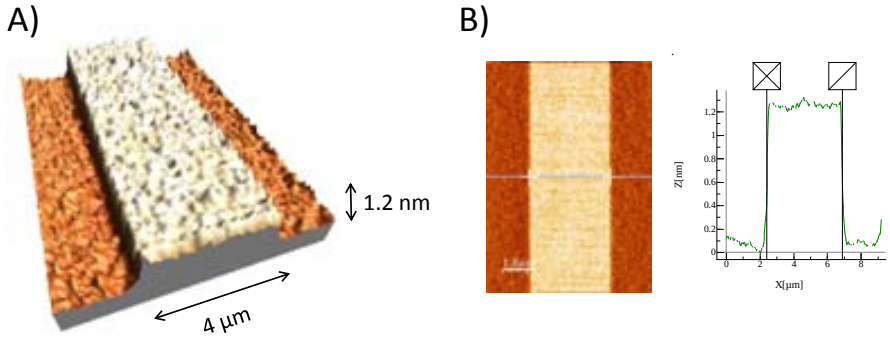

Figure 2.25: 10 μm $\times$ 10 μm AFM pictures of the nanometric waveguide rib of the BiMW. A) 3D AFM image of the rib waveguide and B) the profile of the waveguide rib.

AFM images are recorded on an Agilent 5500 AFM/SPM microscope (formerly molecular Imaging PicoPlus AFM) in tapping mode. A multi-purpose low-coherence scanner with scan range up to 90 μm is used for imaging samples under ambient conditions. The AFM probes are NSC15 silicon pointprobes (force constant 30-50 N/ m, resonant frequency 330 KHz) from MikroMasch.

AFM image processing and rendering is done with the WSxM software (Nanotec). For a reproducibility study of the microfabrication process, 16 independent rib waveguides of a chip were examined by AFM. The results confirm the reproducibility of the process, obtaining a rib width of **4.45 ± 0.02 μm** and a height of **1.22 ± 0.03 nm**. These results assure a high reproducibility in the sensitivity of the fabricated devices in the same chip.

2.5 Optical characterization

Before the optical characterization, the polishing of the edges is required to obtain specular surfaces to couple light using an objective. The method to polish the edges of the chips consists of a revolving plate in which polishing papers are sticked and the chip is leaned on its surface. The polishing machine (Logitech CL50, Figure 2.26) is designed to polish flat surfaces. However, the use of a micrometer positioner assembled to the machine allows us to place the chip in a vertical position.

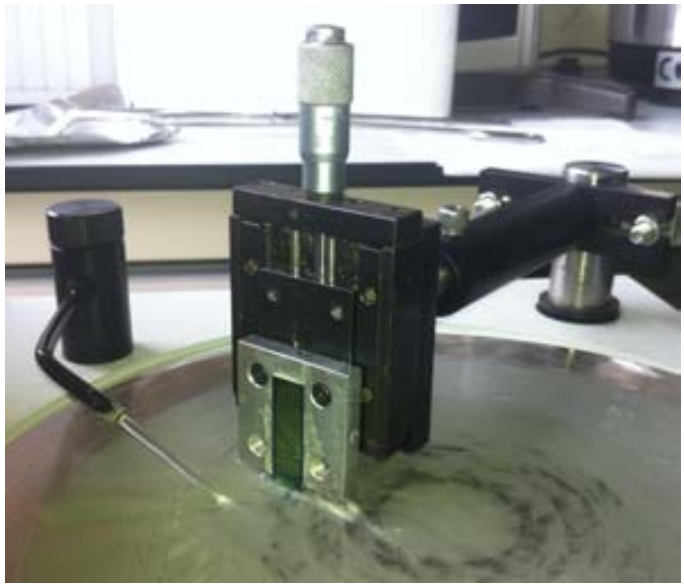

Figure 2.26: Image of the polishing machine.

Firstly, a 9 μm grain size abrasive paper is used to polish the edges of the chip for 5 min at an angular velocity of 30 rpm. A stream of water refrigerates the contact surface between the paper and the chip, eliminates particles, and lubricates the abrasive paper surface. After that, the 9 μm abrasive paper is changed by another with 3 μm grain size which is used for 15 min. Finally, the optical quality is obtained by polishing the edge using a 0.3 μm grain size paper. After every step of the polishing process, it is necessary to check the edges using an optical microscope (Figure 2.27), to assure that the surface is free of defects and thus, we will have low insertion loses.

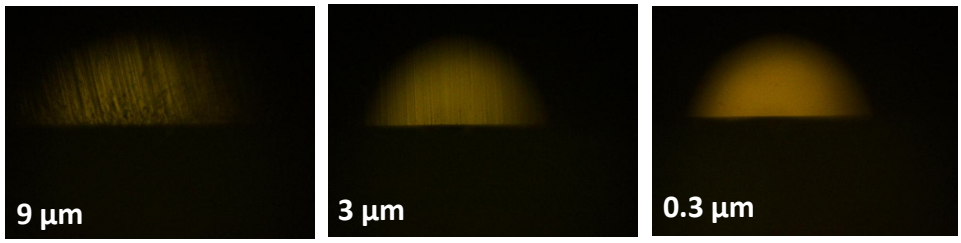

Figure 2.27: Optical microscope image (4×) of a chip edge after every step of the polishing process.

2.5.1 Experimental set up

For evaluation of the BiMW device, a He-Ne laser in TE configuration is employed as light source as it offers a narrow spectral line, stable in time, and with a coherency length of several millimeters. Moreover, the frequency of the light from the He-Ne laser (λ= 632.8 nm) located at the red part of the visible spectrum does not interact with the biomolecules. The light from the He-Ne laser is coupled into the rib waveguide by using a microscope objective (40×) and a beam expander as shown in Figure 2.28.

Figure 2.28: Light source employed for coupling light into the rib waveguide.

The chip is installed on a home-made copper base mounted over a thermoelectric element connected to a temperature controller (see Figure 2.29). This assembly requires a temperature transducer incorporated to the copper base. This system provides temperature stabilization of the chip with 0.01 degrees accuracy.

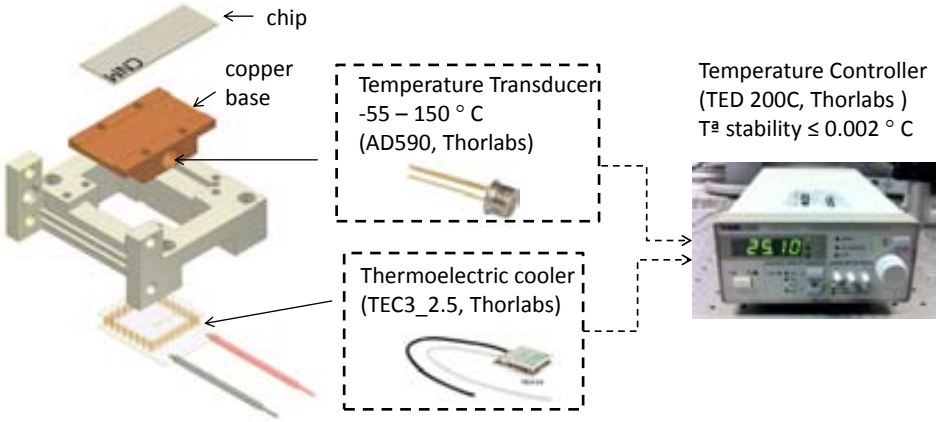

Figure 2.29: Schematic drawing of the temperature stabilization system.

For sensing evaluation, a flow cell is designed and fabricated by soft-lithography using a durable and inexpensive material, polydimethylsiloxane (PDMS, Sylgard) silicon elastomer (see Figure 2.30). Firstly, a methacrylate (PMMA)

topographic master is fabricated using a standard milling machine. Then, the elastomer is mixing with a curing agent in a 10:1 ratio in weight and the PMMA master is carefully filled with the solution. The PMMA master with the PDMS elastomer is placed inside a vacuum chamber for 1 h to evacuate the bubbles trapped in the elastomer. After that, the PMMA master filled with the elastomer is cured into an oven at 80° C. The final fluidic housing with embedded PDMS mold has four independent channels (15 μl volume each) which cover each of the sensing areas of a group of four interferometers. The microfluidic header is coupled to a syringe pump and an injection valve and allows the sequential evaluation of up to 4 sensors per chip. The normal operation of the fluidic system consists in maintaining a fixed fluid in the flow system, and introducing 250 μl of a determined solution sample when required using the injection valve. The velocity of the pump is modified according with the detection requirements, in a range from 5 to 40 μl/min. The flow cell is easily attached and detached to the chip surface and a hermetic sealing is ensured by screwing the cell to the chip support.

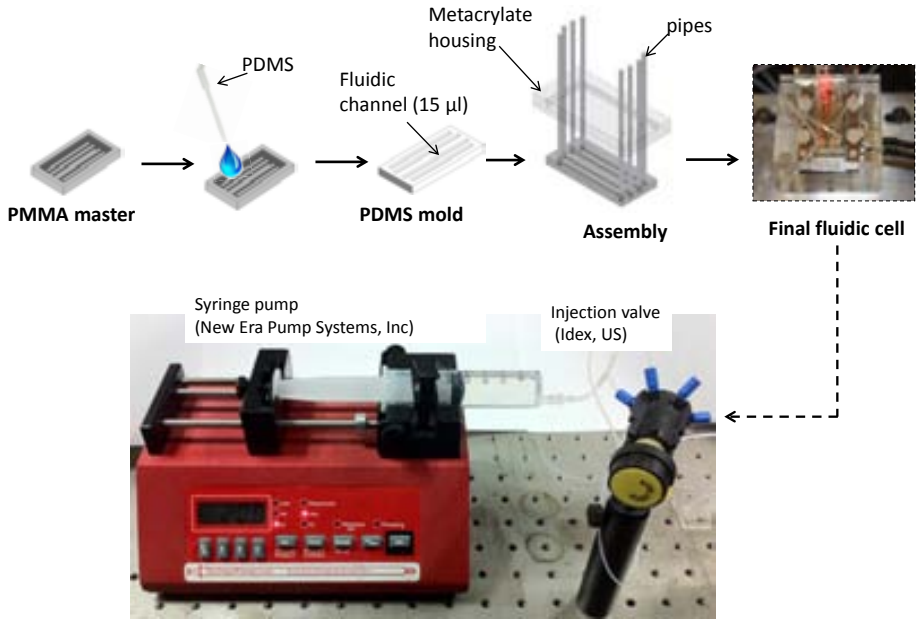

Figure 2.30: Sketch of the fluidic system.

The interference pattern at the output of the bimodal waveguide is monitored using a two sectional photodiode and each section is connected to a current amplifier as sketched in Figure 2.31. Light exiting the waveguide generates currents I_{up} and I_{down} in the upper and the lower sections of the photodetector, respectively. The values of the currents are used to calculate the parameter S (sensitivity), proportional to the phase variation of the signal, according with the expression:

$$S = \frac{I_{up} - I_{down}}{I_{up} + I_{down}} \quad \cos(\Delta\Phi_S(t)) \tag{2.47}$$

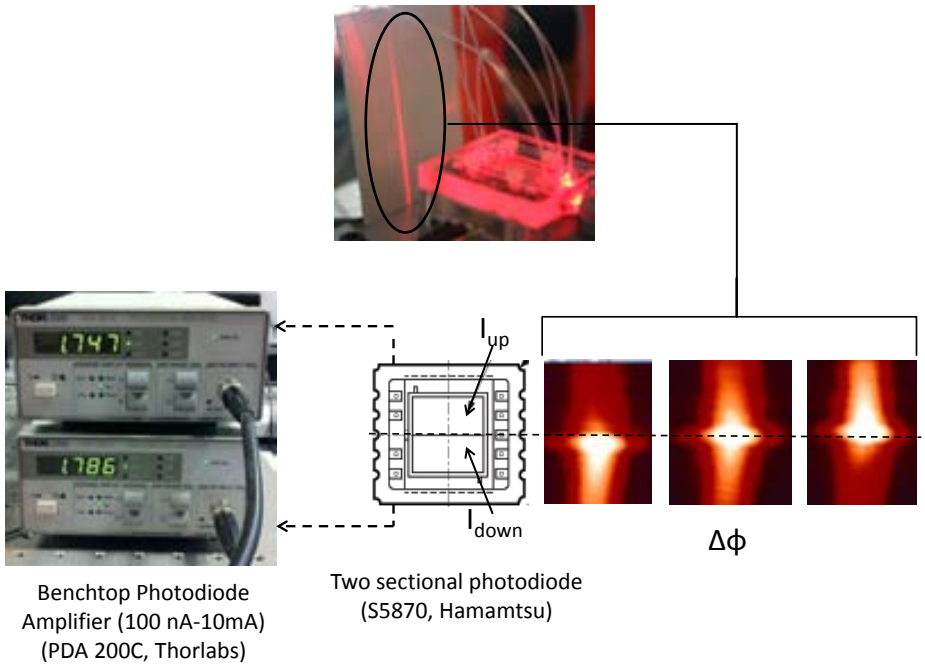

Figure 2.31: Processing of the output signal of a BiMW waveguide.

Due to the signal S is normalized with the intensity addition ($I_{up} + I_{down}$), it can be deduced that the interference pattern is independent on the light intensity and the output signal is not sensitive to fluctuations in the coupling efficiency. This fact gives an additional stabilization to the signal that will not

affected by the thermal expansion of the chip folder. Furthermore, the signal will not vary by variations in the input light.

The photodetector is directly attached to the chip output facet to obtain the minimum dispersion of the signal as shown in Figure 2.32. To obtain a low noise, all the light detected by the photodetector must come from the device output. Therefore, the environmental light is prevented to come intro the photodetector by blocking the side of the fluidic cell with an opaque material.

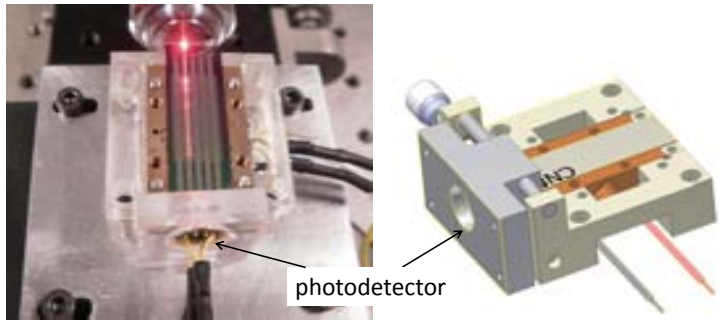

Figure 2.32: Chip mounted onto the temperature stabilization unit with the photodetector attached at the output facet. Note that a coupled rib waveguide is shown at the picture.

The two signals coming from the current amplifiers are acquired through an acquisition card and manipulated with a dedicated Labview software (National Instruments). The value S (see equation 2.47) is evaluated and displayed in real-time. A screenshot of the user interface of this software is shown in Figure 2.33.

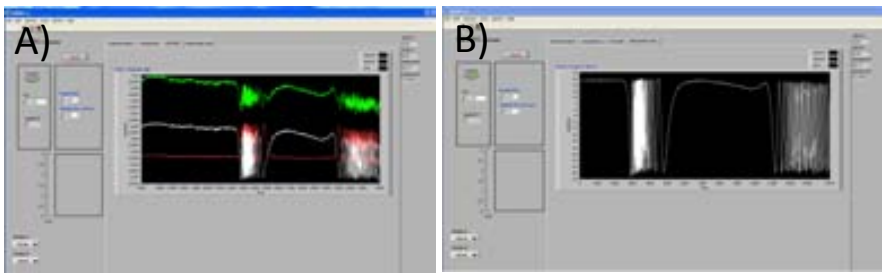

Figure 2.33: Screenshot of the software for the characterization of a BiMW device. A) Individual intensities for each photodetection section (I_{up}, white and I_{down} red lines) and the operation $I_{up} + I_{down}$ (green line), and B) resulting signal after applying the operation described in equation 2.47.

The resulting set up employed for all the sensing and biosensing experiments is shown in Figure 2.34.

As the BiMW is an interferometric device, the signal obtained has a periodic nature that can give rise to wrong or ambiguous interpretations. This is due to the cosine dependency that can be deduced from equation 2.47. This dependency leads to ambiguity in the interpretation of the signal and to a variable sensitivity. There are three main issues related to this type of signal: ambiguity, sensitivity fading, and intensity fluctuations leading to false positives. Signal ambiguity prevents the discrimination between two values differing of an integer multiple of 2π and impedes the prediction of the phase evolution direction when the phase difference between the two arms is an integer multiple of π. At the same time, sensitivity suffers the same periodicity of phase evolution, i.e. is not constant but maximum at quadrature point and minimum at curve extremes.

2.5.2 Temperature e ect

The different interaction of the two modes with the external medium makes the BiMW device sensitive to temperature changes. Therefore, a change in the temperature of the system can be employed to estimate the quality of the modal splitter and the noise of the system. The chip is placed at the optical set up and water is flowed at a constant rate of 20 μl/min by using the flow system. Light is coupled and the output signal is recorded in real-time. After monitored the baseline for 35 minutes, the temperature is increased 2.2 degrees, from 22.2 to 24.6°C. The interferometric signal obtained for this variation of the temperature is shown in Figure 2.35. It can be seen a modulation deep of

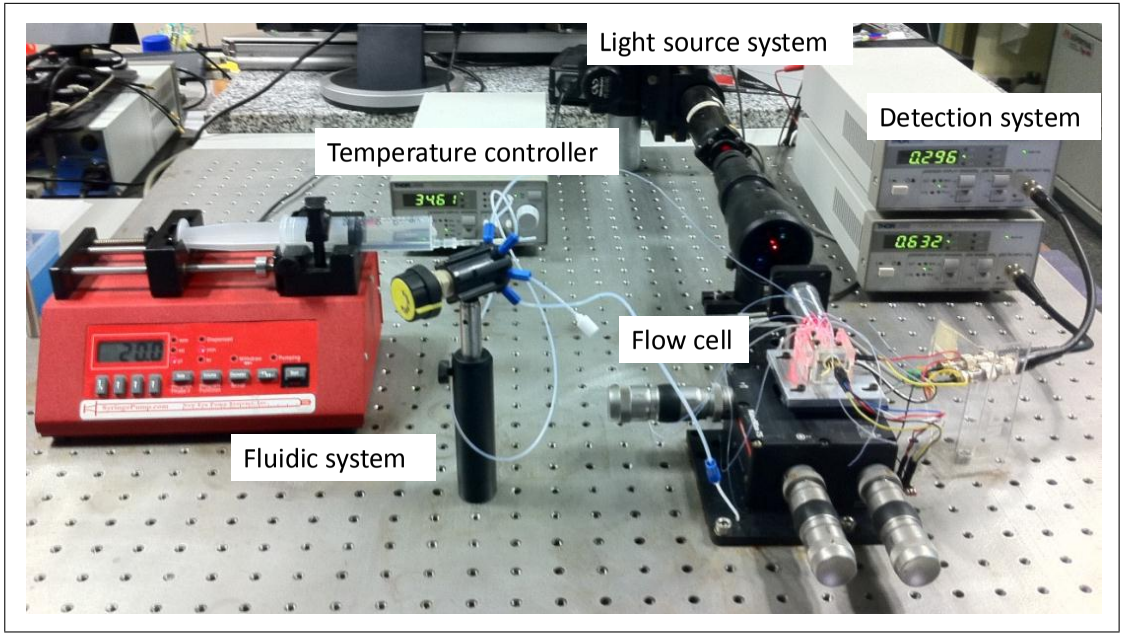

Figure 2.34: Set up of the BiMW device.

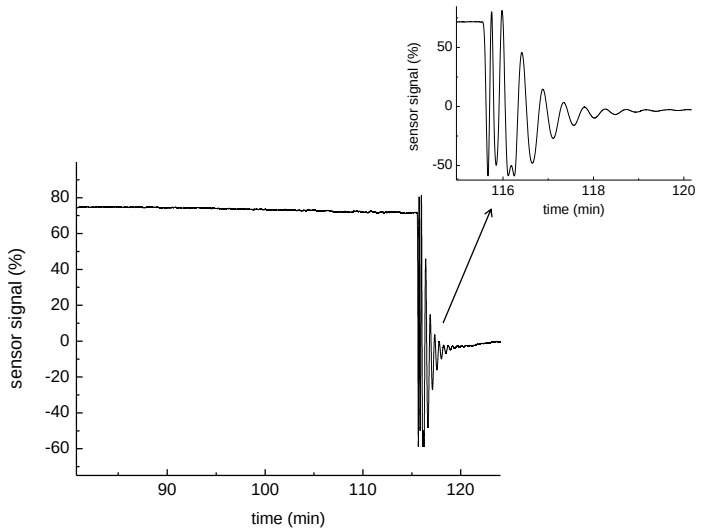

Figure 2.35: Response of the BiMW device to a 2.2 degrees of temperature change.

Taking into account the modulation depth of the output signal, the fluctuation in the parameter S did not exceed the 2% for 35 min previous to the temperature change. This result evidences the high stability of the system provided by the temperature controller with an accuracy of 0.01 °C.

2.5.3 Homogeneous sensing

To check the sensitivity of our device, a calibration curve evaluating bulk refractive index changes is carried out (see Figure 2.36). Using the system described above, injections of different concentrations of HCl (0.2 M, 0.1 M, 0.05 M and 0.025 M) are flowed. Previously to injection, the refractive index of the solutions is checked with an ABBE Refractometer (Optic Ivymen System, Spain). Refractive indexes of the HCl solutions and the Δn that are evaluated by n_{HCl}-n_{H_2O} are summarized in Table 2.2.

In the experiments, a continuous water flow at a constant rate of 20 μl/min is maintained over the sensor surface which is gradually replaced by an injected loop of 250 μl of the HCl solution under evaluation.

HCl concentration (M)	n	Δn	$\Delta\Phi\times 2\pi$rad
0.2	1.3342	1.9E-3	3.47
0.1	1.3333	1E-3	1.65
0.05	1.3331	6E-4	0.83
0.025	1.3329	4E-4	0.45

Table 2.2: Values of the absolute refractive index (n) of HCl concentrations and change in refractive index (n).

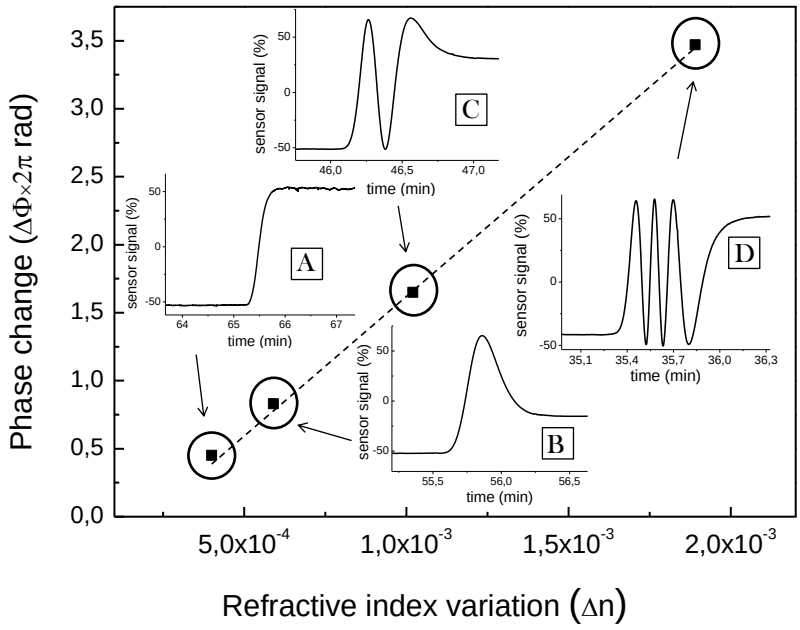

Figure 2.36: Sensitivity evaluation of the BiMW sensor: phase change is evaluated as a function of the refractive index variation due to the injected HCl concentrations. Inset: A) n = 4×10^{-4}, B) n = 6×10^{-4}, C) n = 1×10^{-3}, D) n = 1.9×10^{-3} (in all the insets only HCl entrance is showed).

Changes of the refractive index over the sensor area induce a phase change through the evanescent field interaction. Phase variation is plotted versus index variation (Δn) and the experimental sensitivity is determined as $\frac{2}{dn} = 2026$.

As the lowest phase shift which could be evaluated is considered to be three times the N/S ratio which is $5\times10^{-4}\times2\pi$ rad, this means that a theoretical detection limit of Δn_{min}= **2.5×10^{-7} RIU** could be achieved. This LOD for a bulk change in the refractive index is extraordinary low and is very close from the most sensible optical devices described in the literature (see Table 1.1).

2.5.4 Surface sensing

The surface sensitivity of the device can be demonstrated by a simple protein adsorption on the sensor area surface. We use Bovine Serum Albumin (BSA) protein that is commonly employed to prove the applicability of novel waveguide biosensors [11]. For the experiment, components of phosphate Buffer Saline (PBS; 10mM phosphate, 2.9 mMKCl, 137 mM NaCl, pH 7.4), and albumin bovine 95 99% (BSA) were purchased from Sigma. The employed water was Milli-Q grade (Millipore).

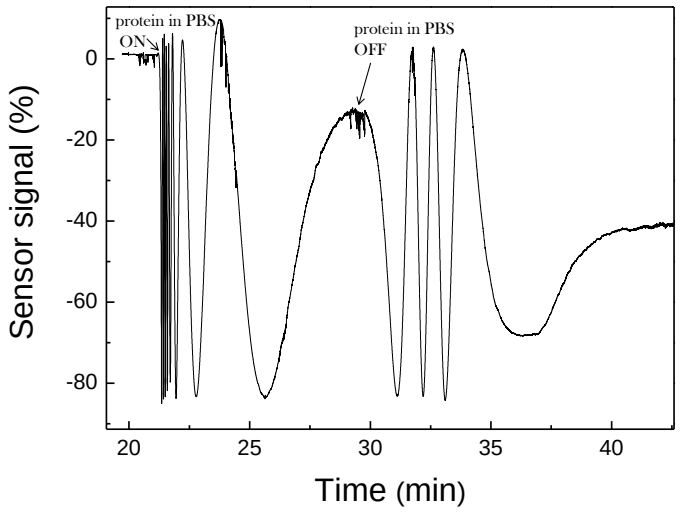

Figure 2.37: Real-time monitoring of the phase change due to the injection of 250 μl of 50 μg/ml BSA in PBS.

Physical adsorption of BSA protein onto the sensor area of the BiMW was

done by flowing 250 μl of a PBS solution with 50 μg/ml BSA, at a flow rate of 10 μl/min. Phase variation (7.86 $\times 2\pi$ rad) due to the refractive index bulk change and physical adsorption of the protein is observed in Figure 2.37. The phase change becomes slower until reaches a stable signal, which means that the surface is totally saturated with proteins. Next, a phase change of (3.30 $\times 2\pi$ rad) is observed, due to the refractive index change from PBS to water. Finally, the water flow induces the detachment of non-adsorbed protein (0.15 $\times 2\pi$ rad). Therefore, the total phase change due to receptor attachment was (4.41 $\times 2\pi$ rad), corresponding to an experimental covering of 0.42 ng/mm^2 [12] of BSA receptors (pH=7).

Taking into account the experimental covering of BSA at this pH, considering the sensor area surface (0.6 mm^2), the standard value of density of a protein (0.183 cm^3/g), and the minimum detectable phase change ($5\times10^{-4}\times 2\pi$ rad) the calculated surface sensitivity corresponds to 3×10^{-5} nm^{-1}.

2.6 Conclusion

A two-mode interference device, the BiMW interferometer, has been presented in this chapter. The thickness of the waveguide core has been optimized to obtain more than 70% of the output signal modulation and confinement factors of the modes have been calculated, obtaining a higher delocalization for first order mode. Losses of light in crossing the modal splitter have been analyzed by simulations and it has been found that the quantity of light dispersed is not significant. Silicon-based technology is chosen to fabricate the BiMW device by a standard microfabrication procedure. Si_3N_4 (n = 2.00) and SiO_2 (n = 1.46) have been chosen as core and cladding layer, respectively. Final chip consists of 16 independent rib waveguides, 192 devices per wafer. Sub-micron precision in the fabrication process has been verified with morphologic characterization of the rib waveguide dimensions by AFM, demonstrating a high reproducibility of the fabricated devices. The set up used for the optical characterization has been presented. The chip is stabilized in temperature with an accuracy of 0.01 by placing it on a copper base in contact with a thermoelectric element connected to a temperature controller. It has been demonstrated that an increase of one degree over the chip does not affect the modulation depth, although the $I_{up} + I_{down}$ signal decreased due to the thermal expansion of the chip. A 4-channel microfluidic cell fabricated with PDMS allows the flow transport until the transducer surface and the liquid movement is controlled by mechanical displacement of liquid by a pump.

The sensitivity of the device to changes in the buld refractive index has been investigated by maintaining water in flow and supplying solutions with different refractive indexes. A theoretical detection limit of $\Delta n_{min} = 2.5\times10^{-7}$ RIU has been achieved for bulk refractive index changes, whereas a surface sensitivity of 3×10^{-5} nm^{-1} has been experimentally found for BSA adsorption.

Bibliography

[1] E. Hecht. *Optics*. Addison Wesley, 2002.

[2] Gines Lifante. *Integrated photonics fundamentals*. Wiley, 2003.

[3] H. Kogelnik. 2. theory of dielectric waveguides. In *Integrated Optics*, volume 7 of *Topics in Applied Physics*, pages 13 81. Springer Berlin / Heidelberg, 1975. 10.1007/BFb0103618.

[4] Francisco Pietro. *Sensores Interferometricos Mach-Zehnder integrados basados en guias de onda arrow para aplicationes biosensoras*. PhD thesis, Centro Nacional de Microelectronica, CSIC, 2002.

[5] T. Tamir. *Guided-wave Optoelectronics*. Berlin: Springer, 1988.

[6] Jose Sanchez. *Desarrollo de un biosensor fotonico de alta sensibilidad basado en interferometros Mach-Zehnder integrados en tecnolog a de silicio*. PhD thesis, Centro Nacional de Microelectronica, CSIC, 2007.

[7] F Prieto, B Sepulveda, A Calle, A Llobera, C Dom nguez, A Abad, A Montoya, and L M Lechuga. An integrated optical interferometric nanodevice based on silicon technology for biosensor applications. *Nanotechnology*, 14:907 912, 2003.

[8] M. Vogt and R. Hauptmann. Plasma-deposited passivation layers for moisture and water protection. 74 75:676 681, 1995.

[9] Kirill E. Zinoviev, Ana Belen Gonzalez-Guerrero, Carlos Dom nguez, and Laura M. Lechuga. Integrated bimodal waveguide interferometric biosensor for label-free analysis. *J. Lightwave Tech.*, 29:1926 1930, 2011.

[10] Carlos Dominguez Horna, Kirill Zinoviev, and Laura M. Lechuga Gomez. Patent. interferometer and sensor based on bimodal optical waveguides, and detection method, Oct 2010.

[11] D. Dorfner, T. Zabel, T. Hurlimann, N. Hauke, L. Frandsen, U. Rant, G. Abstreiter, and J. Finley. Photonic crystal nanostructures for optical biosensing applications. *Biosensors and Bioelectronics*, 24(2):3688 3692, 2009.

[12] N. J. Freeman, L. L. Peel, M. J. Swann, G. H. Cross, A. Reeves, S. Brand, and J. R. Lu. Real time, high resolution studies of protein adsorption and structure at solid-liquid interface using dual polarization interferometry. *J. Phys.; Condens. Matter*, 16:S2493 S2496, 2009.

Chapter 3

Biofunctionalization of the Si_3N_4 sensor area

"`An experiment is a question which science poses to Nature, and a measurements is the recording of Nature's answer"'

Max Planck, Scientific Autobiography and other papers

3.1 Introduction

The sensor area of the BiMW device is the region of the core of the biosensor in contact with the changing external medium. Processes occurring on this surface such as changes in the bulk refractive index or protein adsorption originate a net change in the phase variation of the output signal at the end of the waveguide. The device is not selective at this point, since different types of biomolecules could be adsorbed on its sensor area giving unspecific signals. The device is just sensitive to refractive index changes until a selective bioreceptor layer is assembled onto the transducer surface. Only then the BiMW device turns into a biosensor.

Immobilization of the biomolecules on the Si_3N_4 core waveguide surface is an important step in the biosensor development. In some cases, the immobilization of biomolecules on Si_3N_4 waveguide surfaces has been carried out by physical adsorption [1]. However, covalent attachment of the biomolecules has been employed when a stable and resistant biosensing surface is required [2 4]

as explained previously. Therefore, the study of a chemical modification of the Si_3N_4 inert surface to create functional reactive groups is required to implement the bioreceptor layer.

The biorecognition layer will provide the biosensor with the ability for discriminating between interference and the analyte to detect. At the same time, it establishes the maximum number of available binding sites to interact with the analyte, an essential issue to obtain the minimum LOD for a particular application. Moreover, the stability of the receptor layer must be considered when an exhaustive study of the recognition event is needed due to the possibility of regenerating the surface, extremely useful to diminish cost and time.

Silanization methods have been extensively employed to covalently attach biomolecules to silicon-based surfaces. They are the simplest way to generate reactive functional groups onto silicon surfaces due to its simplicity and the few number of steps required. Furthermore, silanization methods have been already extensively investigated and the mechanism used by the silane molecule to link the surface is well-known. The core of a silane coupling agent is a silicon atom (Si) bonded with an inorganic functional group (amino, mercapto, chloro, epoxy...) and three ether groups (methoxy, ethoxy...). Ether groups bond to a silanol group on the Si_3N_4 surface whereas inorganic functional groups provide the surface with anchorage points for the attachment of biomolecules. An undesirable effect regarding the use of trialkoxysilanes is the polymerization that can occur at the free silanol groups on the surface or in solution, leading to highly heterogeneous surfaces, a potential disadvantage when dealing with biosensors. To avoid this negative effect, anhydrous solvents have been used to limit the amount of water reacting during the monolayer formation [5]. However, small variations in the amount of water during the silanization reaction can dramatically alter the thickness of the final film giving place to highly irreproducible surfaces due to the formation of silane multilayers [6].

The most employed silane to functionalize Si_3N_4 surfaces is the 3-Aminopropyltriethoxy silane (APTES). This silane provides silicon surfaces with amino groups [3, 4] that can be further activated with glutaraldehyde to introduce a layer of aldehyde groups. Proteins can be immobilized on these surfaces through Schiff's base condensation between free amine groups on proteins and aldehyde groups on the modified surfaces [4]. This strategy has some undesirable effects, such as the formation of several layers of glutaraldehyde that could break during the biorecognition process giving inaccurate signals.

In this chapter, we establish the reaction parameters (time and concentration) of the silanization protocols employed to covalently immobilize the bioreceptors on the BiMW sensor areas.

3.2 Surface modi cation using a carboxyl-terminated silane (CTES)

Carboxyl group is the most suitable functional group for bioconjugation of proteins because of its chemical versatility and wetting properties. However, the use of carboxyl-terminated silanes to functionalize a silicon surface is not frequently found in the literature. The ability of carboxyl groups to covalently link with biomolecules has led to the development of some approaches to provide Si_3N_4 surfaces with terminal carboxylic acid (sketched in Figure 3.1 A) by the use of a trifluoro ethanol ester and subsequent thermal acid hydrolysis [7], B) through attachment of a photocleavable ester and subsequent photochemical cleavage [7], or C) via the attachment of long-chain carboxylic acid terminated monolayers [8, 9]. However, these strategies involve a high number of preparation steps and require from strong acids (HF), organic solvents, and additional instrumentation.

To achieve a carboxylic acid terminated layer on the Si_3N_4 surface by a simple silanization method, avoiding the derived problems of using anhydrous solvents, and to take advantage of the suitability of carboxyl group for the bioconjugation we chose to study the use of a carboxyethylsilanetriol sodium salt (CTES). CTES has been extensively employed for the functionalization of silica particles [10, 11] and as a co-structure directing agent [12] normally by stirring for hours at high temperature. However, few works can be found about functionalization of silicon surfaces with CTES silane [13]. Due to its short alkyl chain of approximately 6 Å and to the hydrophilicity of the functional carboxyl group that contains, CTES is an organosilane stable front the cross-linking in water. This is an unusual property for a silane molecule that makes the use of CTES especially attractive to avoid concerns regarding the use of organic solvents and the generation of organic waste by the rinsing steps. Another attractive aspect of the use of water as solvent for the reaction is its larger dielectric constant, which favors the formation of packaged monolayers [14]. Moreover, the solvent compatibility with the polymer materials employed in our fluidic systems allows the use of CTES to silanize the sensor area inside the fluidic cell (in-flow) when

necessary for specific applications.

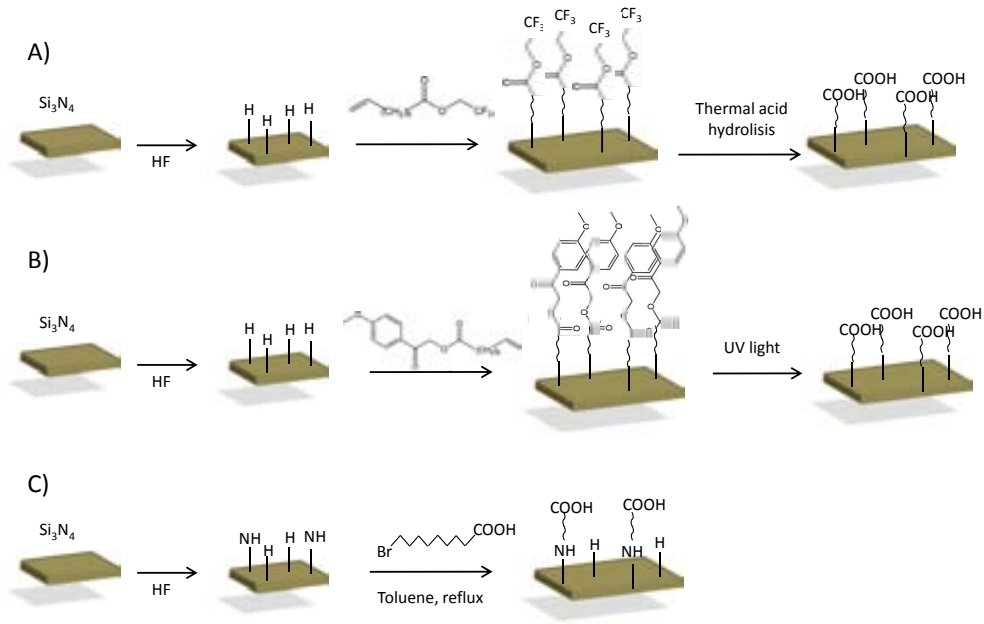

Figure 3.1: Sketch of the different strategies developed to provide the Si_3N_4 surface with carboxyl groups, through A) trifluoro ethanol ester, B) a photocleavable ester, and C) long-chain carboxyl-terminated monolayers.

The activation of carboxyl group with 1-ethyl-3-[3-dimethylaminopropyl]carbodiimide hydrochloride (EDC) and N-hydroxysulfosuccinimide (NHS) is the simplest way to obtain a peptidic bond between a surface and an amino group of a biomolecule (see Figure 3.2 A). The EDC/NHS mechanism is well-known [15] and its uses for covalent attachment of biomolecules has been extensively reported for gold surfaces [7, 16, 17]. After covalent coupling, the remaining reactive groups should be blocked to avoid covalent binding of the analyte to the surface as it is shown in Figure 3.2 B. This is an important issue related to the bioreceptor layer, specially crucial for the evaluation of real samples. The blocking agents have groups which are excellent in preventing nonspecific adsorption such as hydroxyl or poly(ethylene oxide) groups [18].

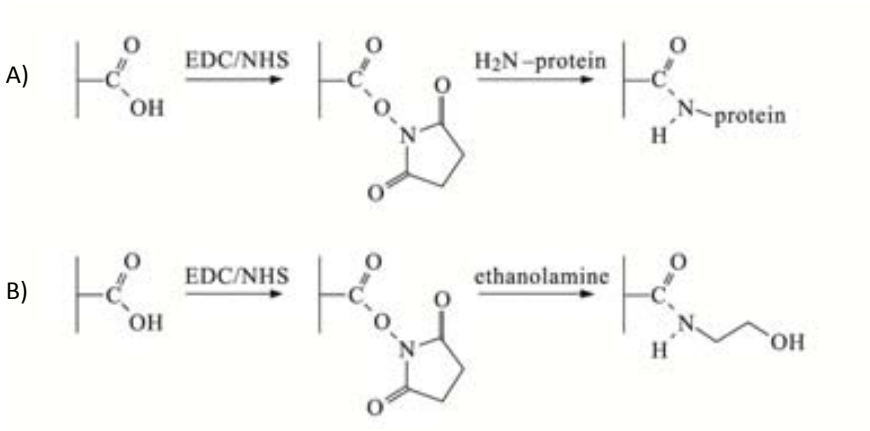

Figure 3.2: A) Covalent coupling of the amino groups of proteins to a carboxylic-terminated surface and B) the blocking of unreacted N-hydroxysuccinimide esters via ethanolamine.

Another important issue related with the formation of a bioreceptor layer is the method employed to place the biomolecules on the sensor surface. The most explored methods for the immobilization of the bioreceptor layer in biosensors are the in-flow strategy [19] and the patterning of surfaces [20]. The in-flow strategy uses smalls channels with low Reynolds number that generates a laminar flow [21], and allows the real-time monitoring of the layer formation. On the other hand, the surface patterning is based on the selective deposition of small volumes of samples under static conditions, which avoids the formation of the typical geometrical patterns due to the laminar flow [19].

To obtain an optimized functionalization protocol using the CTES silane, we have used standard surface techniques employed for the characterization of the surfaces such as the atomic force microscopy [8, 22], the contact angle analysis [9], and fluorescence microscopy. This optimized covalent strategy is used for the linkage of the bioreceptor on the sensor area surface using two different approaches: an in-flow patterning and a microcontact printing using a biodeposition system.

3.2.1 Materials and methods

Reactives. CTES was purchased from ABCR, Germany. Absolute ethanol (EtOH, 99%), acetone (Ac, 99,5%), and methanol (MeOH, 99,5%) were purchased from Panreac, Spain. Hydrochloric acid (HCl, 35-38%) was purchased from Poch SA, Poland. Sodium dodecyl sulfate (SDS) (99%), bovine serum albumin (BSA), monoclonal anti-bovine serum albumin antibody (anti-BSA), fluorescein isothiocyanate conjugate bovine albumin (FTIC-BSA), NHS (98%), all the components of phosphate buffered saline (PBS; 10 mM phosphate, 2.9 mM KCl, 137 mM NaCl, pH 7.4), and tris(hydroxymethyl)amino methane (TRIS; 10 mM, pH 7.1) were purchased from Sigma-Aldrich, Germany. Water used was always DI (Millipore, USA).

Si_3N_4 surfaces. Si_3N_4 test surfaces were fabricated as follows: a thermal silicon dioxide layer (2 μm thickness) was thermally grown over a silicon wafer (500 μm thickness). After that, a 180 nm thick layer of Si_3N_4 was deposited by Low Pressure Chemical Vapor Deposition (LPCVD) technique. The wafer was diced into 10 $\times$ 10 mm^2 pieces to perform the silanization experiments.

Surface silanization. All the test substrates and the sensing chips were cleaned by rinsing with acetone, ethanol, and DI water. After that, substrates were sonicated for 5 min in SDS 1% and flushed with H_2O. Finally, substrates were sonicated for 10 min in HCl and MeOH 1:1. Creation of reactive silanol groups on the Si_3N_4 surface is achieved by keeping the Si_3N_4 substrate for 1 h in an ozone plasma using a UV/Ozone ProCleaner (Bioforce Nanosciences, USA) and 25 min in HNO_3 10% at 75° at reflux conditions and flux with H_2O. After that, Si_3N_4 test substrates were immersed in the appropriate silane solution using different concentrations and different immersing times. The CTES silanized substrates were cleaned with water and dried with N_2. Finally the silane layer was cured in the oven at 110° for 1h.

Biofunctionalization protocols. The bioconjugation of test Si_3N_4 surfaces silanized using CTES was performed by the activation of carboxyl groups, accomplished by using EDC/NHS in a molar ratio of (0.2/0.05) and followed by reaction with a solution of 50 μg/ml of BSA in PBS. Biofunctionalization of EDC-activated surfaces with BSA-FTIC was done in the same way but TRIS was used to avoid salt interferences in the fluorescent analysis. At this moment, we can distinguish two types of biofunctionalization:

In the **ex-situ** biofunctionalization, the reaction is performed out the fluidic

cell, in static mode. The activation of the carboxyl group is carried out by placing a drop of the EDC/NHS allowing to react for 10 min. Afterwards, the sample/chip is rinsed with DI water and immersed in the BSA solution for 1 h.

In the **in-situ** biofunctionalization, the reaction is carried out in the fluidic cell by flowing solutions, at a flow rate of 20 μl/min.

Biodeposition platform. A NanoeNablerTM system (BioForce Nanosciences, USA) was used for the covalent attachment of FTIC-BSA onto the silanized and EDC-activated surfaces. This molecular printing platform enables the direct writing/deposition of 1-60 μm size droplets with a high position resolution (20 nm X, Y, and Z resolution). The size of the deposited drops depends on the contact time and force between the SPT cantilever and the surface being patterned, which are controlled by using a variable intensity laser and a position-sensitive photodetector. Molecules to be printed are loaded into the SPT cantilever reservoirs by pipet (0.5 μl). In this work, SPT tools with rounded edge and 30 μm width were used (SPT-S-C30R). Glycerol is typically used to facilitate the filling of the cantilever channel and reduce the drops evaporation. Relative humidity is adjusted to 50% and the spotted solution was incubated during 1h. The SPT tools were previously cleaned with hot organic solvents and under UV/Ozone cleaner (UV/Ozone ProCleaner TM, BioForce Nanosciences, USA) during at least 40 minutes, which beside cleaning the surface of organic molecules facilitate wettability and fluid flow.

Contact angle analysis. Drop shape analysis was performed with an Easy drop standard (Kruss, Hamburg). Drops were placed on the Si_3N_4 surface with a volume of 3 μl. Each measurement is the average of 10 different measurements done along the characterized Si_3N_4 surface.

Fluorescence analysis. Fluorescent analysis of the patterned surfaces was carried out by an inverted microscope (TE 2000U, Nikon) and a filter set for Cy3TM (Chroma Technology, Vermont) was used to analyze and capture fluorescence images. Images of the same experiment are taken using the same camera exposition parameters for a real comparison between them.

3.2.2 Optimization of the silanization using CTES in test surfaces

Reaction of usual organofunctional alkoxysilanes (sketched in Figure 3.3 A) involves four different steps. Initially, hydrolysis of the alkoxy groups occurs. When the alkoxy groups are hydrolyzed, the condensation to oligomers takes place. After that, oligomers can form hydrogen bonding with the silanol surface that results in a covalent bond after the thermal curing [23]. After the hydrolysis, the resulting silanol groups are more electrophilic and reactive due to the electropositive structure of the silicon, which results in stronger hydrogen bonding. However, this hydrolysis turns the trialkoxyorganosilane reagent in an amphiphilic molecule that easily form vesicles, bundles, or fibers in the condensation step depending on the solvent, giving place to highly irreproducible surfaces [24]. It has been previously observed that solvents having a low dielectric constant (highly hydrophobic) can force organosilane molecules to form reversed micelles or networks or even randomly aggregated silane structures in the solution, therefore reducing the concentration of the silane head groups in the medium which prevents the self-assembled monolayer (SAMs) formation [14].

Taking into account the above considerations, the silanization using an organosilane stable in water can entail several advantages if comparing with standard alkoxysilanes. The steps of hydrolysis and condensation are omitted in the silanization using CTES as it has been sketched in Figure 3.3 B. The clearest advantage is that the formation of a monolayer using CTES is not dependent of the changing atmospheric moisture. The alkoxy groups that protect the cross-linking of silanol groups are not required in CTES silane, due to the strong solvation of CTES molecules in water that stabilizes the solution which, in turn, prevents the polymerization of the silane molecules. Thus, after the interaction of the CTES monomers with the surface, the covalent bond including the cross-linking of silanol groups takes place after the curing process typically at 110° for 1 h [25]. In this context, using water stable silane offers several advantages such as: i) reduction of the silane molecules polymerization, avoiding the buried of the functional groups by the carbon chains, which would make them inaccessible to the biomolecules; ii) formation of homogeneous layers which assures a low roughness of the surface, avoiding losses of light related with the sensor surface irregularity; iii) reduction of the distance between the transducer surface and the biomolecular event due to the formation of single layers, increasing the sensitivity of the detection, in opposition to the multilayer formation.

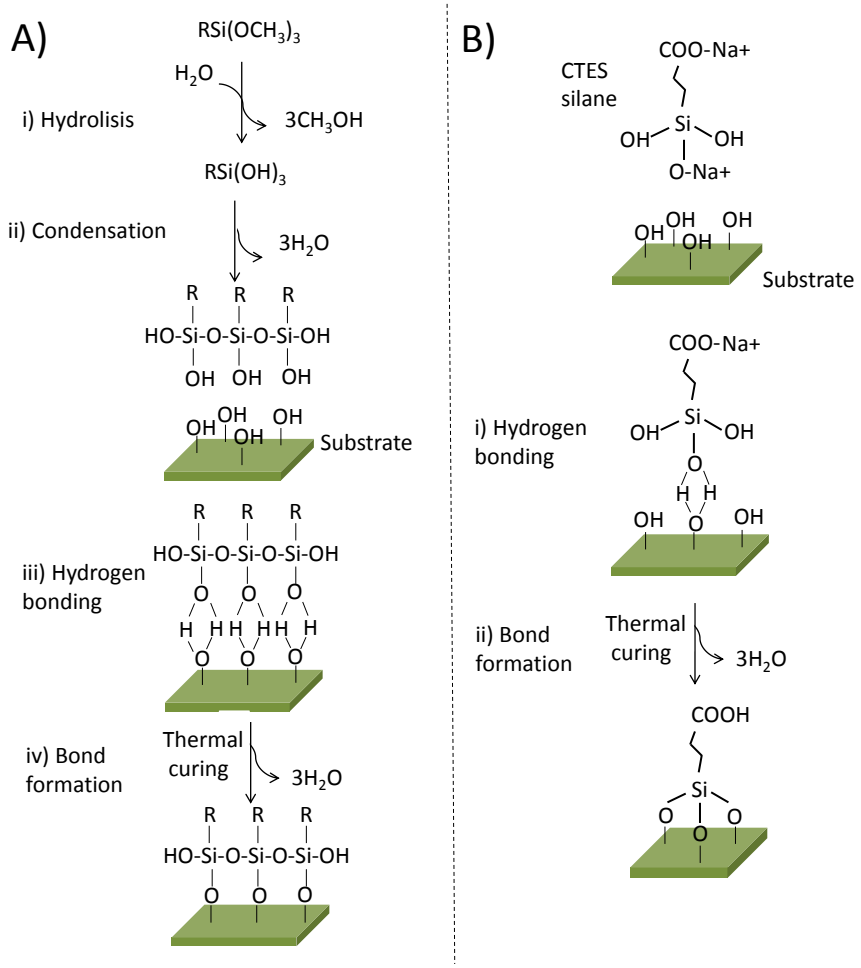

Figure 3.3: Comparison between the different steps of the silanization using a) a trialkoxysilane and b) the CTES silane.

The reaction between the silicon atom from the organofunctional alkoxysilane molecule and the surface requires hydroxyl group generated by oxidation. After that, the bioapplication dictates the functional group desired for the later bioconjugation and consequently the silane needed. As explained before, CTES silane has been chosen for proteomics applications. After the incubation with

the silane, substrates are thermically cured into an oven. In this step, the layer becomes stable due to the condensation between the free silanol groups from the silane molecules and the surface [25]. Prior to the application in the BiMW devices, the optimization of the different steps are previously tried out in Si_3N_4 test surfaces. A sketch of the global silanization scheme employed is shown in Figure 3.4.

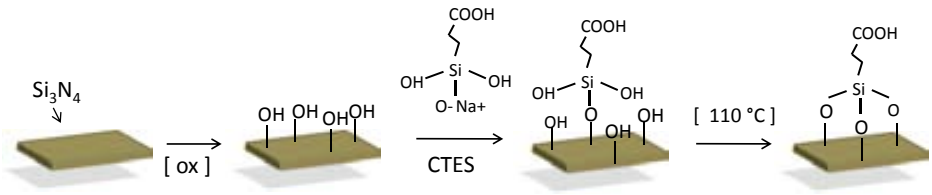

Figure 3.4: Sketch of the overall silanization process using CTES silane.

The silicon nitride surface must be accessible to oxidizing agents to create silanol groups. This aspect is critical to achieve an optimal covering with the silane molecule and therefore, to render in highly reproducible surfaces. With this purpose, the cleaning process must assure the total removal of the contaminants with the minimal damage of the surface. Several cleaning methods are available using different acid, base, organic solvents, or a combination of them as pre-treatment for the silanization [26, 27]. We chose a cleaning process based on three different cleaning steps to be completely sure of the full elimination of the different types of dirtiness (i.e. dust, grease, or inorganic material). The first step is a standard cleaning by rinsing with acetone, ethanol, and DI water (Ac/EtOH/H_2O). In the second step, the Si_3N_4 surface is sonicated in SDS 1% and flushed with water. Finally, the sample is sonicated in HCl and MeOH 1:1 and rinsed with water. The chemical modification of the surface is checked by contact angle analysis. The values corresponding to the different cleaning steps are shown in 3.1. Results demonstrate that the cleaning step (acetone, ethanol, and DI water) is not enough to totally remove contaminants from the sample. It can be noted a reduction in the contact angle after 5 min of sonication treatment with SDS 1% and finally, a homogenization of the clean surface after the sonication with HCl:MeOH. These results are consistent with previous publications [26, 27].

After the cleaning process, the oxidation of the Si_3N_4 test surfaces is es-

Table 3.1: Contact angle values of Si_3N_4 surfaces after each step in the cleaning process.

Cleaning step	Contact Angle (°)
N_2	45 ± 4
Ac/EtOH/H_2O	40 ± 5
SDS 1%	24 ± 6
MeOH : HCl	22 ± 1

sential to make them reactive to the silane molecule. A layer of SiO_2 must be created over the Si_3N_4 surface and activated to have enough silanol groups for the reaction. There is not a standard procedure for the oxidation and activation of a Si_3N_4 surface. Several approaches have been described in the literature. For example, to directly get silanol groups, several strong oxidizing cocktails have been used such as piranha [4], a mix of ammonium chloride and HCl [22], and concentrated HNO_3 [3]. However, these aggressive techniques can damage the surface inducing an increase in the surface roughness, a drawback for waveguide devices. One alternative is using two different steps, first the incorporation of oxygen atoms to the Si_3N_4 surface using a weak oxygen plasma [28, 29] or UV/ozone [30] and afterwards, the activation of this oxide by using a diluted acid solution or water [31]. This procedure will maintain the structural integrity of the optical waveguide device by minimizing the defects produced by the oxidation process on the sensor area surface. In this work, 1 h of UV/ozone has been used to totally oxidize the Si_3N_4 surface, obtaining a highly hydrophilic surface with a contact angle lower than 5 °which indicates the presence of ion species as O^-. After the oxidative step, a solution of 10% of diluted HNO_3 at 75 °C has been used at reflux conditions to activate silanol groups, with a resulting contact angle of 19 °.

In a wet-chemical silanization procedure, the concentration of the silane solution and the reaction time with the surface are important parameters to obtain stable and compact monolayer of CTES, and to avoid the formation of a multilayer structure. To study these parameters, pretreated test samples were immediately immersed in a solution of 1% of CTES silane and were allowed to react for different time periods ranging from 5 to 1200 min. Samples were then cleaned with water and placed for 1h in an oven at 110 °C for a thermal curing step. Then, the contact angles for the different immersion times of samples in silane solution were evaluated. Values are shown in Table 3.2. The contact

Table 3.2: Contact angle values of silanized samples for different times using a 1% CTES solution and after immersion for 1 h in a solution of 50 μg/ml of BSA in PBS.

Time (min)	CTES (°)	BSA (°)
5	49.3±3	65± 5
15	49.8±2	-
30	55.2±3	70±11
60	56.6±6	-
120	54±5	60±8
300	56.7±11	70.3±8
1200	43.2±3	42.2 ±8

angle of silanized Si_3N_4 test surfaces reaches a maximum after 1 h of immersion in the CTES solution and decreases for longer silanization times. The pH is another important factor to control in order to avoid cross-linking; it seems that only basic pH gives packaged monolayers, probably due to the condensation of CTES silane molecules when alkoxy groups are protonated in acidic conditions.

Afterwards, we checked the applicability of this protocol for the covalent attachment of biomolecules. The covalent binding of the biomolecules over the CTES silanized surface was done through the activation of the carboxyl group by the use of EDC/NHS and the later reaction with the amino groups of the biomolecules to form a peptidic bond [15]. Thus, the previously silanized samples were activated by immersing them in an aqueous EDC/NHS solution of a molar ratio of 0.2/0.05 for 10 min. Then, the samples were rinsed with water, dried with N_2, and immersed into a solution of 50 μg/ml of BSA in PBS for 1 h. Due to the strong adsorption of BSA on the Si_3N_4 test surfaces it was necessary to clean the sample with SDS 1% and HCl 0.1 M to remove all the non-covalently attached proteins. As shown in Table 3.2, proteins are detached from the 12 h sample indicating that they were physically adsorbed. Thus, it can be confirmed that the total coverage of the Si_3N_4 surface was achieved with 1 h of silanization time and that longer immersion times have negative effects for the formation of the silane layer. This fact can be explained by the instability of the hydrogen bonding between the silanol groups and the CTES molecule, where silanol groups slowly come back to the silicon net and are not able to compete for a long time with the strong hydrogen bridges that form the CTES molecule with water. Thus, CTES molecule is detached from surface and solved again in the water for times larger than 1 h.

Table 3.3: Contact angle values and AFM (roughness) characterization of silanized surfaces for 1 h using different silane concentrations.

[CTES]	Contact Angle (°)	Roughness(Å)
0%	31 ± 1	1.5
0.2%	36 ± 2	6
0.5%	49 ± 1	1.2
2%	47 ± 2	1

The concentration of CTES in the aqueous solution also plays a crucial role in the formation of a well packaged single layer of silanes. Closely packed layers are effective in preventing water penetration, and have demonstrated better stability in saline environments [5]. To find the optimum silane concentration, oxidized Si_3N_4 surfaces are placed in different concentrations of CTES solutions ranging from 0% to 2%, maintaining the silanization time fixed to 1 h. The resulting silanized surfaces are characterized by contact angle (see Table 3.3) and by AFM (see Figure 3.5). AFM analysis reveals that a concentration of 0.2% does not totally cover the Si_3N_4 surface as it can be noted by an increase in the roughness, due to the partial covering of the surface and to the length of the CTES molecule. However, the reduction of the roughness and a maximum in the contact angle indicate that a concentration of 0.5% is enough to totally cover the Si_3N_4 surface. The contact angle corresponding to the silanized surface using 0.5% CTES solution and 1 h of immersion time is 49°. Therefore, this contact angle value will be considered as a reference to assess the success of the silanization process when functionalizing a silicon-based device.

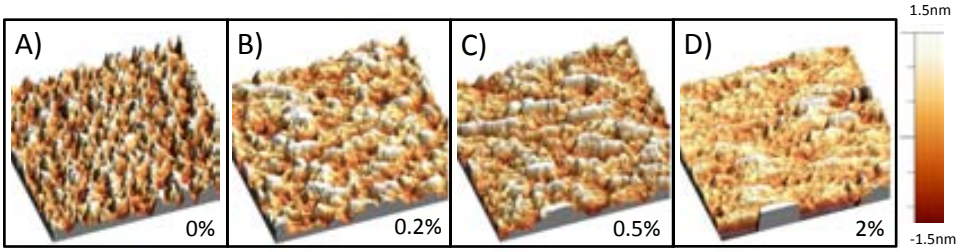

Figure 3.5: AFM tapping analysis of Si_3N_4 substrates immersed for 1 h into different concentrations of CTES.

Once the optimal silanization conditions have been found, control experi-

ments are done to confirm the covalent binding of biomolecules over the CTES silanized surfaces, checking the surface coverage through the surface contact angle. A solution of the protein BSA is deposited onto two Si_3N_4 test surfaces, one of them is previously cleaned and silanized with CTES solution with the optimized conditions (1 h, 0.5%), while the other is just cleaned omitting the silanization step. After, the same treatment is done on the silanized and non-silanized samples: surface activation by the use of EDC/NHS followed by immersion in a BSA protein solution, 50 μg/ml, during 1 h. After the protein incubation for both samples, silanized and bare Si_3N_4 the showed similar contact angles, (70±2)° and (68±3)°, respectively. However, after cleaning by flushing HCl 0.1 M and SDS 1%, the contact angle of the non-silanized samples fell down to (40±2)°. On the contrary, the contact angle of the silanized surface biofunctionalized with BSA is kept constant. These results demonstrate: i) the detachment of non-covalently bonded protein when the sample is subjected to harsh conditions and ii) the suitability of the silanization method for the covalent attachment of proteins.

To check the applicability of the bioconjugation protocol to the patterning of biomolecules, a biodeposition system is employed to selectively biofunctionalize an area of the surface with FTIC-BSA. Two silanized Si_3N_4 surfaces are employed. In one of the samples, carboxyl groups are activated by the use of EDC/NHS, while the other one is just immersed in water after the silanization. After that, the biodeposition system is employed to pattern the samples with FTIC-BSA and allowed to react for 1 h. Then, a cleaning step is done by fluxing the sample with water. As can be seen in Figure 3.6 A, whereas in the carboxyl-activated sample FTIC-BSA shows a good attachment, in the non-activated sample (see Figure 3.6 B) almost all the proteins are detached from the Si_3N_4 surface. This indicates that covalent bonding between carboxyl group and FTIC-BSA has been achieved through EDC/NHS activation, whereas weak adsorption occurred on the silanized Si_3N_4 surface. The biodeposition platform is very useful in order to contrast the fluorescent spot with the surrounding surface, that acts as a reference. In this experiment, we also demonstrate that the bioconjugation protocol can be combined with the selective surface patterning by using a deposition platform.

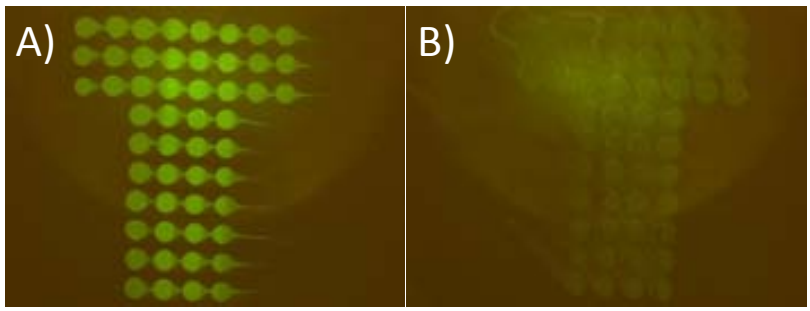

Figure 3.6: Fluorescent analysis images of FTIC-BSA deposited on silanized surfaces by a commercial biodeposition system. A) Activated silanized surface and B) non-activated silanized surface.

3.2.3 Application of the silanization protocol using CTES to a BiMW device

The final goal of this work is to apply the water-silanization protocol to attach a biological receptor layer onto the Si_3N_4 surface of a BiMW device to develop high performance biosensors. To monitor the sensor surface modification, the chip is placed in the experimental set-up after its silanization and encapsulated with the fluidic cell. After that, all the solutions needed for the activation and functionalization of the surface are flowed over the surface by injecting a constant volume of the sample into the fluid cell at a fixed flow rate. The chosen fluid channel size and flow rate ensure a laminar flow over the BiMW sensor. The progress of the biofunctionalization procedure was assessed in real-time by the analysis of the interferometric signals of the BiMW sensor. In particular, the monitoring of the bioreceptor binding to the Si_3N_4 surface provides valuable information about the efficiency of the biofunctionalization process. The interferometric signal of the covalent attachment of the BSA protein to the sensor area of the BiMW device is shown in Figure 3.7 A.

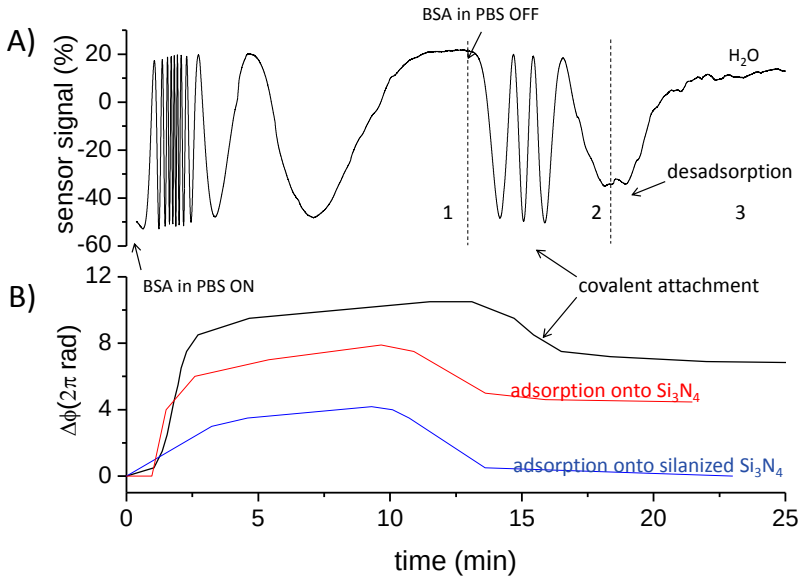

Figure 3.7: a) Real-time interferometric signal of the covalent attachment of 50 μg/ml of BSA to an activated surface and, b) signals due to the immobilization of BSA onto different surfaces (activated, silanized, and bare Si_3N_4) where interferometric graphs has been transformed into phase signals (2 π rad).

To carry out this experiment, The BiMW chip is silanized using the CTES silane with the previously optimized protocol. Then, the carboxyl groups are activated by inyecting 250 μl of EDC/NHS, immediately followed by an injection of 250 μl of BSA at a concentration of 50 μg/ml. During all the experiment a water flow is maintained at a constant rate of 20 μl/min. The interferometric signal corresponding to a binding process and/or to a change of the bulk refractive index could be difficult to interpret by a non-experienced user. By a post-processing of this signal, it is possible to obtain an easier and "common-type" graph. Values of the output signal variation (y axis) can be converted into phase signal (radians) to transform a sinusoidal signal into a linear signal (see in Figure 3.7 B).

Three different regimes can be recognized in the interferometric detection signal. Since the entrance of the BSA in PBS to its exit (region 1) the signal is due to two factors: i) the variation of bulk refractive index between the contin-

uous water flow and the PBS containing the protein and ii) the immobilization of the protein on the transducer surface. Afterwards, when the BSA in PBS is going out from the fluidic channel and the water is coming in, the signal is only due to the change in bulk refractive index between PBS and water (region 2). Finally, water flow induces desorption of non-covalent attached BSA (region 3).

To investigate the nonfouling behavior of the CTES silane layer, another channel of the same silanized chip is used to evaluate the adsorption of BSA onto the silanized BiMW sensor area. In this experiment, the same conditions used for the covalent attachment are employed but the activation step is omitted. Then, 250 μl of BSA at a concentration of 50 μg/ml are flowed over the sensor area at a constant rate of 20 μl/min through the fluidic cell. The nonspecific adsorption of BSA onto the silanized sensor area is negligible, as it can be seen in Figure 3.7. This indicates the formation of a stable and compact silane layer and confirms that the signal obtained in the previous experiment is due to the covalent attachment. In opposition, BSA was strongly adsorbed when it was flowed over the bare sensor area of an identical BiMW device using the same experimental conditions [32]. The interferometric signal corresponding to the physical adsorption of BSA is shown in Figure 3.7 B for a direct comparison. The net change is larger in the case of protein covalent attachment using the silanization procedure ($6.81\times2\pi$ rad) than for the direct protein adsorption over bare Si_3N_4 surface ($4.41\times2\pi$ rad). This indicates that the highest protein coverage is reached with the covalent strategy. The lower signal obtained for the direct adsorption of the protein can be explained by an incomplete covering of the surface, which produces a non-uniform protein layer, leaving holes that can induce the unselective adsorption of biomolecules during the biorecognition process. Moreover, strong interactions with the surface can cause conformational changes in the proteins and the consequent loose of functionality of the receptor layer, whereas weak interactions with the surface entail the possibility of desorption of the biorector layer due to the liquid flow [33].

For the in-flow strategy, the silanized chip was placed on the optical set-up and the solutions were flowed through the fluidic cell using the same parameters than in the previous section. On the other hand, to immobilize the biomolecules by the micro-patterning strategy, the silanized chip was activated by immersion in an EDC/NHS solution for 10 min and the sensor area was filled with a mix solution of 50 μg/ml BSA and glycerol 1% by the biodeposition system and allowed to react for 1 h, at room temperature and under a 50% ambient humidity.

At this point, it is possible to evaluate the quality of the bioreceptor layers by the interferometric detection of the specific monoclonal antibody (anti-BSA) and the immobilized BSA protein. To perform the detection, PBS is flowed at constant rate of 20 μl/min over the sensor area and a 250 μl solution of 3 nM anti-BSA is injected. After the biorecognition event, the bioreceptor surface is recovered by the use of a regeneration solution, due to the disruption of the antigen-antibody bond. A total regeneration is achieved by the injection of HCl 20 mM, allowing multiple detections using the initial state of the bioreceptor layer. The interferometric signals obtained for the biointeraction with the anti-BSA before and after the regeneration of the bioreceptor surface, using both immobilization procedures, in-flow and patterning, are shown in Figure 3.8 A and B, respectively. In both cases, the response of the sensor indicates the affinity of the receptor layer for the antibody providing high sensitivity to the detection. Moreover, the injection of a non-specific antibody at the same concentration (3 nM anti-hGH) did not produce any interferometric response ($\Delta\Phi \times 2\pi = 0$) in any of the sensor areas (data not shown) in agreement with previous experiments. The same experiment is done over the silanized sensor area where BSA is flowed, obtaining negligible signals for both specific and unspecific antibodies. These results demonstrate the specificity of the layer, the high protein packaging, and the low adsorption of biomolecules over the silane layer. The regeneration of the BSA bioreceptor layer points out the stability of the covalent linkage in both the silanization and the biofunctionalization procedures. However, it can be observed that the signal obtained when the BSA protein is immobilized using the biodeposition system ($0.45\times2\pi$ rad) is higher than the one obtained with the in-flow immobilization ($0.29\times2\pi$ rad). This is probably due to the reorganization capacity of the protein layer when it is allowed to react with the surface in static conditions instead of in-flow. Although selectivity and stability of the bioreceptor layer is excellent using both immobilization strategies, static conditions are preferred to enhance the signal obtained for the BiMW biosensor for a given analyte concentration due to an increase in the number of available binding sites.

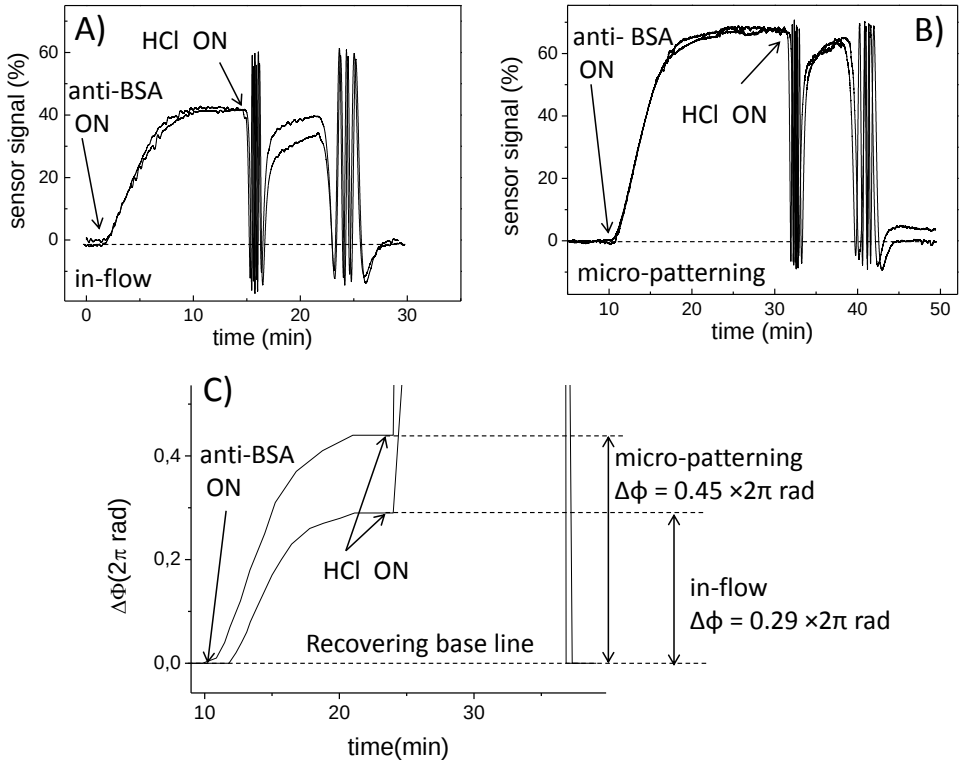

Figure 3.8: Real-time monitoring of the phase change due to the injection of 3 nM anti-BSA and the regeneration of the surface using both biofunctionalization strategies, A) in-flow, B) using the biodeposition system, and C) comparison between both strategies (signals have been transformed into phase signals $\times 2\pi$).

3.3 Surface modi cation using a thiol-terminated silane (MPTS)

For biological receptors which do not contain available amino groups a suitable silane must be employed such as the 3-methacryloxypropyl tris(trimethylsiloxy)silane (MPTS). This silane has been widely employed in silicon oxide surfaces to achieve a covalent immobilization of for example, thiol-terminated DNA oligonu-

cleotides on self-assembled layers by disulfide bond formation [34, 35]. It has also been for an immunoassay for the detection of avian influenza through whole virus capture [36]. The main advantage of MPTS is the direct attachment of SH-modified DNA to the thiol functional group of the silane by a strong and stable disulfide bond without further mediators. MPTS has been widely used by the scientific community [25] and its applicability for biosensing has already been demonstrated. Therefore, we have carried out a straight forward study in which basic parameters are optimized such as the concentration of the silane solution and the immersion time. The silanized test surfaces are tested by fluorescent analysis.

3.3.1 Materials and methods

Reactives. MPTS, toluene, formamide, phosphate buffer (PB; 50mM phosphate,0.5 M NaCl, pH 7), and the sodium citrate buffer (SSC 5×; 0.75 M NaCl, 0.075 M sodium citrate) were purchased from Sigma-Aldrich, Germany. Oligonucleotides SH-DFO-Cy (Cy-DNA), 5' modified with thiol and 3' modified with Cy3, were purchased from IBA, Germany. The DNA oligonucleotides sequence was (THIOL)AGA AGA AGA AGA TAA ATT ATT CCA(CY3). Other reactives employed have been already specified in the previous section.

Surface silanization. The pretreatment of the sample (cleaning and oxidation processes) is the same that described for the CTES silanization procedure. After the immersion of the samples in the MPTS solution, silanized substrates are cleaned by consecutive rinsing of toluene, acetone, ethanol, and water. Then, the samples are cured for 3 h in oven at a temperature of 110 °C.

Biofunctionalization. The bioconjugation of silanized surfaces using MPTS is done by the use of Cy-DNA 1 μM in PB with an incubation time of 1 h.

Contact angle analysis. In previous experiments, it was found a strong adsorption of toluene on bare Si_3N_4 surfaces that causes an increase of the contact angle values. Thus, contact angle measurements are not useful to check the silanization procedure using MPTS.

Fluorescence analysis. Silanized surfaces by different conditions are allowed to react with SH-modified DNA that has been labeled with a dye (SH-DFO-Cy3).

3.3.2 Optimization of the silanization of the sensor area using MPTS in test surfaces

The overall silanization process using MPTS silane (see Figure 3.9) is quite similar to the one with the silane. The pretreatment of the test surfaces consisting in the cleaning and the oxidation is followed by the immersion of the samples in the MPTS solution. After that, the silanized samples are cured on oven for 3 h at 110°C.

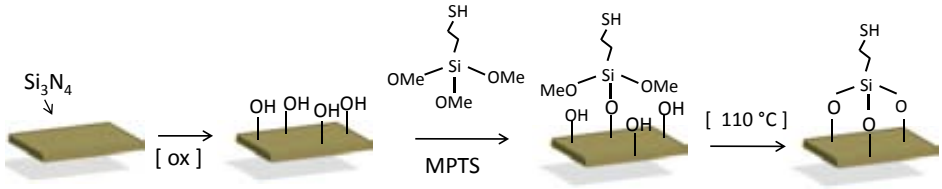

Figure 3.9: Scheme of the silanization process using MPTS silane.

Pretreated samples are immersed in a fixed concentration of MPTS at 10% in toluene for different immersion times. After the curing treatment, samples are incubated with the Cy-DNA allowing to the thiol group of the syntethic DNA to react with the silanized surface. The fluorescent analysis of the bioconjugation of the labeled Cy-DNA with Si_3N_4 surfaces silanized with MPTS at a fixed concentration of 10% for different incubation times is shown in Figure 3.10. It can be seen that the overnight incubated surface shows the best covering of Cy-DNA. On the contrary that for the case of CTES silanization, long immersion times in the MPTS solution are clearly better than short times. This fact is probably due to a slower reaction velocity of the reaction between the silane and the surface.

Figure 3.10: Fluorescent analysis of Cy-DNA attached to silanized surfaces during different times of MPTS incubation. A) 1 h, B) 3 h and C) overnight.

Once the optimum silanization time has been determined, different MPTS silane concentrations have been tested for overnight incubation. Pretreated samples are immersed in MPTS solutions at concentrations ranging from 0.5% to 25% in toluene. Fluorescent analysis of the samples is showed in Figure 3.11. Images do not indicate a gradual increase of the fluorescence as could be expected, but a sudden increase of the fluorescence from 12.5% indicating that this silanization procedure is relatively independent of silane concentrations, corroborating a previous work [25].

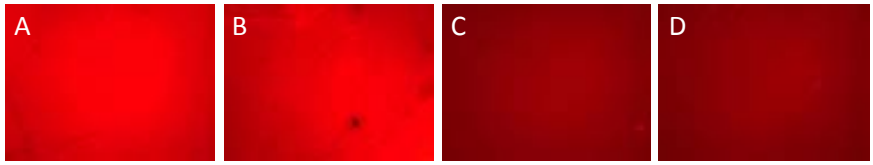

Figure 3.11: Fluorescent analysis of Cy-DNA deposited on silanized surfaces using different concentrations of MPTS. A) 25%, B) 12.5%, C) 6.25%, and D) 0.5%.

Control experiments have been performed to validate the fluorescence analysis as the suitable technique for the characterization of bioconjugated surfaces. Control samples are undergone to different treatments representing the different steps in the silanization process. The results of these experiments are shown in Figure 3.12. For the first experiment (Image A) a clean Si_3N_4 is immersed for 1 h in PB buffer, demonstrating that fluorescence is not due to the interference of salts on the surface. Second experiment (Image B) induces the adsorption of the Cy-DNA onto a cleaned Si_3N_4 surface. It can be noted that Cy-DNA presents low physical adsorption onto the Si_3N_4 surface. Image C displays the Cy-DNA adsorption onto an oxidized Si_3N_4 surface that has been previously immersed in a toluene solution overnight in order to demonstrate that adsorbed toluene is not interfering the covalent attachment. In image D, the optimized protocol for the MPTS silanization is reproduced (10% in MPTS concentration overnight) but the thermal curing is omitted. Finally in image E, the entire protocol has been repeated including the thermal curing, showing a high bioconjugation with the labeled DNA. As it has been demonstrated, the fluorescence is only due to the covalent attachment of Cys-DNA. It has been also noted that thermal curing is an crucial parameter for this silanization procedure.

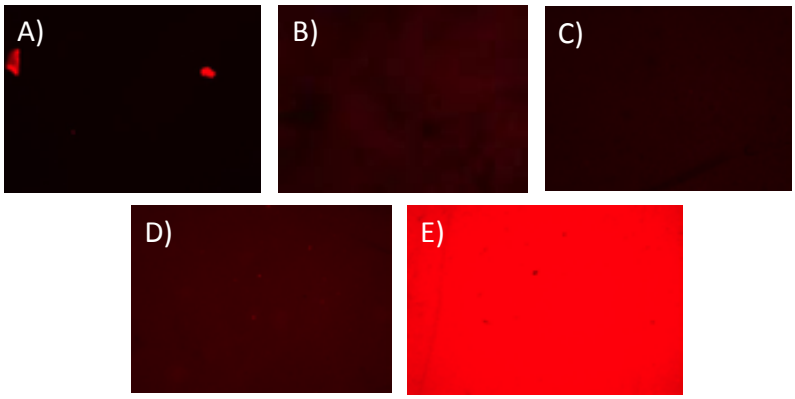

Figure 3.12: Fluorescent analysis of control experiments for the covalent attachment of Cys-DNA to the silanized surface. A) Clean sample immersed for 1 h in PB, B) adsorption of Cys-DNA onto a clean sample, C) adsorption of Cys-DNA onto a oxidized sample previously immersed in toluene overnight, D) optimized protocol reproduced without the thermal curing step, and E) completed optimized protocol reproduced.

3.3.3 Application of the silanization protocol using MPTS to a BiMW device

In the same way that with the CTES silane, the silanization protocol using MPTS is demonstrated by the detection of a target nucleotide sequence after immobilizing a DNA sequence on the sensor area of a BiMW device. To carry out this experiment, The BiMW chip is silanized using the MPTS silane with the previously optimized protocol and placed on the experimental set-up. Then, the DNA sequence is immobilized by injecting 250 μl of the receptor sequence at a concentration of 1μM in PB at a constant rate of 5 μl/min. Then, SSC 5$\times$ buffer is employed at a constant rate of 20 μl/min to perform the biodetection. The detection of a 50 nM concentration of the target sequence and the regeneration of the baseline by the use of a regeneration solution (Formamide 35% in water) are shown in Figure 3.13 demonstrating the biosensing capabilities of the optimized silanization protocol.

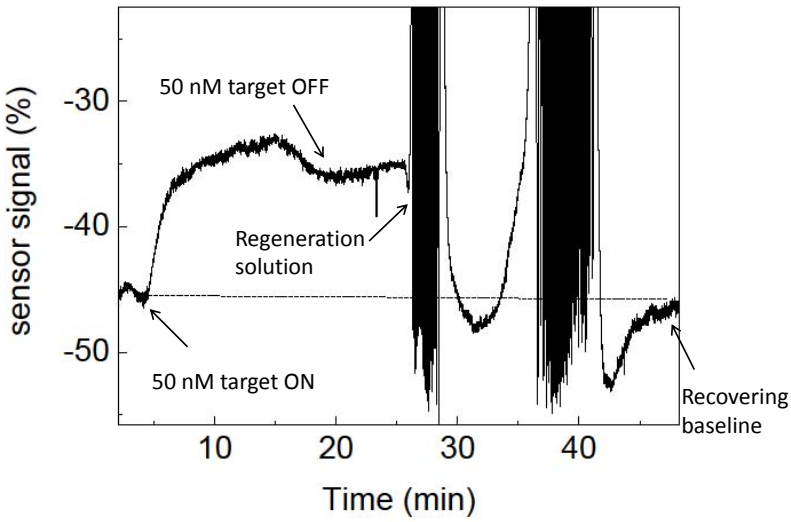

Figure 3.13: Detection of a 50 nM concentration of a target DNA sequence complementary to a immobilized DNA hairpin structure and the regeneration process.

3.4 Conclusions

This chapter showed the optimization of a bioconjugation process using CTES and MPTS, as linkers between the Si_3N_4 surface and the biomolecules for developing biosensors able to recognize a wide range of analytes using the BiMW device.

It has been demonstrated that a complete CTES silane monolayer is assembled onto the Si_3N_4 test samples when it is used at a concentration 0.5 % and for 1 h of immersion time in aqueous solution, obtaining a contact angle of 49 °. The suitability of the optimized protocol for biosensing applications is checked by the real-time monitoring of the processes occurring on the sensor area of a BiMW device. Results indicate that the developed silanization protocol is highly efficient to cover the sensor area and to protect the Si3N4 sensor area from unspecific interactions. Two common strategies for the bioconjugation of the receptor in biosensing, the in-flow and the microdeposition patterning, are assessed for biosensing applications using the developed silanization protocol.

In both cases, results indicate the high reproducibility and selectivity of the biodetection as well as the stability of the covalent attachment that allows the regeneration of the bioreceptor layer. The highest signal is obtained when the receptor layer is immobilized using the deposition system, demonstrating a better package of proteins when they are allowed to link with the silane in static conditions instead of in-flow. The results demonstrate that this water-based tethering method can be very useful to link the bioreceptor layer on different types of silicon-based devices in order to enhance its biosensing capabilities.

A thiol-terminated silane (MPTS) has been employed to attach SH-modified DNA on the Si_3N_4 due to the strong disulfide bond that is produced between both. The best covering of the surface with the MPTS silane is achieved for long silanization times (overnight) indicating a slow kinetics reaction. MPTS silanization is relatively independent from the concentration of silane when this is used above the 10%. It has been shown that in the silanization procedure using MPTS, the thermal curing is necessary. This silanization method has been applied to a sensor area of a BiMW device, demonstrating the applicability of this for biosensing.

Bibliography

[1] M. Mujika, Aran S, E. Castano, M. Tijero, R. Vilares, J. M. Ruano-Lopez, A. Cruz, L. Sainz, and J. Berganza. Magnetoresistive immunosensor for the detection of escherichia coli O157:H7 including a microfluidic network. *Biosens. Bioelectron.*, 24:1253 1258, 2009.

[2] B. Sepulveda, J. Sanchez del R o, M. Moreno, F. J. Blanco, K. Mayora, C. Dom nguez, and L. M. Lechuga. Optical biosensor microsystems based on teh integration of highly sensitive mach-zehnder interferometer devices. *J. Opt. A: Pure Appl. Opt.*, 8:S561 S566, 2006.

[3] Renny Edwin Fernandez, Enakshi Bhattacharya, and Anju Chadha. Covalent immobilization of pseudomonas cepacia lipase on semiconducting materials. *Appl. Surf. Sci.*, 254:4512 4519, 2008.

[4] Jinpian Diao, Dacheng Ren, James R. Engstrom, and Kelvin H. Lee. A surface modification strategy on silicon nitride for developing biosensors. *Anal. Biochem.*, 343:322 328, 2005.

[5] Anfeng Wang, Haiying Tang, Ting Cao, Steven O. Salley, and K.Y. Simon Ng. In vitro stability study of organosilane self-assemble monolayers and multilayers. *Journal of Colloid and Interface Science*, 291(2):438 447, 2005".

[6] J. Kim, P. Seidler, L. S. Wan, and C. Fill. Formation, structure, and reactivity of amino-terminated organic films on silicon substrates. *Journal of Colloid and Interface Science*, 329(1):114 119, 2009.

[7] Ahmed Arafat, Marcel Giesbers, Michel Rosso, Ernst J. Rl Sudholter, Karin Schoroen, Richard G. White, Li Yang, Matthew R. Lindord, and Han Zuilhof. Covalent biofunctionalization of silicon nitride surfaces. *Langmuir*, 23:6233 6244, 2007.

[8] A. Cricenti, G. Longo, M. Luce, R. Generosi, P. Perfetti, D. Vobornik, G. Margaritondo, P. Thielen, J.S. Sanghera, I.D. Aggarwal, J.K. Miller, N.H. Tolk, D.W. Piston, F. Cattaruzza, A. Flamini, T. Prosperi, and A. Mezzi. AFM and SNOM characterization of carboxylic acid terminated silicon and silicon nitride surfaces. *Surf. Sci.*, 544:51 57, 2003.

[9] Fabrizio Cattaruzza, Antonio Cricenti, Alberto Flamini, Marco Girasole, Gianni Longo, Alessio Mezzi, and Tommaso Prosperi. Carboxylic acid terminated monolayer formation on crystalline silicon and silicon nitride surfaces. a surface coverage determination with a fluorescent probe in solution. *J. Mater. Chem.*, 14:1461 1468, 2004.

[10] Daisuke Nagao, Mikio Yokoyama, Shu Saeki, Yoshio Kobayashi, and Mikio Konno. Preparation of composite particles with magnetic silica core and fluorescent polymer shell. *Colloid Polym. Sci.*, 286:959 964, 2008.

[11] Chung-Ta Tsai, Yu-Chi Pan, Chun-Chiang Ting, Shanmugam Vetrivel, Anthony S. T. Chiang, george T. K. Fey, and Hsien-Ming Kao. A simple one-pot route to mesoporous silicas SBA-15 functionalized with exceptioanlly high loadings of pendant carboxiylic acid groups. *ChemComm*, pages 5018 5020, 2009.

[12] Lu Han, Yasuhiro Sakamoto, Osamu Terasaki, Yongsheng Li, and Shunai Che. Synthesis of carboxylic group functionalized mesoporous silicas (CFMSs) with various structures. *J. Mater. Chem.*, 17(1216 1221), 2006.

[13] Ying Chen, Pengcheng Xu, Min Liu, and Xinxin Li. Bio/chemical detection in liquid with self-sensing Pr-Oxi-Lever (piezo-resistive SiO_2 cantilever sensors. *Micromech. Microeng.*, 87:2468 2474, 2010.

[14] Gokhan Demirel, Mustafa O. Ca glayan, Bora Garipcan, and Erhan Piskin. A novel DNA biosensor based on ellipsometry. *Surface Science*.

[15] T. W. Grahan Solomons. *Organic Chemistry*. John Wiley & Sons, inc., fifth edition edition, 1992.

[16] J. Trevino, A. Calle, J.M. Rodr guez-Frade, M. Mellado, and L.M. Lechuga. Determination of human growth hormone in human serum samples by surface plasmon resonance immunoassay. *Talanta*, 78:1011 1016, 2001.

[17] Nikin Ptel, Martyn C. Davies, Mark Hartshorne, Richard J. Heaton, Clive J. Roberts, Saul J. B. Tendler, and Philip M. Williams. Immobilization of protein molecules onto homogeneous and mixed carboxylate-terminated self-assembled monolayers. *Langmuir*, 13:6485 6490, 1997.

[18] R.G. Chapman, E. Ostuni, L. Yan, and G.M. Whitesides. Preparation of mixed self-assembled monolayers (SAMs) that resist adsorption of proteins using the reaction of amines with a sam that presents interchain carboxylic anhydride groups. *Langmuir*, 16:6927 36, 2000.

[19] Shuichi Takayama, J. Cooper McDonald, Emanuele Ostuni Michael N. Liang, Paul J. A. Kenis, Rustem F. Ismagilov, and George M. Whitesides. Patterning cells and their environments using multiple laminar fluid flows in capillary networks. *PNAS*, 96, 1999.

[20] Tohid Fatanat Didar, Amir M. Foudeh, and Maryam Tabrizian. Patterning multiplex protein microarrays in a single microfluidic channel. *Anal. Chem.*, 84, 2011.

[21] Bernhard H. Weigl and Paul Yager. Microfluidic diffusion-based separation and detection. *Science*, 283:346 347, 1999.

[22] Ketul C. Popat, Sadhana Sharma, Robert W. Johnson, and Tejal A. Desai. Afm analysis of organic silane thin films for biomems applications. *Surf. Interface Anal.*, 35:205 215, 2003.

[23] *A silane primer: chemistry and applications of alkoxy silanes*, volume 65 of *822*. Federation of Societies for Coatings Technology, 1993.

[24] Oana M. Martin, Lian Yu, and Sandro Mecozzi. Solution self-assembly and solid state properties of fluorinated amphiphilic calix[4]arenes. *Chemical Communications*.

[25] Catherine M. Halliwell and Anthony E. G. Cass. A factorial analysis of silanization conditions for the immobilization of oligonucleotides on glass surfaces. *Anal. Chem.*, 73:2476 2483, 2001.

[26] J. J. Cras, C. A. Rowe-Taitt, D. A. Nivens, and F. S. Ligler. Comparison of chemical cleaning methods of glass in preparation for silanization. *Biosens. Bioelectron.*, 14:683 688, 1999.

[27] Y. Hand, D. Mayer, A. Offenhausser, and S. Ingebrandt. Surface activation of thin silicon oxides by wet cleaning and silanization. *Thin Solid Films*, 510:175 180, 2006.

[28] Sukdeb Pal, Min Jung Kim, and Joon Myong Song. Quantitation of surface coverage of oligonucleotides bound to chip surfaces: a fluorescence-based approach using alkaline phosphatase digestion. *Lab Chip*, 8:1332 1341, 2008.

[29] Stephanie Dauphas, Soraya Ababou-Girard, Aurelie Girard, France Le Bihan, Tayeb Mohammed-Brahim, Veronique Vie, Anne Corlu, Christiane Guguen-Guillouzo, Olivier Lavastre, and Florence Geneste. Stepwise functionalization of SiN_x surfaces for covalent immobilization of antibodies. *Thin Solid Films*, 517:6016 6022, 2009.

[30] Stefan Spirk, Heike M. Ehmann, Rupert Kargl, Natascha Hurkes, Martin Reischl, Jiri Novak, Roland Resel, Ming Wu, Rudolf Pietschnig, and Volker Ribitsch. Surface modifications using a water-stable silanetriol in neutral aqueous media. *Appl. Mater. Interfaces*, 2(10):2956 2962, 2010.

[31] Mary Manning and Gareth Redmond. Formation and characterization of DNA microarray at silicon nitride substrates. *Langmuir*, 21:395 402, 2005.

[32] Kirill E. Zinoviev, Ana Belen Gonzalez-Guerrero, Carlos Dom nguez, and Laura M. Lechuga. Integrated bimodal waveguide interferometric biosensor for label-free analysis. *J. Lightwave Tech.*, 2011. In Press.

[33] Philippe Dejardin. *Proteins at Solid-Liquid Interfaces*. Springer, 2006.

[34] Ralf Lenigk, Maria Carles, Nancy Y. Ip, and Nikolaus J. Sucher. Surface characterization of a silicon-chip-based DNA microarray. *Langmuir*, 17:2497 2501, 2001.

[35] Andrea Alessandrini, Valentina De Renzi, Lorenzo Berti, Imrich Barak, and Paolo Facci. Chemically homogeneous, silylated surface for effective DNA binding and hybridization. *Surface Science*, 582(1-3):202 208, 2005.

[36] Jie Xu, David Suarez, and David S. Gottfried. Detection of avian influenza virus using an interferometric biosensor. *Anal. Bioanal. Chem.*, 389:1193 1199, 2007.

Chapter 4

Proteomic applications for the BiMW biosensor: human Growth Hormone and Pseudomona bacteria detection

> "When proteins, antibodies and other biological molecules kiss, biosensor can tell."
>
> *Vanderbilt University (2007, September 20).*

4.1 Introduction

Proteins are involved in a large number of processes in the human body which include structural, transport, hormonal, or enzymatic functions. Proteins that are either overexpressed or underexpressed are early indicators of biological states

and could be used as potential diagnostic/prognostic biomarkers associated with diseases. They are also present in the outer membrane of some microorganism, which make proteins potential targets for the detection of pathogens. In this context, the effective prevention and diagnosis of many diseases depend on the ability to quantitatively measure protein from clinical samples as well as from air, food, or water at very low concentrations [1]. In this chapter, we develop a BiMW biosensor to investigate the proteomics applications of this device for the detection of a protein, the human growth hormone (hGH) and for the detection of the bacteria (Pseudomona) through its membrane proteins.

4.1.1 The immunoassay

An antibody (Ab) is a large Y-shaped protein generated by the immune system to identify and to neutralize foreign substances introduced in a living organism. Antibodies are heavy (150 KDa) globular plasma proteins consisting of a basic constant functional unit and a variable region as it can be seen in Figure 4.1. The basic region is an immunoglobulin (Ig) monomer, but the secreted antibodies can also be dimeric, tetrameric, or pentameric with two, four, and five Ig units, respectively. The variable region of the antibody is located at its arms and allows the generation of millions of antibodies with slightly different tip structures, or antigen binding sites. Then, each tip of the "Y" of an antibody contains a paratope (a structure analogous to a lock) that is specific for one particular epitope (similarly analogous to a key) on an antigen, allowing these two structures to bind together with precision (see Figure 4.1).

The affinity of an antibody for an antigen is determined by the combination of physical forces, hydrophobic interactions, hydrogen bonds, and van der Waals interaction, whereas the specificity of the antibody depends on the relative affinity for the antigen and the binding sites of the antibody. The specificity of the antibody can give place to cross-reactivity if this presents affinity in different degrees for more than one antigen. The properties of the antigen-antibody interaction determine the selectivity and sensitivity of the immunoassay.

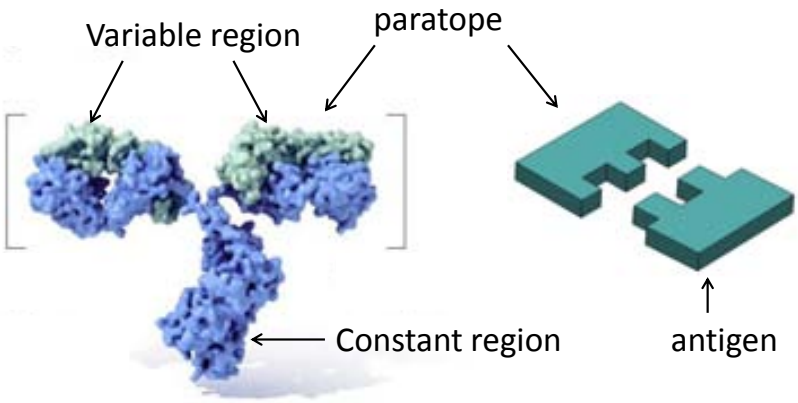

Figure 4.1: Basic structural units of an antibody.

The large and diverse population of antibodies is generated by random combinations of a set of gene segments that encode different antigen binding sites, followed by random combinations in this area of the antibody gene, which create further diversity. Antibodies are normally generated in animals repeatedly exposed to the antigen of interest. As a result, a large number of antibodies are produced with different specificities and epitope affinities, known as **polyclonal antibodies** (pAb) (see Figure 4.2 A). Then, the serum of the animal is extracted, purified, and stored.

High affinity antibodies can be produced by the fusion of spleen cells from the immune animal with neoplastic B cells (normally a B cell line derived from a tumour). From this fusion, hybrid cells are produced (hybridomas) which exhibit characteristics of both parent cells. Such hybridomas secrete antibodies of a specificity shown by the immune donor and are also immortal (a characteristic of the neoplastic B cell line). Thus, the B lymphocyte produces immunoglobulin of only one antige specificite called **monoclonal antibody** (mAb) (see Figure 4.2 B). The antibodies produced by the different hybridomas are screened to find the ones with highest affinity for the antigen. The hybridomas selected are cloned to produce identical antibodies with identical response to the antigen.

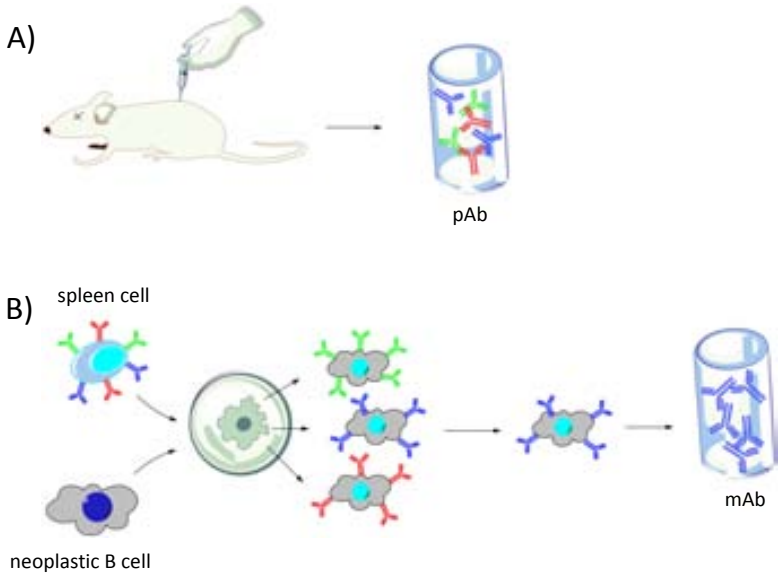

Figure 4.2: Scheme of the antibody production; A) polyclonal production and B) monoclonal production of antibodies.

The immunoassays are a powerful tool for the detection of proteins, which are based on the recognition of an antigen by its antibody. Current immunoassay tests consist in labeled techniques, depending on the label incorporated, they are distinguished between enzymatic immunoassays (ELISA), radioimmunoassays (RIA), chemiluminescent immunoassay (CL), and fluorescence immunoassay (FIA). Enzyme-linked immunosorbent assay (ELISA) employs a solid-phase enzyme immunoassay the detect the presence of an anlayte (usually an antigen), is the most used immunoassay as diagnostic tool. To detect and quantify the presence of the antigen in the sample, the antigen and/or the antibody must be targeted with enzyme. After the recognition process a substance containing the enzyme substrate is added. The reaction between the enzyme and the substrate produces a detectable signal, most commonly a color change in the substrate.

The detection strategy is another criterion in to classify the immunoassay tests which are divided into competitive and noncompetitive. The **competi-**

tive immunoassays determine the free binding sites by employing a limited concentration of antibodies or antigens. Using this type of assay, both of them can be immobilized on the solid surface.

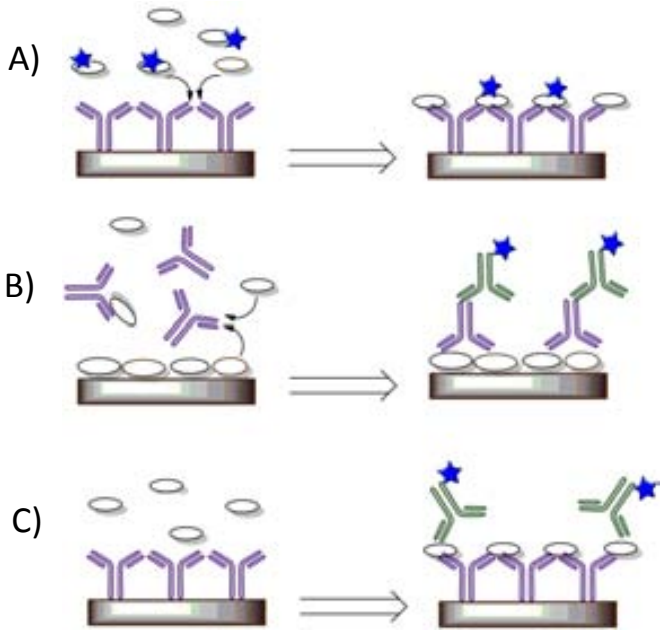

Figure 4.3: Types of immunoassays according with the detection strategy: A) direct competitive immunoassay, B) indirect competitive immunoassay, and C) a sandwich immunoassay.

The assays in which the antibody is immobilized on the surface are considered direct immunoassays (see Figure 4.3 A) due to the analyte from the sample and the labeled antigens are competing for the binding sites at the antibodies. After removing the non-reacted antigen and antibody, the label-antigen are determined according with the type of incorporated label. The obtained signal is inversely proportional to the analyte concentration.

In the indirect competitive strategy the antigens are immobilized on the solid surface and the analyte to determine is added together with the antibody (see Figure 4.3 B). In this case the immobilized antigens are competing with the

analytes from the sample for the antibodies. The antibodies on the surface are determined by the addition of a labeled antibody able to recognize the reacted antibody. The signal obtained in this case is also inversely proportional to the analyte concentration.

The **noncompetitive immunoassay** uses an excess of antibody concentration to measure the binding sites occupied by the analyte (see Figure 4.3 C). In this case, the antibodies are immobilized on the substrate and the analyte is added. In order to determine the analytes that are interacted with the antibodies on the surface, a labeled antibody that reacts with other epitope at the analyte is introduced, resulting in a sandwich immunoassay. The signal obtained is proportional to the analyte concentration. To perform this assay, it is needed that the analyte has more that one binding site.

However, labels are not required in photonic biosensors based on evanescent wave detection due to enable the label-free immunoassay which greatly simplifies the strategy. In this case, the types of immunoassays can be divided into direct, competitive, and sandwich immunoassay.

In a **direct immunoassay** (Figure 4.4 A), antibodies are immobilized on the transducer surface and the antigens are directly detected. The main features of this assay are short analysis times and less quantity of consumed reagent, together with the reduction of the assay complexity. The main drawback is the structural instability of antibodies to harsh conditions (acid or base solutions) employed to interrupt the antibody-antigen interaction.

In a **competitive immunoassay** (Figure 4.4 B), the protein to detect is used as receptor layer. The detection of the analyte is performed indirectly by incubating the variable antigen concentration with a determined quantity of antibody. The remaining free antibody of the solution will interact with the bioreceptor layer. The competitive immunoassay has important advantages in terms of device reusability, allowing many measurements for the same bioreceptor layer. This is due to the superior stability of the antigens in presence of acids or other harsh conditions that makes them more suitable as biological receptors than antibodies. The main disadvantage of this method is the increase in the assay time due to the previous incubation of the antibody with the protein to detect.

The **sandwich immunoassay** (Figure 4.4 C) is less employed in label-free

biosensors, however, it can be useful to amplify the signal when the direct immunoassay does not reach the desired sensitivity.

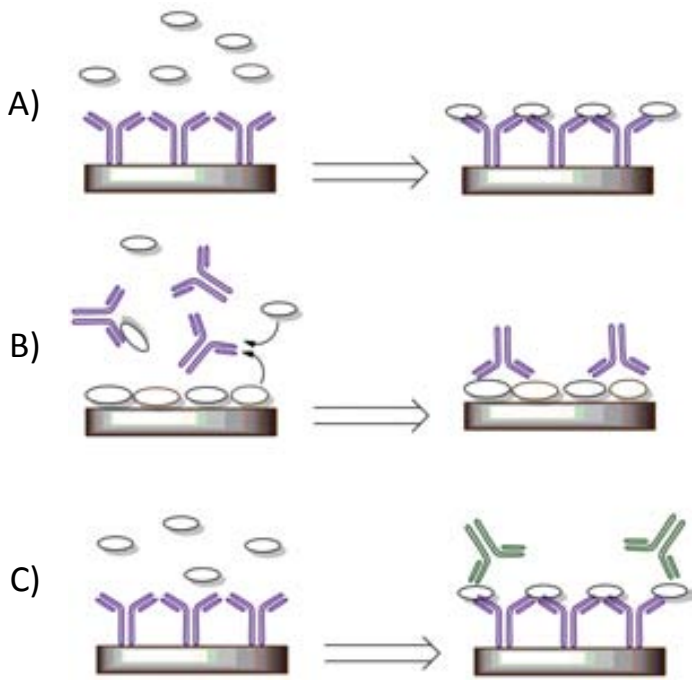

Figure 4.4: Types of immunoassay strategies in a label-free biosensor; A) direct, B) competitive, and C) sandwich immunoassay.

4.1.2 Regeneration of the sensor surface

To reuse the sensor chip surface the analyte must be removed, but the bioligand must stay intact. This so-called regeneration procedure (see Table 5.7) has to be evaluated empirically because the combination of physical forces responsible for the binding are often unknown, and the regeneration conditions must not cause irreversible damage to the bioreceptor.

Among the regeneration methods, the injection of low pH-buffers such as 10 mM Glycine pH 1.5 - 2.5, or 100 mM HCl is one of the most employed. The working mechanism is probably due to most proteins become partly unfolded and positively charged at low pH. The protein binding sites will repel each other and the unfolding will bring the molecules further apart.

Table 4.1: More employed regeneration solutions.

Acidic	HCl pH 1-3 glycine/HCl pH 1.5-3 formic acid pH 2-3 phosphoric acid pH 1.5 - 2.5
Basics	NaOH pH 11-13 glycine/NaOH pH 9-10 ethanolamine pH 8.5-10.5
Ionic	NaCl 0.5 - 5 M $MgCl_2$ 1-4 M

Other procedures use high pH, high salt content or specific chemicals to break the interaction. It is important to choose the mildest regeneration conditions that completely dissociate the complex.

4.1.3 Biosensor terminology

The terminology used at the biosensor field which is employed to compare the performance of a biosensor, as described in the following:

Dynamic range describes the range of analyte that is detectable by the sensor, or the minimum and maximum values that generate a response in the sensor. In a static configuration, the relationship between the sensor output signal and the analyte is $S = a + bs$, where S is the signal produced with s measurand, a is the intercept or the output signal at zero input signal, and b is the slope or **sensitivity** of the transducer. However, this relationship assumes that the response of the sensor is perfectly linear, which is not always the case.

In immunoassays, the hyperbolic or sigmoidal response of the signal in function of the concentration is usually employed. For that, different concentrations of the analyte are measured, the signal obtained by them must range from negligible to the maximum (saturated signal). To obtain the detection limits and the lineal range of the assay for a sigmoidal response of the sensor, the averaged

responses of the replicas measured for each concentration are plotted versus the logarithm of the analyte and fitted to a four-parameter logistic equation:

$$y = \frac{D + (A - D)}{1 + (\frac{x}{C})^B}$$

where x is the concentration, y is the response, A is the asymptotic maximum, corresponding to the signal in absence of analyte, B is the slope at the inflection point, C is the inflection point, equivalent to the half inhibitory concentration I_{50}, and D is the asymptotic minimum, corresponding to the background signal.

The **limit of detection** of the device will be found by calculating the analyte concentration that gives a 90% of the signal. The **lineal range** of the device is obtained from concentration given a signal from I_{80} to I_{20}.

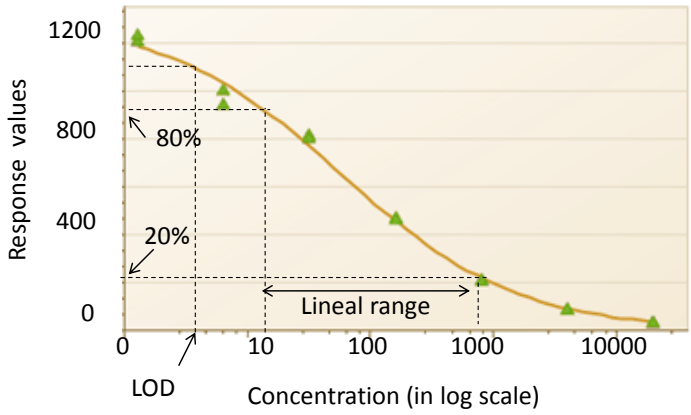

Figure 4.5: Four parameter logistic sigmoidal analysis.

Related parameters include saturation, selectivity, sensitivity, the concentration of analyte for which is obtained the zero output or the drift. Saturation is the point at which there is no further signal increase, even if more analyte is added to the sensor.

Selectivity describes the suppression of the detection of unspecific molecules or environmental interference. The warm-up time and frequency response describe how fast a sensor can respond to a analyte. Finally, the **repeatability/reproducibility** of the sensor describes how the response of the sensor changes if the same measurement is done under the same conditions.

4.2 Detection of the human Growth Hormone (hGH)

4.2.1 Introduction

Hormones are liberated by cells or glands to send out messages that affect cells in other parts of the organism. Only a small amount of hormone is required to alter cell metabolism. Hormones are secreted directly to the bloodstream by different glands which compose the endocrine system. Amongst these glands, the one that controls physiological processes as growth, reproduction, or metabolism is the pituitary gland. The human Growth Hormone (hGH) is a polypeptide hormone essential for normal growth and development, secreted by the anterior pituitary gland in higher quantities that any other pituitary hormone. Although its production by the anterior pituitary gland is controlled by the hypothalamus, it is altered by other factors such as exercise, sleep, and the stress [2]. hGH is secreted in a pulsatile manner as a result of alterations in the hypothalamic GH-releasing hormone (GHRH), which stimulates hGH synthesis and release, and somatostain, which inhibits GH release. In humans, up to eight to ten pulses of hGH are secreted in a 24 h period [3]. The most evident effect of the hGH in the body is the growth in height from the infancy due to the direct stimulation of the hGH in bones and in a huge variety of tissues.

Circulating hGH consists of a heterogeneous mixture of proteins, involving a predominant 22 kDa hGH isoform, and other less abundant variants such as the 20 kDa hGH, generated from alternative splicing of the primary transcript of full-length 22-kDa hGH [4]. The variation of the normal concentration of hGH in the bloodstream can be an early indicator of an anomalous growth pointing out an altered biological state. The excess of hGH, commonly caused by pituitary tumours which result in a gradual increase of hGH production, leads to an illness named acromegaly or pituitary gigantism when it occurs in childhood [5]. The hGH deficiency prevents a normal growth, a problem particularly serious during the infancy. The main causes for hGH deficiency are genetic or due to

pituitary malformations [6].

At the moment, the detection methods used for quantitative determination to hGH include bioassays, radioreceptor assays, and immunoassays. The classical in vivo bioassays for hGH evaluate rat tibial growth, rat weight, or gain. However, they are limited because of their relative insensitive, slow performance, imprecision, and cost. Radioreceptor assays were early employed in the detection of hGH but have not found wide application for routine purposes. They are also relatively insensitive and require tissue culture facilities or preparation of plasma membrane fractions. Moreover, they are very prone to interfere when used with unextracted serum. Immunoassays are the common technique for the detection of immunological epitopes on hGH molecules due to the possibility of obtaining high affinity antibodies. The most frequent immunoassay is the enzyme-linked immunosorbent assay (ELISA) but radioimmunoassays (RIA), immunoradiometric assays (IRMA), and immunofunctional assays (IFA) are also employed for hGH determination due to their sensitivity and high sample throughput [7]. However, these conventional selective assays are time consuming; require florescent labels, or radioactive probes. In addition, most of these assays require facilities, which obstruct their application in settings out of the lab. The lowest limit of sensitivity for existing hGH immunoassay is 50 pg/ml, obtained by a sandwich-type chemiluminescence assay [8].

A label-free detection scheme has been employed for our group by using a home-made SPR device for the real-time detection of hGH [9]. The results showed high reproducibility and performance but the LOD achieved (6 ng/ml) is not adequate to detect hGH basal concentrations. The higher sensitivity of interferometric devices has encouraged us to investigate the applicability of the BiMW device for the detection of hGH. Therefore, the aim of this study is to perform a real-time and label-free biosensing of hGH but achieving a LOD around the pg/ml. For that, a competitive immunoassay has been employed in which hGH has been covalently immobilized on the sensor surface by the use of CTES silane. The high stability of the hGH enables a complete regeneration of the biosensor after each detection. Thus, multiple interactions are allowed using the same bioreceptor layer making possible an evaluation of the reproducibility, linear range, and LOD of the biosensor for the hGH detection.

4.2.2 Materials and Methods

Reactives. EDC (99%), NHS (98%), ethanolamine, and components of phosphate buffer saline (PBS; 10 mM phosphate, 2.9 mM KCl, 137 mM NaCl, pH = 7.4) were purchased from Sigma-Aldrich, Germany. Hydrochloric acid (HCl, 35-38%) was purchased from Poch SA, Poland. Recombinant human Growth Hormone (hGH) composed exclusively of the 22 kDa isoform was purchased from Harbor-Ucka Medical Center, USA. Acetic acid for the acetate buffer (Ac; 10 mM acetate, pH 5) was purchased from Panreac, Spain. The monoclonal antibody (mAb hGH), that recognizes all hGH isoforms, was obtained from and characterized by the Department of Immunology and Oncology from the National Center of Biotechnology, CSIC. The mAb hGH was produced from immunized mice with hGH. The highest titer of the serum with the antigen determined the mice selected for cellular fusion experiments to immortalize the cells that will produce the antibody. The cells coming from the lymphatic glands from the selected mice were fused with the myeloma P3X63-Ag8.653 using PEG by previously described protocols [10]. The presence of the specific antibody in these cultures was analyzed by enzymatic immunoassay (EIA), the positive ones were cloned by limiting dilution of the hybridoma. The monoclonal antibodies obtained were purified by ammonium sulfate precipitation from the ascitic liquid. Affinity and specificity of the mAb hGH were determined by radioimmunoassay (RIA) and EIA, obtaining an affinity of 3 nM for both hGH isoforms, 20 and 22 KDa. The mAb hGH was additionally purified by a HiTrap^{TM} NHS-activated HP Column from GE Healthcare, USA, prepared with recombinant hGH. The preparation of the column and the coupling of the antigen were carried out following the manufacturer's instructions. After that, the mAb hGH was introduced in the column at a concentration of 4 mg/ml, obtaining 2.7 ml of the purified antibody. This antibody solution was dialyzed by a PD-10 Desalting Column from GE Healthcare, the resulting purified antibody was obtained at a concentration of 395 μg/ml. Purified antibody (mAb hGH) was aliquoted and stored at -20°C until its use.

Biofunctionalization procedure. Silanization of the Si_3N_4 sensor area surface using CTES silane was performed as explained previously. After that, the chip is placed in the setup and from now on all the processes are done in-situ by using the fluidic cell. Activation of the carboxyl groups on the sensor area surface is carried out by flowing the EDC/NHS solution. Immediately afterward, hGH 50 μg/ml in acetate buffer 10 mM (pH = 5) is flowed over the activated surface. The antibody concentration and the pH of the immobilization buffer

were previously optimized to obtain the maximum antibody detection signal. To wash out nonreacted proteins, 0.05 M of HCl was used and the hGH injection was repeated. Finally, ethanolamine (1M, pH = 8) is injected to react with the remaining activated carboxylic groups. The volume of all the injections is 250 μl and the water flow is maintained at a constant rate of 20 μl/min. Water is replaced by PBS at the end of the biofunctionalization process. A draft of the biofunctionalization process can be seen in Figure 4.6 A.

Experimental BiMW immunoassay format: competitive assay. The detection of hGH is carried out by a competitive immunoassay. In this format, the hGH is immobilized on the sensor surface and a constant amount of antibody is added to all the samples. Further antibody binding to the immobilized antigen is inhibited by the presence of the analyte thus producing decreasing signals as the analyte concentration increases. The election of the competitive format versus the direct one is mainly motivated by the possibility of employing the hormone as bioreceptor instead of the antibody. It entails several advantages such as the prevention of the problems derived by the random orientation of antibodies when are immobilized on the sensor area surface. Furthermore, the stability of the antigens front harsh environments is higher than the antibodies which enables the use of acidic or basic solutions without damaging the sensor area interface. For that, the competitive immunoassay format extends the immunosensor lifespan due to the possibility of regenerating the bioreceptor surface. Therefore, the competitive immunoassay format assures the best performance, reusability, and stability of the immunosensor maintaining its activity intact throughout a long number of measures and regeneration cycles.

The detection of the analyte in this biosensor is performed by a competitive immunoassay as represented in Figure 4.6 B. For calibration curves, a set of triplicate hGH standard concentrations ranging from 10 pg/ml to 100 μg/ml in PBS and blank controls are mixed (1:1) with mAb hGH in PBS. Then, solutions are injected sequentially over the hGH sensor surface at 30 μl/min and the interferometric signal is monitored in real-time. Calibration curve for hGH detection is carried out using a fixed concentration of mAb hGH of 1 μg/ml in PBS. Reutilization of the sensor surface is accomplished by an injection of HCl 20 mM regeneration solution at a flow speed of 40 μl/min.

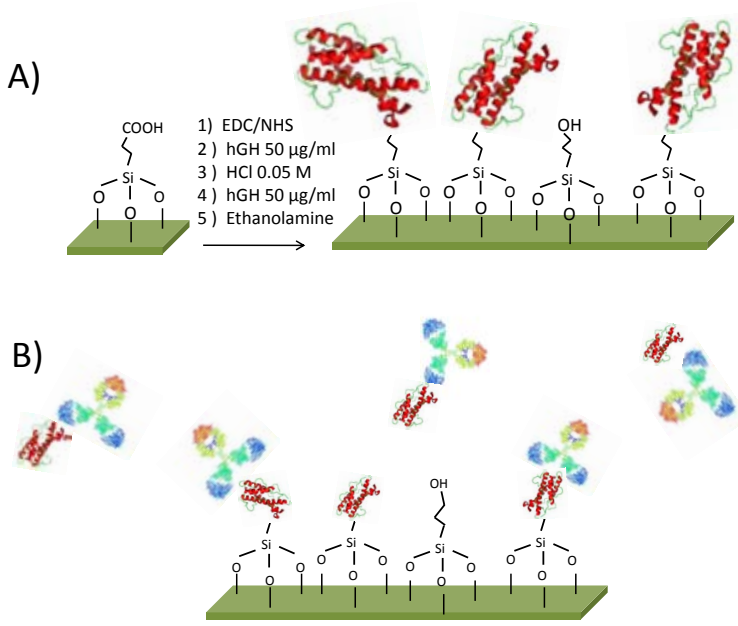

Figure 4.6: Draft of hGH detection procedure by a competitive immunoassay. A) Result of the biofunctionalization process and B) scheme of the competitive assay used.

4.2.3 Results

The experimental system designed for the biosensing with the BiMW device allows for the in-situ biofunctionalization of the sensor area by the use of the fluidic cell after the ex-situ chip silanization. This enables the monitoring in real-time of the processes occurring on the sensor surface. The measurements for the complete biofunctionalization procedure are shown in Figure 4.7. The interferometric signals for the different steps are presented as follow: A) activation of the carboxyl groups present in the silanized surface by the EDC/NHS solution, B) covalent attachment of the hGH protein to the activated carboxylic groups by the creation of a peptidic bond, C) 0.05 M of HCl to clean adsorbed proteins, D) second injection of hGH, E) reaction of ethanolamine with the remaining activated groups, and F) change from water flow (used to perform

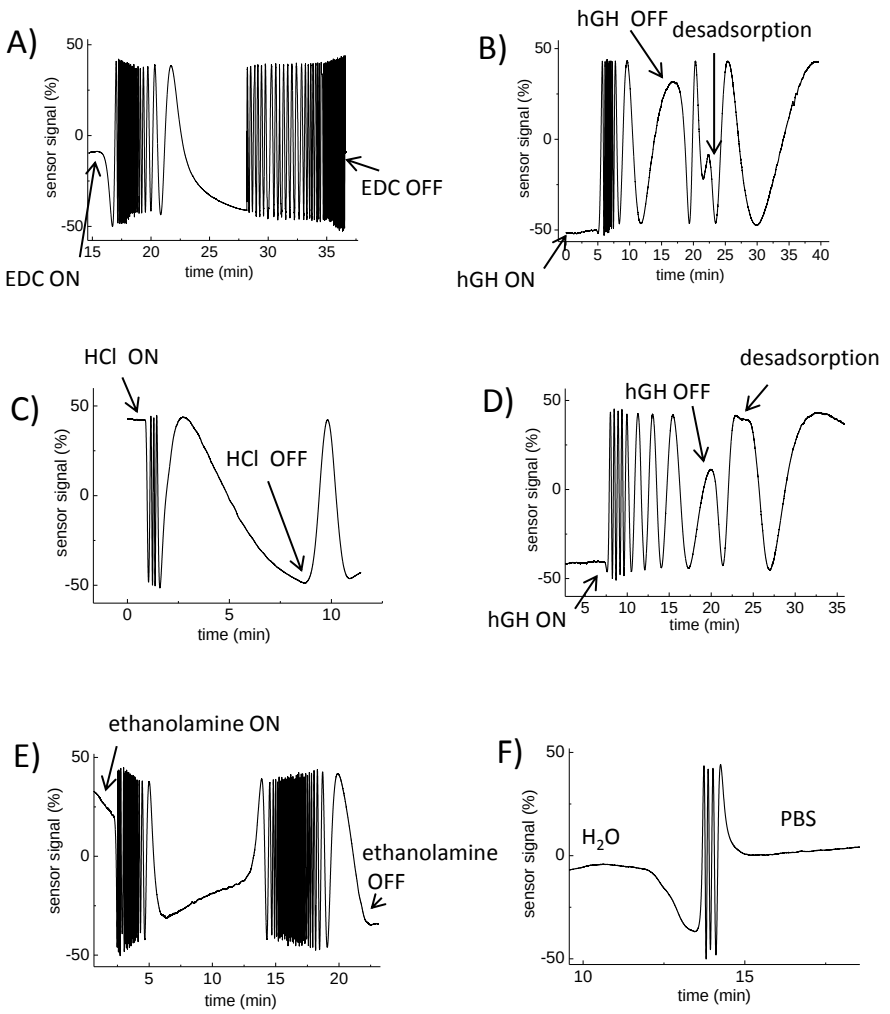

Figure 4.7: Real-time monitoring of the in-situ complete biofunctionalization procedure maintaining water in flow. A) EDC/NHS, B) hGH 50 μg/ml, C) HCl 0.05M, D) hGH 50 μg/ml, E) ethanolamine, and F) change from water to PBS in flow.

the in-situ biofunctionalization) to PBS flow (more adequate for the biodetections).

The interferometric analysis of the biofunctionalization is very useful to investigate the formation of the biological layer, especially those related with the covalent attachment of the biomolecule. This process will determine the reproducibility, sensitivity, and selectivity of the detection. The resulting $\Delta\Phi$ for the covalent attachment of hGH to the surface (Figures 4.7 B and D) can give us an idea about the covering of the surface and consequently about the recognition process with the antibody. Quantified values for the covalent attachment of hGH on the transducer surface are shown in Table 4.2. The net change of $\Delta\Phi$ is higher for the first injection of hGH ($8.5\times2\pi$ rad), as could be expected. However, the $\Delta\Phi$ obtained for the second injection ($6.4\times2\pi$ rad) indicates that this additional step is necessary for a successful biofunctionalization procedure. In the optimization of this two-step biofunctionalization procedure it was evidenced that a third hGH injection was unnecessary.

Receptor injection	$\Delta\Phi$ Entrance	$\Delta\Phi$ Exit	$\Delta\Phi$ Desorption	Net Change $\Delta\Phi$
1^{st}	11.44	1.29	1.65	$8.5\times2\pi$ rad
2^{nd}	8.33	0.83	1.1	$6.4\times2\pi$ rad

Table 4.2: Values of the obtained for the covalent attachment of hGH on the sensor surface.

The selectivity and specificity of the bioreceptor layer created by this biofunctionalization process is showed in Figure 4.8. The specific detection of mAb hGH 0.5 μg/ml (3 nM) by the hGH biolayer with a signal of $\Delta\Phi = 0.46\times2\pi$ rad is presented in comparison with the same concentration of mAb BSA used as control. The negligible response of nonspecific antibodies confirms the selectivity of the monolayer. It also demonstrates the complete covering of the surface by the hGH, avoiding nonspecific interaction between the unspecific mAb BSA and the transducer surface. The recovery of the baseline after flowing a diluted HCl solution indicates the loss of the antibodies due to the disruption of the biological recognition process between the hGH and the mAb hGH recovering the initial conditions. The high stability of both the protein and the covalent bond that links it with the Si_3N_4 surface allows the regeneration of the biosensor. In these conditions, we are able to perform more than 50 different biodetections in each channel of the device reducing cost and time and allowing a complete study of the biointeraction.

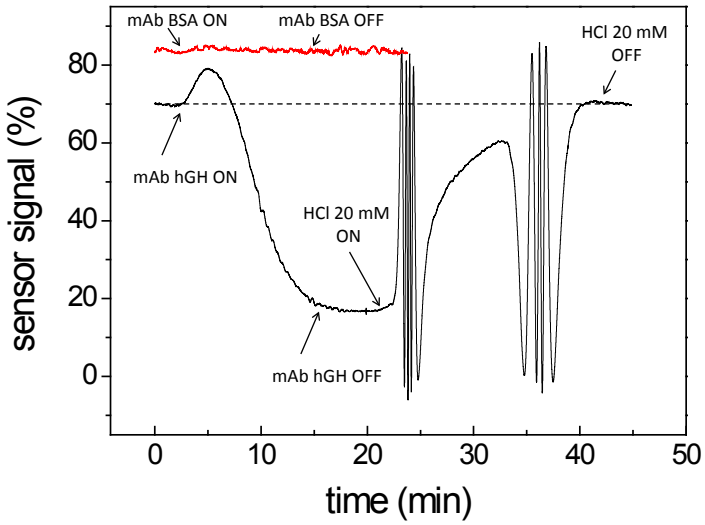

Figure 4.8: Real-time monitoring of the detection of 0.5 μg/ml of mAb hGH ($= 0.46 \times 2\ \pi$ rad) and the regeneration of the surface. A total regeneration of the surface is obtained as can be noted by the recovering of the baseline.

The hGH receptor layer response is evaluated before performing the competitive assay by the interaction with different concentrations of mAb hGH ranging from 0.25 to 5 μg/ml followed by regeneration of the surface. The $\Delta\Phi$ obtained for each mAb hGH concentration is shown in Figure 4.9 and individual measurements are represented in the inset. This information will be useful to choose the fixed concentration of antibody to perform the competitive assay. The antibody concentration chosen must not saturate the bioreceptor layer because in such a case small quantities of hormone will not be detectable. On the other hand, interferometric signal given by the concentration chosen must be high enough to obtain a wide lineal range. The fixed antibody concentration chosen will determine the detection limit and the lineal range obtained for the detection. Lower detection limits will be obtained by lower fixed concentrations, however it will entail an undesired reduction in the range of the response.

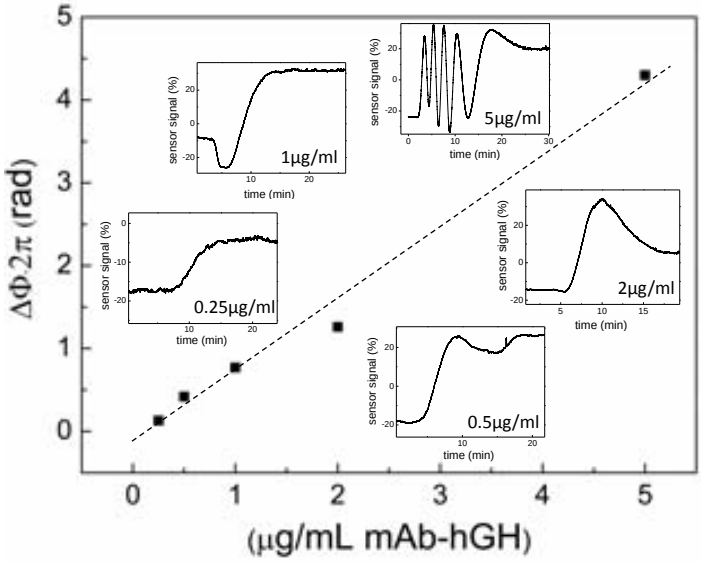

Figure 4.9: Response of the hGH surface to different concentrations of mAb hGH.

Following these considerations, the fixed mAb hGH concentration used to carry out the competitive assay has been 1 μg/ml. To perform the calibration curve for the detection of hGH, a volume of the mAb hGH is incubated for 5 min with the same volume of the hGH concentration. After that, 250 μl solution is injected in the system and the analysis is done in less than 8 minutes (flow velocity of 30 μl/min) as shown in Figure 4.10 A. Including the incubation of the antibody with the hGH, the total time of the assay is 13 min. The standard calibration curve of hGH can be shown in Figure 4.10 in where each point is the mean value of the three replicated measurements. Mean points has been adjusted to a sigmoidal curve in where LOC is calculated as 8 pg/ml, the I_{50} is 35 ng/ml, and the lineal range goes from 668 pg/ml to 4 μg/ml. In the Table 4.3, the results obtained are compared with those obtained for the SPR analysis [9].

In conclusion, LOD obtained by the BiMW biosensor for the hGH has been improved in an order of magnitude with regard to the previously discussed methods. In comparison with the SPR immunoassayassay, LOD has been decreased 1000 times. The wider linear range of the BiMW in comparison with the SPR analysis can be related to the increase in the size of the sensor area. It can be observed a high dispersion of the triplicate measurements, meanly in the low-

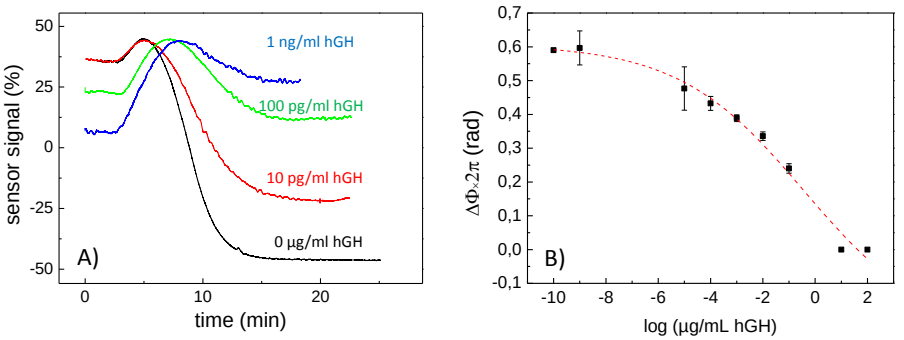

Figure 4.10: A) Real-time measurements of different concentration of hGH detection using a competitive assay and B) standard calibration curve of hGH in PBS. Each point shows the mean value of the three replicate measurements.

Device	I_{50}	Lineal range	LOD
SPR	91 ng/ml	18-542 ng/ml	4 ng/ml
BiMW	35 ng/ml	680 pg/ml - 4 μg/ml	8 pg/ml

Table 4.3: Values obtained for the hGH detection by SPR analysis in comparison with values obtained by the BiMW device.

est concentrations of hGH. This variability can be due to the variations in the room temperature that causes condensation in the container where the sample is stored. Another factor is the adsorption of the biomolecules onto the walls of the vessel when it is diluted. Reproducibility of the measurements for the hGH calibration curve should be improved by the control of these parameters. Nevertheless, the excellent LOD and linear range obtained with the short analysis time, means a significant improvement of the hGH detection in comparison with standard techniques.

4.3 Detection of the bacterium Pseudomona aureginosa

4.3.1 Introduction

There is no doubt that detection of harmful microorganisms at the early stages of the infection in a direct and effective way is the best manner to avoid the contagious. From this point of view, prompt detection of pathogen microorganisms is actually an unmet requirement. The standard protocol for the detection of pathogenic microorganisms includes the isolation, growth, and biochemical test (immunologics, DNA amplification) to complete the identification. Culture assay for bacteria detection has the highest sensitivity, it is possible to detect just one bacterium by the formation of a colony in the selective agar. Afterwards, the bacteria must be further identified by immunological methods. However, the complexity and long time of analysis make this method unpractical for routine tests in greenhouses, warehouses, or slaughterhouses.

There is an urgent need for improving velocity of detection methods of bacteria while maintaining the high sensibility of the current analytics tests. The emerging label-free techniques based on photonic devices could satisfy this demand by achieving the same LOD as current culture-based methods but drastically diminishing the analysis times.

There are an extended number of reported articles for real-time and label-free bacteria detection using an SPR device [11]. Detection of Salmonella Typhimurium using an SPR biosensor has been achieved at 1×10^6 cfu/ml [12]. Four different species of bacteria, Escherichia coli O157:H7, Salmonella choleraesuis, Listeria moncytogenes, and Campylobacter jejuni have been detected in different mediums obtaining detection limits ranging from 3.4×10^3 to 1.2×10^5 cfu/ml [13]. Even though in some cases these detection limits have been slightly improved (100 cfu/ml) [14] the common detection limits for bacteria detection using an SPR device are up to 1000 cfu/ml. Factors that are believed to attribute to the limited sensitivity of direct cell-capture in SPR assays are the effective penetration depth of the evanescent field. This means that only refractive index changes occurring within the evanescent field will cause a change in the generated SPR signal. Furthermore, these instruments average the SPR angle over an area of approximately 0.25 mm^2 on the sensor surface. Thus, the signal response can decrease as bacterial cells are large and may not an area

measured [15].

Since the natural pathogenic contaminants in most environments rarely exceed 10^3 cfu/ml or g matrix (e.g., Listeria monocytogenes in food) [16], the exposed real-time techniques could not provide the adequate LOD in this application. However, interferometric transducers could make them appropriate candidates for rapid and highly sensitive detection of bacteria due to its higher sensitivity. However, few works about interferometric microorganism detection are available and the LOD of the existing ones do not improve the SPR performance.

The capabilities of a BiMW device for the detection of Pseudomonas aeruginosa by a direct immunoassay are investigated in the following experiment. Pseudomonas aeruginosa is a common bacterium that can be found in soil, water, skin flora, and most environments throughout the work. The versatility of this bacterium enables to infect damaged tissues or those with reduced immunity. If such colonization occur in critical body organs, shuch as the lungs, the urinary tract, and kidneys, the results can be fatal. This bacterium is frequently found in medical equipment causing infections in hospitals and clinics. Due to the risk of infection associated to handle life bacteria, they must be previously deactivated. As a consequence of the different steps involve in the deactivation, some bacteria could broke. For the assembly of this biosensor, polyclonal antibodies are employed. These antibodies have different affinities by several membrane proteins, thus, the evaluation of the selectivity of the biosensor must be done by the detection of another bacterium, the Staphylococcus aureus which is used as control.

4.3.2 Materials and Methods

Reactives. EDC (99%), NHS (98%), ethanolamine, and components of phosphate buffer saline (PBS; 10 mM phosphate, 2.9 mM KCl, 137 mM NaCl, pH = 7.4) were purchased from Sigma-Aldrich, Germany. Polyclonal antibody against Pseudomonas aeruginosa (pAb-Pseudomonas) was purchased in a concentration of 4.5 mg/ml from Abcam, UKA. Pseudomonas aeruginosa and Staphylococcus aureus were obtained from the group of Applied Microbiology from the UAB, Barcelona. Deactivation of bacteria was carried out by a combined treatment of ultrasound for 3 min followed by 30 min of heat. The experiments carried out by the group of Applied Microbiology indicated that ultrasounds treatment breaks the bacterial cell that is implied in the release of antigen, enhancing the detection limits of the ELISA assays. However, some of the bacteria retain their

integrity and they can be observed in the microscope images that are shown in Figure 4.11, in where a drop of a Pseudomonas solution (1×10^{-7} colonies for unit, CFU) was placed on a glass slide.

Biofunctionalization procedure. Silanization of the Si_3N_4 sensor area surface using CTES silane was done as explained previously. After that, the chip is placed in the setup and the vast of the experiments are done in-situ. Activation of the carboxyl groups on the sensor area surface is carried out by flowing the EDC/NHS solution. Immediately afterward, 25 μg/ml of pAb-Pseudomonas are flowed over the surface of the sensor area. Finally, ethanolamine solution (1 M, pH = 8) is used to react with the remaining activated carboxyl groups. The volume of all the injections is 250 μl at a constant rate of 20 μl/min, maintaining water at flow. Water is replaced by PBS at the end of the biofunctionalization process. A draft for the biofunctionalization of the transducer surface with antibodies is shown in Figure 4.12 A.

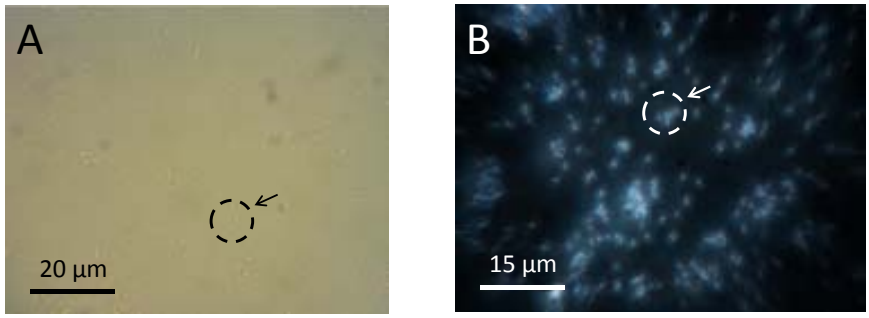

Figure 4.11: Microscope images of Pseudomonas bacteria. A) Optical microscope image using 40× magnification and B) dark field microscope image using 60× magnification.

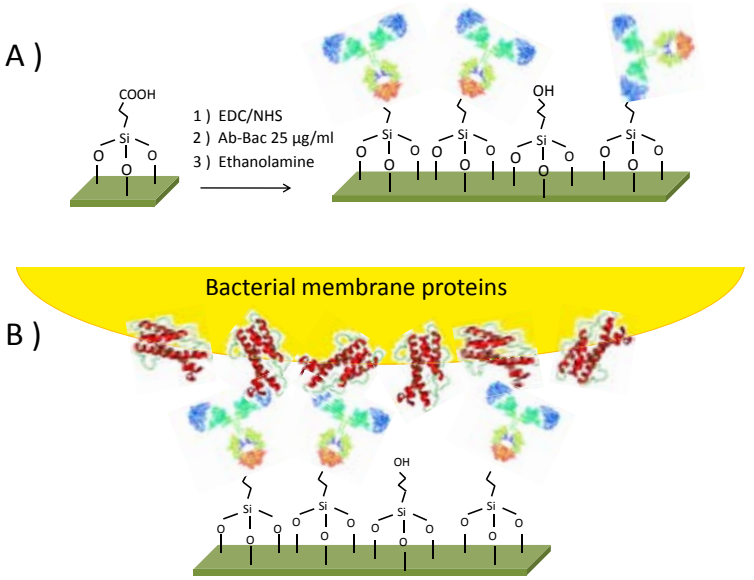

Figure 4.12: Draft of Pseudomonas detection procedure by a direct immunoassay. A) Result of the biofunctionalization process and B) scheme of the direct assay.

Experimental procedure: direct assay. A direct assay has been designed for the immunodetection of Pseudomonas. In a direct assay, antibodies are immobilized on the transducer surface and the antigen is directly detected, as illustrated in Figure 4.12 B, reducing the analysis time, the consumed reagent, and the complexity in comparison with competitive assay. Taking into account the structural instability of antibodies front regeneration solutions, we perform an additive assay by adding increasing concentrations of suspended bacteria in PBS. The concentrations of the detected bacteria suspensions are 10, 1000, 1×10^5 and 1×10^7 cfu/ml. The PBS flow is maintained at a constant rate of 20 μl/min during all the experiment. Two channels biofunctionalized with pAb-Pseudomonas from the same chip are used in this experiment, in the first one specific Pseudomonas detection is carried out. In the second one unspecific detection of Staphylococcus is performed as control.

4.3.3 Results

In this experiment, amino groups from the pAb-Pseudomonas protein structure were attached onto the EDC-activated sensor surface in a non-oriented way. Polyclonal antibodies are been chosen due to offer affinity for more than one protein of the pseudomona cellular membrane and then, provide a wider response. However, the presence of common proteins in different bacterial outer membranes could be an inconvenience for the use of polyclonal antibodies due to the cross-reactivity with unspecific bacteria. The real-time interferometric signals for the corresponding immobilization of the antibodies on the silanized sensor surface are shown in Figure 4.13.

As explained previously, the interferometric analysis of the in-situ biofunctionalization of the surface area can give us valuable information about the quantity of biological receptor immobilized. In this biofunctionalization process, the net $\Delta\Phi$ obtained for both channels is very similar, assuring the possibility of comparing the responses, as it can be seen in Table 4.4. Desorption signals indicate that the antibody concentration used to perform the assay, 25 μg/ml, is an adequate quantity. The use of the bioreceptors in excess is requited to assure the total covering of the sensor area. However, high excess could arise in an unnecessary increase in the cost of the analysis and formation of multilayers.

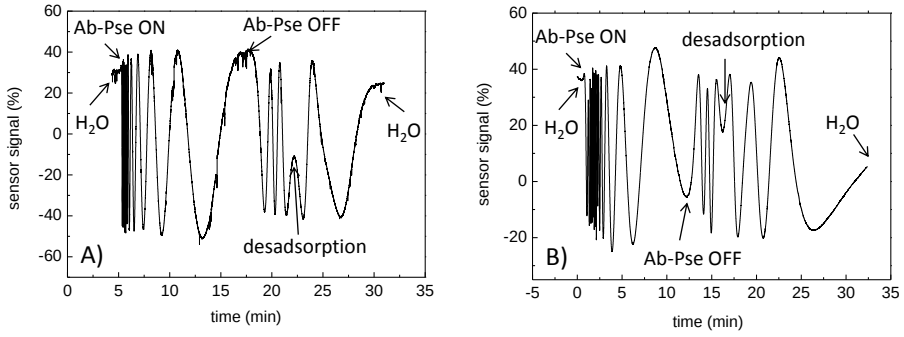

Figure 4.13: Real-time monitoring of the covalent attachment of pAb-Pseudomonas in PBS onto the EDC-activated BiMW sensor area maintaining water in flow in A) channel 1 and B) channel 2.

Channel	Entrance	Exit	Desorption	Net Change $\Delta\Phi$
channel 1	11.5	2.57	1.5	$7.4\times2\pi$ rad
channel 2	12.4	2.5	2.8	$7.1\times2\pi$ rad

Table 4.4: Values of the obtained for the covalent attachment of the pAb-Pseudomonas on the sensor surface.

After that, an additive assay was performed by flowing increasing bacteria concentrations. Results for the detection of Pseudomonas using the additive immunoassay are showed in Figure 4.14. In the inset, the individual interferometric signals for each bacteria concentration are shown. As it can be noted, good signals are obtained even for the lowest concentration tried, 10 cfu/ml. The results achieved clearly indicate that the signal obtained cannot be given by entire bacteria. Considering that just 250 μl are injected from a milliliter that contains a total of 10 bacteria, the total volume of the channel is 15 μl, and the typical volume of a bacteria is 1 nl, the possibilities of capturing a bacteria by the sensor area are very scarce. Thus, the detection must be given by the interaction of the antigen contained in the bacteria, liberated due to the inactivation process. This antigen is homogeneously dispersed in the PBS solution, enhancing the signal. As it has been witnessed, the response of the biosensor for the different bacteria concentrations is highly sensitive, improving in 3 orders of magnitude the ELISA assays performed by the group of Applied Microbiology that supplied with the different types of deactivated bacteria. Moreover, the 250 μl of bacteria solution have flowed at a velocity of 20 μl/min, accounting for a time of analysis of 12 min.

To check the selectivity of the receptor layer and the degree of specificity of these signals, channel 2, which has also been biofunctionalized with pAb-Pseudomonas, is used to detect the Staphylococcus bacteria using the same protocol described before. Staphylococcus solutions in PBS are injected in this sensor area to perform an additive immunoassay at the same concentrations that for the Pseudomonas detection. Resulting $\Delta\Phi$ for each bacteria concentration is shown in Figure 4.15. In the inset, the individual interferometric signals for each bacteria concentration are shown. As expected, the response for the nonspecific bacteria is not totally negligible, this fact can be given to unspecific adsorption of the bacteria onto the antibody surface, and/or the possibility that due to the polyclonal response some pAb-Pseudomonas present affinity for proteins contained in both bacteria.

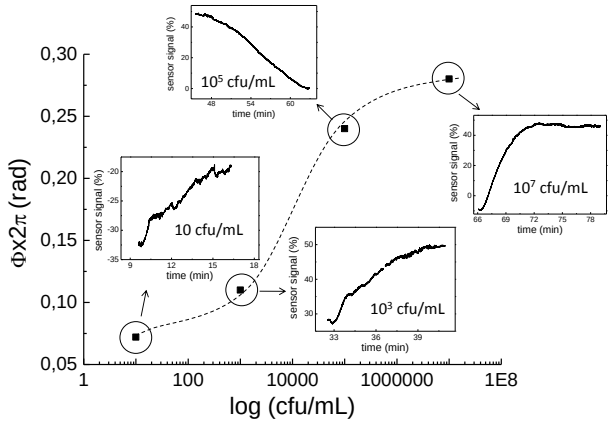

Figure 4.14: Response of pAb-Pseudomonas bacteria receptor layer to different concentrations of specific Pseudomonas bacteria. Inset: interferometric signal due to the detection of 10, 1000, 1×10^5, and 1×10^7 cfu/ml of Pseudomonas.

To quantify the cross-reactivity of the pAb-Pseudomonas and the specificity of the signal, both calibration curves can be represented in the same graph for a better comparison. In Figure 4.16, specific detection is represented by the black line with squares whereas nonspecific detection is represented by the red line with circles. High selectivity of the immunoassay can be noted due to significant interferometric responses that are only given by the specific bacteria. For a further analysis of the biolayer selectivity and the specificity of the method, the signal for the lowest concentrations of specific bacteria is compared with the signal for the same concentrations of nonspecific baterias. As can be seen in Figure 4.16 A, the specificity of the detection of 10 cfu/ml is 75% as the $\Delta\Phi$ caused by the detection of specific Pseudomonas is $0.04\times2\pi$ rad and the detection of nonspecific Staphylococcus used as control is $0.01\times2\pi$ rad. When increasing the concentration of bacteria to be detected, the specificity of the signal is also increased. As can be noted in Figure 4.16 B, when the bacteria concentration is raised to 1000 cfu/mL, the specificity of the signal is 88%.

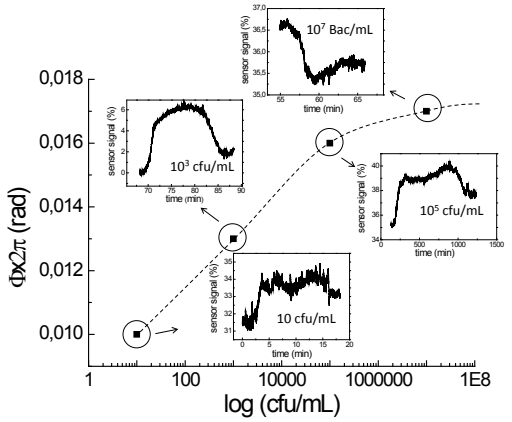

Figure 4.15: Response of pAb-Pseudomonas bacteria receptor layer to different concentrations of nonspecific Staphylococcus bacteria. Inset: interferometric signal due to the detection of 10, 1000, 1×10^5, and 1×10^7 cfu/ml of Staphylococcus.

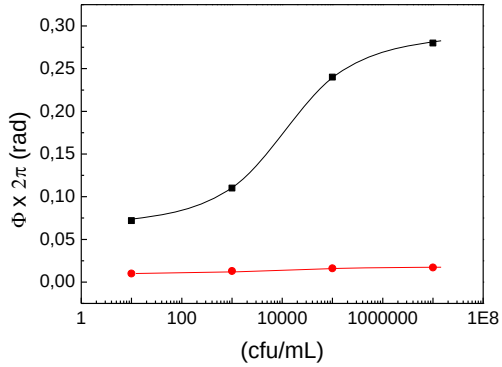

Figure 4.16: Comparison between specific Pseudomonas (squares, black line) and nonspecific Staphylococcus (circles, red line)

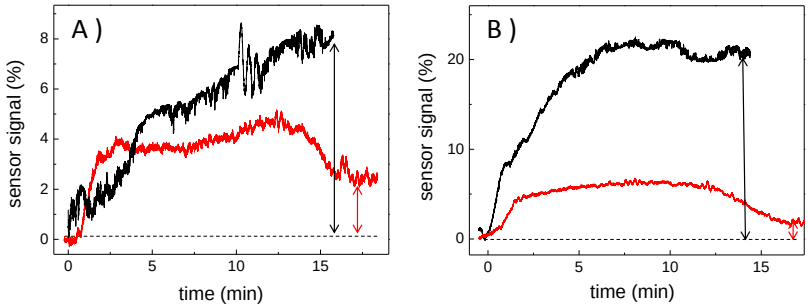

Figure 4.17: Real-time monitoring of specific Pseudomonas (black line) in comparison with unspecific Staphylococcus (red line). A) 10 cfu/mL and B) 1000 cfu/mL

4.4 Conclusions

The real-time and label-free detection of different types of proteins using a BiMW biosensor has been presented in this chapter. Firstly, we present the detection of hGH by a competitive immunoassay in which the reproducibility, stability, and selectivity of the immobilized bioreceptor layer has been demonstrated. LOD achieved for the competitive immunoassay have improved by 1000 times the LOD obtained for SPR and the practical lineal range has been dramatically increased. An improvement of the LOD and the reproducibility of the biomeasurements is expected in controlling some environmental conditions (i.e. room temperature, humidity). In comparison with the most sensitive reported technology to detect hGH (labeled), the LOD has been decreased in an order of magnitude and the total time of analysis has been reduced to 13 min. These results represent a significance improvement for the use of the detection of hGH as an early biomarker related with some harmful illness. Secondly, we present the preliminary results for the direct immunoassay for the specific bacterium Pseudomonas aeruginosa and the study of the cross-reactivity of the biosensor using the nonspecific bacterium Staphylococcus aureus. Polyclonal antibodies against Pseudomonas immobilized in a non-oriented way have been employed as bioreceptor layer. To avoid regeneration cocktails that could damage the antibodies, a simple additive assay has been used. The biosensor response for the specific bacteria has demonstrated detection limits close to current technologies used to detect harmful bacteria but drastically reducing the analysis time

from hours to a total of 12 min. Specificity of the signal studied by the cross-reactivity between Pseudomonas and Staphylococcus is higher than the 75%, even for the lowest concentration. However, the deactivation process is a drawback to deeply investigate the LOD of the device for entire bacteria. Due to the promising results obtained, our next step in this direction is to investigate the LOD of the BiMW device for whole harmless bacteria. In conclusion, the BiMW device conveniently biofunctionalized has demonstrated high performance and extremely sensitivity for the two proteomic applications investigated.

Bibliography

[1] Lee Hartwell, David Mankoff, Amanda Paulovich, Scott Ramsey, and Elizabeth Swisher. Cancer biomarkers: a systems approach. *Nat. Biotechnol.*, 24:905 908, 2006.

[2] Andrea Giustina and Johannes D. Veldhuis. Pathophysiology of the neuroregulation of growth hormone secretion in experimental animals and the human. *Endocrine Reviews*, 19(6):717 797, 1998.

[3] Madalina Ionescu and Lawrence A. Frohman. Pulsatile secretion of growth hormone (GH) persists during continuous stimulation by CJC-1295, a long-acting GH-releasing hormone analog. *J. Clin. Endocrinol. Metab.*, 91(12):4792 4797, 2006.

[4] Kin-Chuen Leung, Chris Howe, Lily Y.-Y. Gui, Graham Trout, Johannes D. Veldhuis, and Ken K. Y. Ho. Physiological and pharmacological regulation of 20-kda growth hormone. *Am J Physiol Endocrinol Metab*, 283:836 843, 2002.

[5] Roger Guillemin, Paul Brazeau, Peter Bohlen, Frederick Esch, Nicholas Ling, and William B. Wehrenberg. Growth hormone-releasing factor from a human pancreatic tumor that caused acromegaly. *Science*, 218(5):585 587, 1982.

[6] David M Hoffman, Anthony J O'Sullivan, Robert C Baxter, and Ken K Y Ho. Diagnosis of growth-hormone deficiency in adults. *The lancet*, 218(5):1064, 1994.

[7] Violeta Popii and Gerhard Baumann. Laboratory measurement of growth hormone. *Clinica Chimica Acta*, 350(1-2):1 16, 2004.

[8] Martin Bidlingmaier, Jennifer Suhr, Andrea Ernst, Zida Wu, Alexandra Keller, Christian J. Strasburger, and Andreas Bergmann. High-sensitivity chemiluminescence immunoassays for detection of growth hormone doping in sports. *Clin. Chem.*, 55(3):445 453, 2009.

[9] Juan Trevino, Ana Calle, Jose Miguel Rodr guez-Frade, Mario Mellado, and Laura M. Lechuga. Surface plasmon resonance immunoassay analysis of pituitary hormones in urine and serum samples. *Clin Chim Acta*, 403:56 62, 2009.

[10] E. Harlow and D. Lane. *Antibodies: a laboratory manual*. New York: Cold Spring Harbor Laboratory, 1988.

[11] Jir Homola. Surface plasmon resonance sensors for detection of chemical and biological species. *Chem. Rev.*, 108:462 493, 2008.

[12] Yu bin Lan, Shi zhou Wang, Yong huang Yin, W. Clint Hoffmann, and Xian zhe Zheng. Using a surface plasmon resonance biosensor for rapid detection of salmonella typhimurium in chicken carcass. *J. Bionic Eng.*, 5(3):239 246, 2008.

[13] Allen D. Taylor, Jon Ladd, Qiuming Yu, Shengfu Chen, Jir Homola, and Shaoyi Jiang. Quantitative and simultaneous detection of four foodborne bacterial pathogens with a multi-channel spr sensor. *Biosens. Bioelectron.*, 22:752 758, 2006.

[14] Byung-Keun Oh, Woochang Lee, Young-Kee Kim, Won Hong Lee, and Jeong-Woo Choi. Surface plasmon resonance immunosensor using self-assembled protein g for the detection of salmonella partyphi. *J. Biotech.*, 111:1 8, 2004.

[15] Peter Durand Skottrup, Mogens Nicolaisen, and Annemarie Fejer Justesen. Towards on-site pathogen detection using antibody-based sensors. *Biosens. Bioelectro.*, 24:339 348, 2008.

[16] D. E. Gombas, Y. Chen, R. S. Clavero, and V. N. Scott. Characterization of monoclonal antibodies specific for the human growth hormone 22 k and 20 k isoform. *Journal of Food Protection*, 66(4):559 569(11), 2003.

Chapter 5

Genomic application: oligonucleotide detection

> "RNA cannot be longer regarded as a simply DNA-to-protein intermediate. There is another level of information, transacted by RNA, which in turn implied the evolution of a much more sophisticated regulatory system and a huge increase in the amount of regulatory information in more complex organisms."
>
> *John S. Mattick. Deconstructing the dogma.*

5.1 Introduction

5.1.1 Oligonucleotide detection

Nucleic acids are biological molecules essential for life that include DNA and RNA. They consist of two long polymers of simple units called nucleotides with backbones made of sugar and phosphate groups joined by ester bonds (see Figure 5.1). Attached to each sugar is one of four types of molecules called nucleobases, they provide the molecular structure necessary for the hydrogen bonding of either complementary DNA or RNA and its strands. An important property of

DNA is that it can replicate, or make copies of itself. DNA is always located in the nucleus of the cell and is formed by desoxyribose sugar and four different bases; A, T, C, and G. RNA is located in the nucleus and the cytoplasm and is formed by ribose sugar and the same base as DNA but where T is replaced by U.

Nowadays, single nucleotide strands can be designed and commercially obtained containing the nucleotide sequence desired in order to interact with the complementary target sequence of interest. Single-stranded DNAs or RNAs can bind to their complementary strands with high specificity and are useful for nucleic acid detection in a process named hybridization. Current methods to detect oligonucleotides consist of amplification of the sample by polymerase chain reaction (PCR), electrophoretic techniques for the separation of complex mixtures, and the final detection and quantification by labeled techniques (usually fluorescence). These techniques imply the pretreatment of the sample, the use of different and complex instruments, and the specialized training of the user enlarging the cost and the analysis time.

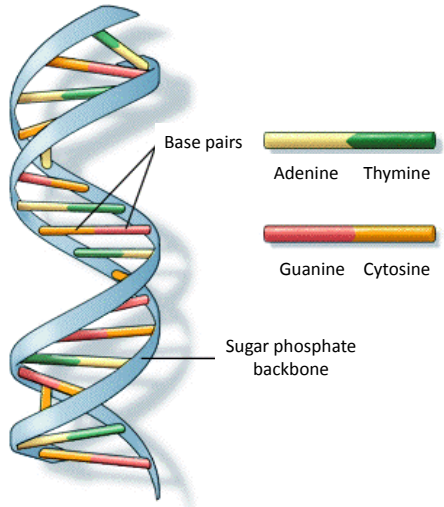

Figure 5.1: DNA is a double helix formed by base pairs attached to a sugar-phosphate backbone

Nevertheless, optical biosensing techniques provide the monitoring of biomolecular interactions in real-time without any labeling. Using SPR methods, sub-

nanomolar detection for DNA targets [1], including the identification of single mismatches [2], have been reported. RNA biosensing is much less widespread than DNA, not only due to the complexity of detecting a specific RNA sequence in a complex matrix containing hundreds of other RNA sequences but also for the frequent presence of secondary structures. While the detection of short RNA sequences has been demonstrated by SPR [3], detection of longer RNA sequences is not straightforward mainly due to the abundance of different folding structures which RNA can adopt. For that, our group has implemented a novel detection method based on the RNA recognition through the formation of a triplex helix and employing an SPR sensor for the analysis [4]. These techniques allow the immobilization of the oligonucleotide bioreceptor sequence to the sensor area surface without modifying it neither the analyte. Then, the complementary sequence is detected without further preparation, saving time and cost in comparison with standard techniques.

In the detection of oligonucleotide by , the oligonucleotides are directly immobilized on the transducer surface and the complementary sequence is directly detected without further preparation, saving time and cost in comparison with current techniques.

5.2 Detection of the alternative splicing of the Fas gene

The general assumption is that DNA holds the key of genetic contribution whereas RNA is considered a simple messenger or intermediate. However, recent evidences state that less than 5% of our genome output is transcribed into proteins. The remaining output is transcribed into non-coding RNA, suggesting that it may have undiscovered functions [5]. Hence, the DNA information is transcribed into RNA, which can be either employed for transcription of proteins or to coordinate a sophisticated regulatory system to control cell functions. The increasingly role of RNA as a key regulatory component of DNA information [5] opens a new range of possibilities for biomedical research. The mechanisms implicated in the transcription of information into RNA are amazingly variable. Any given RNA sequence contains the recipe for the production of many different proteins with different functions. The final protein output is determined by a process called alternative splicing [6, 7].

In eukaryotic cells, genes consist of sequences formed by codifying DNA named exons that are alternated with non-codifying sequences named introns.

Once a gene is transcribed into a pre-mRNA, the intronic fragments are efficiently removed and exons are re-joined together. The rearranged exons configure the mature mRNA, to be translated into the final protein, and the free introns carry out other regulatory functions in the cell [5]. Additionally, the alternative splicing provides the cell with the capacity of producing different protein versions by reorganizing the number of exons. The different protein isoforms, may have different functions (sometimes even contrary to the original one). The proportion between the transcribed RNA isoforms depends on the surrounding environment providing the cell with the ability to adapt itself to the changing external medium. This post-transcriptional event takes place in more than 95% of human genes [7], promoting a higher diversity of proteins with a lower number of genes. Deeper studies must be carried out to clarify the mechanism that regulates this process, contributing to the understanding of many genetic diseases.

The alteration of the splicing process can cause dramatic effects in the organism. This is the case of the regulation of apoptosis (programmed cell death) that has an important role in the development and progression of cancer. The alternative splicing of the gene Fas (also called CD95 and APO-1) results in either anti- or a pro-apoptotic isoforms depending on whether the Fas exon 6 is included or skipped [8, 9]. When the mature RNA contains exons 5 and 7 but does not contain exon 6 (57 isoform), it results in a soluble extra-cellular protein which prevents the cell to undergo apoptosis. On the other hand, the isoform containing exon 6 (567 isoform) results in a transmembrane protein that allows the cell to trigger the apoptosis process in the presence of the appropriate stimuli. A schematic representation of this process is shown in Figure 5.2.

The participation of Fas in apoptosis or programmed cell-death routes has dramatic consequences in many biological processes such as carcinogenesis, tumor outgrowth, and metastasis [10 13]. When splicing is altered, it can lead to loss of functional 567 isoform and/or low 567 isoform levels which have been demonstrated to result in aggressive tumor phenotypes since they become apoptosis-resistant [10, 14]. This entails very harmful consequences as a negative response to chemotherapy that becomes ineffective to kill the tumor cells [13, 14]. These issues make the RNA produced by the alternative splicing an interesting target for the development of biosensing strategies with potential application in cancer therapy, such as the classification of patients according to their Fas alternative splicing status to reach a personalized and more effective therapy.

Several techniques for the detection of alternative splicing have been already developed such as the splicing-sensitive microarrays [13, 15]. Other methods

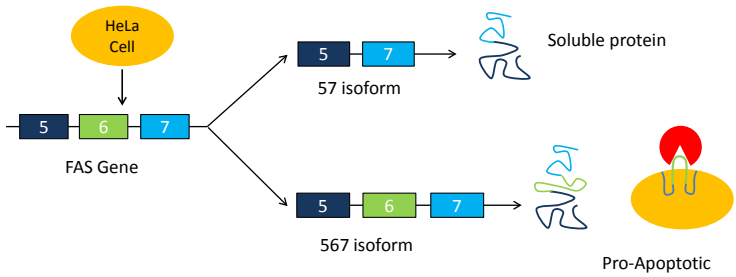

Figure 5.2: Scheme of alternative splicing process for Fas gene. The alternative splicing gives place to two different isoforms, the 567 isoform that has a pro-apoptotic function and the 57 isoform, a soluble protein.

such as crosslinking and immunoprecipitation techniques have allowed to observe the association of some regulation factors to specific RNA sequences in vivo and to determine the complete RNA sequence involved [16]. At the same time, mass-spectrometry techniques [17] have been used to quantify the different isoforms produced. All these methods have provided a strong global knowledge of the splicing process, highlighting its importance in the role of cell development, but those suffer from several drawbacks for diagnosis applications. They normally require the use of labels for the detection, very long analysis times, and they are complex and expensive. In the case of microarrays, a total RNA amount of 50-200 μg is necessary for reverse-transcription to generate enough signal. RNA samples from a single cell may be analyzed with conventional arrays, but this process requires careful amplification to retain original transcription proportions. Hybridization can take from 4 h to 24 h, and usually a thermal step is important for background reduction. In these techniques, results are generally described as a ratio of experimental target relative to a reference sample, rather than being quantitative [18]. Therefore, the development of a methodology based on biosensing platforms seems to be very appealing in contrast with current techniques.

In this chapter, we present the preliminary results obtained for the label-free detection of the two isoforms from the alternative splicing of Fas gene using the BiMW device. The receptor SH-modified sequences are separately immobilized in different fluidic channels of the chip. The attachment of the bioreceptors on the sensor area surface is achieved by a covalent disulfide bond between the

SH-modified oligonucleotide receptors and the previously thiolated sensor areas. The selectivity problems derived from the similarity of both isoforms are solved by using hybridization conditions that reduce the signal given by the target bound with lower affinity.

5.2.1 Materials and Methods

Reactives. Components of the saline sodium citrate buffer (SSC 5×; 0.75 M NaCl, 0.075 M sodium citrate) and phosphate buffer (PB; 50 mM phosphate, 0,5 M NaCl, pH = 7), formamide, and 6-mercapto-1-hexanol (MCH) were purchased from Sigma-Aldrich, Germany. The SH-modified oligonucleotides receptor sequences used in this experiment, summarized in Table 5.1, were purchased from IBA GmbH, Germany. Receptor sequences were designed to specifically match the Fas RNA isofoms by targeting their splicing junctions. Both oligonucleotide receptors consist of a region complementary to exon 5 while the other portion either matches with exon 6 (56-receptor) or exon 7(57-receptor). To improve target accessibility, a poly-timine sequence of 15 nucleotides (T15) has been added to the receptor sequence, working as a vertical spacer that separates the matching receptor sequence away from the surface (HS-T15-Oligo) [2]. In addition, a thiol group was incorporated at the 5' end allowing their immobilization.

Receptor	Sequence
SH-57	5'SH-(T_{15})-AGATCTGGATCCTTCCTCTTTG 3'
SH-56	5'SH-(T_{15})-CTTTCTCTTCACTTCCTCTTTG 3'

Table 5.1: Nucleotic sequences of receptors. The different exons are pointed out by the use of different colors, exons 5, 6, and 7 are represented by green, red, and blue, respectively.

The use of RNA samples to perform the calibration curves of the device has some inconvenient, such as the easy degradation of the RNA due to the presence of RNAsas. On the other hand, the scarce amounts of RNA obtained from cell cultures increase the cost of the experiments. The use of synthetic oligonucleotide target sequences designed to be equivalent to the corresponding mRNA isoform sequences entails a markedly advantage due to its larger stability and limitless quantity. Thus, commercial DNA sequences, summarized in Table 5.2, were employed as target instead of RNA samples for these experiments and they were also purchased from IBA GmbH, Germany.

Target	Sequence
T-57	5'ATGTGAACATGGAATCATCAAGGAATGCACACTCACCAG CAACACCAAGTGCAAAGAGGAAGTGAAGAGAAAGGAAGT ACAGAAAACATGCAGAAAGCACAGAAAGGAAAACCAAGG TTCTCATGAATCTCCAACTTTAAATCCT3'
T-567	5'ATGTGAACATGGAATCATCAAGGAATGCACACTCACCAG CAACACCAAGTGCAAAGAGGAAGGATCCAGATCTAACTTG GGGTGGCTTTGTCTTCTTCTTTTGCCAATTCCACTAATTG TTTGGGTGAAGAGAAAGGAAGTACAGAAAACATGCAGAA AGCACAGAAAGGAAAACCAAGGTTCTCATGAATCTCCAA CTTTAAATCCT3'

Table 5.2: Nucleotidic sequences designed as target units for the experimental detection process. The different exons are pointed out by the use of different colors, exons 5, 6, and 7 are represented by green, red, and blue, respectively.

Biofunctionalization procedure. Silanization of the Si_3N_4 sensor area surface was performed with the MPTS silane using the protocol previously explained . Once silanized, the chip is mounted in the setup and measurements are performed in situ using the microfluidic cell. For detection of the two Fas gene splicing isoforms, we use two separate channels, each specifically biofunctionalized for targeting each isoform, as illustrated in Figure 5.3. Biofunctionalization was carried out by flowing a mixture of the corresponding oligonucleotide receptor and mercaptohexanol (MCH) over the sensor area. The MCH is a lateral spacer incorporated at the immobilization process to avoid physical adsorption phenomena and to increase target accessibility. This molecule favors the upright orientation of the receptor and controls the DNA immobilization density. MCH has been widely described in the literature [19, 20] to largely improve hybridization in biosensors. MCH backfills spaces between immobilized receptors thereby decreasing unspecific interactions and rising-up the nucleotide sequences of the immobilized receptors. The adequate concentration of the MCH spacer that maximizes the target signal was found at 50 nM. Accordingly, SH-57 and SH-56 oligonucleotide receptors are prepared at 1 μM concentration in PB buffer and 50 nM of MCH. Then, each receptor solution is flowed onto a separated channel at 5 μl/min in a continuous running water.

Experimental procedure. Synthetic DNA targets designed with the same sequence of the natural RNA targets were employed to develop a proof-of-

concept of the application. Oligonucleotide target sequences were prepared in SSC 5× buffer containing a 40% of formamide. To avoid that the signal due to bulk refractive index changes hides the hybridization event, SSC 5× with 40% of formamide was also used as running buffer. Formamide is a destabilizing agent that lowers the melting temperature of hybrids, which contributes to a reduction of nonspecific hybridization by increasing the stringency of the probe. Formamide competes with the nucleotide bases in the formation of hydrogen bonds, destabilizing the second structure. Thus, formamide increases the specificity and selectivity of the detection diminishing the cross-reactivity of the isoform that will interact with lower affinity with a given receptor. Formamide prepared at 35% in pure water is also used for regenerating the surface. In this way, the destabilizing effect of the formamide is reinforced with the denaturing effect of pure water, leading to a powerful regeneration cocktail. All the detections and regeneration processes were carried out at a velocity of 20 μl/min.

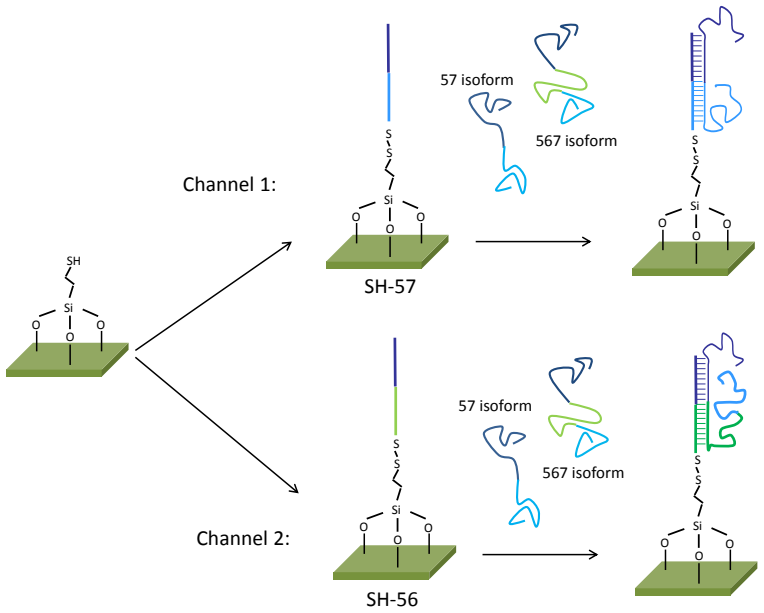

Figure 5.3: Scheme for the designed strategy for the quantitative detection of the two splicing isoforms of the FAS gene. Channel 1 is functionalized with the SH-57 receptor while channel 2 is functionalized with the SH-56 receptor. Then, both target sequences (T-567 and T-57) are separately detected at each channel.

5.2.2 Results

The suitability of the BiMW device for the DNA hybridization has been investigated by the quantification of both isoforms of the Fas gene. The difficulty that entails the differentiation and quantification of the two target isoforms is due to both of them are sharing two of their three exon sequences (exons 5 and 7). The only non-shared region is the exon 6, which is only present in the 567 isoform. Thus, cross-talk hybridization events may occur when individual detection of each isoform is intended. Previous experiments showed that cross-talk reactions were very large, and the introduction of the denaturing formamide agent (H-CO-NH_2) at the hybridization process strongly contributed in decreasing unspecific detections.

The strategy chosen to perform the Fas isoforms detection is based on the

in-situ immobilization of both receptors in different channels and the direct detection of the target oligonucleotides. The covalent attachment of the designed receptor oligonucleotides is monitored in real-time by the interferometric signal of the BiMW device, shown in Figure 5.4.

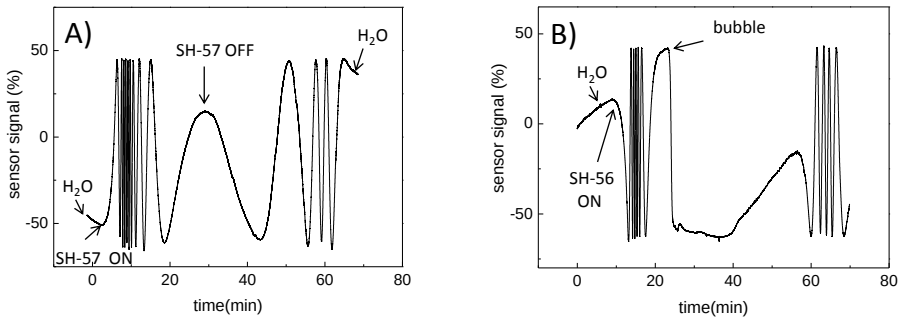

Figure 5.4: Interferometric signal for the covalent attachment of SH-57 and SH-56 to the MPTS silanized sensor area. A) Signal for the covalent attachment of SH-57 in channel 1 and B) signal for the covalent attachment of SH-56 in channel 2.

In channel 1, where SH-57 was covalently linked, resulting $\Delta\Phi$ is $5.5\times2\pi$ rad (Figure 5.4 A) whereas in channel 2 where SH- 56 was attached and the resulting $\Delta\Phi$ is $2\times2\pi$ rad (Figure 5.4 B). The values for $\Delta\Phi$ due to the entrance and the exit in the biofunctionalization process are shown in Table 5.3. It can be observed that the reaction times employed for the immobilization of DNA (70 min) are larger than the ones used in the case of protein or antibody immobilization (30 min). This rate variation for the in-situ immobilization is due to previously reported results that claim that the increase in the oligonucleotide immobilization time contributes to improve both sensitivity and selectivity of the detection [2].

Receptor	Channel	Entrance $\Delta\Phi$	Exit $\Delta\Phi$	Net Change $\Delta\Phi$
SH-57	1	$9.4\times2\pi$ rad	$3.9\times2\pi$ rad	$5.5\times2\pi$ rad
SH-56	2	$6.4\times2\pi$ rad	$4.4\times2\pi$ rad	$2\times2\pi$ rad

Table 5.3: Values of the obtained for the covalent attachment of SH-57 and SH-56 to the sensor surface

Bioreceptors are introduced in channels at the same concentration and velocity. Moreover, both SH-57 and SH-56 have the same number of nucleotides, that is, the same length and mass. Therefore, the same net change of $\Delta\Phi$ could be expected in monitoring the covalent attachment for each channel. Thus, the important difference in the net change of $\Delta\Phi$ that can be noted in Table 5.3 between the channels is probably due to a bubble in the fluidic channel 2 that hides the central part of the interferometric signal. Two main differences can be noted in the interferometric signal of the biofunctionalization process of oligonucleotides in comparison with those obtained for proteins or antibodies, i) net changes are smaller due to the smaller size of the oligonucleotide receptor (10 KDa) in comparison with proteins (50 KDa) and ii) desadsorption process has been avoided probably due to the formation of a compact and stable oligonucleotide monolayer induced by decreasing the flow velocity of the receptors.

A calibration curve is elaborated for both receptor monolayers, SH-57 in channel 1 (Figure 5.5) and SH-56 in channel 2 (Figure 5.6). Due to the low concentrations detected, regeneration of the sensing surface is performed at the end of each calibration curve instead of after each measurement. Furthermore, the integrity of the bioreceptor layer is preserved by this way. Formamide 35% in water gives a high change in the bulk refractive index as is shown in Figure 5.7, due to this, the fluidic circuit must be carefully cleaned prior to the next detection. Excellent sensitivities and minimum cross-talk reaction have been obtained, the minimum concentration (100 pM) improves by two orders of magnitude with regard to the study performed with a home-made SPR system (LOD: 10 nM). This value is very close to the best detection limit reported in the literature f

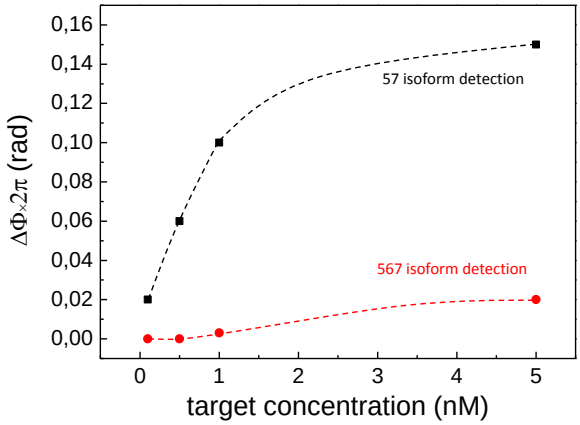

Figure 5.5: Calibration curve for SH-57 receptor in channel 1 of T57 (black line, squares) and T567 (red line, circles) isoforms. Lines are a guide for the eye.

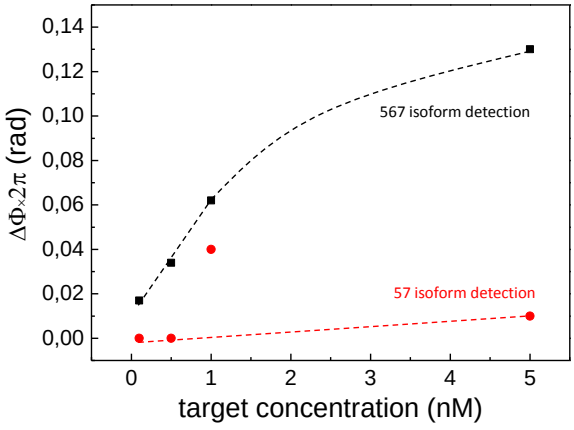

Figure 5.6: Calibration curve for SH-56 receptor in channel 2 of T567 (black line, squares) and T567 (red line, circles) isoforms. Lines are a guide for the eye.

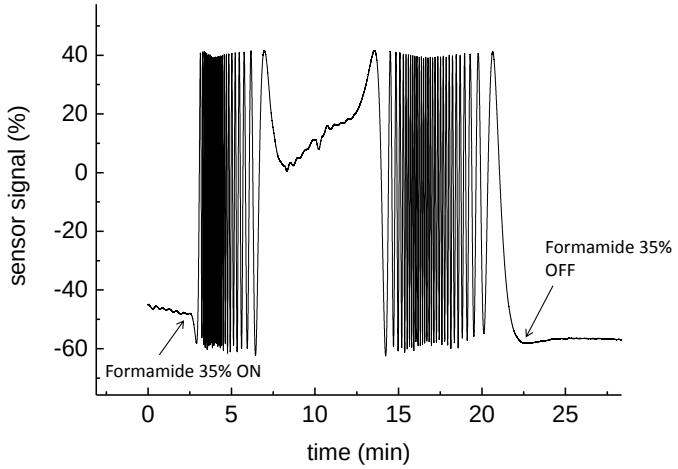

Figure 5.7: Regeneration signal of the oligonucleotide bioreceptor layer by the use of formamide 35% in water.

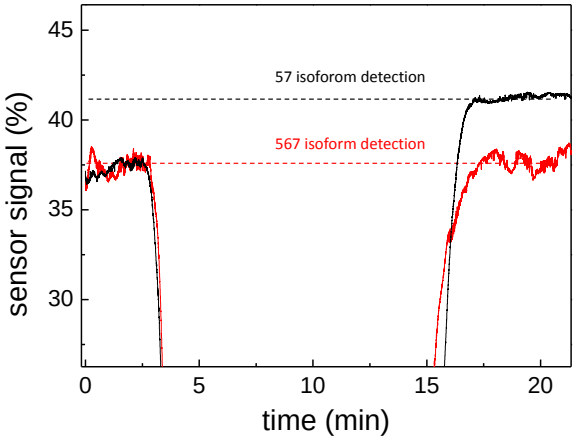

Figure 5.8: Specific detection of T57 isoform (black line) in comparison with unspecific detection of T567 isoform (red line) for receptor SH-57 in channel 1.

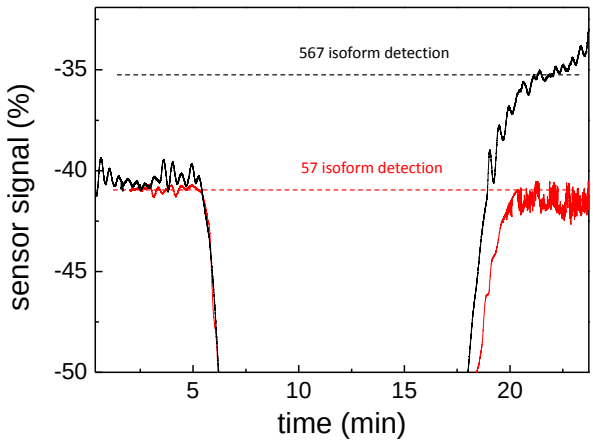

Figure 5.9: Detection of a concentration of 100 pM for specific T56 isoform in comparison with unspecific detection of T567 isoform for receptor SH-56 in channel 2.

or label-free oligonucleotide detection by a MZI biosensor developed in our group (10 pM) [21]. Real-time interferometric signals of the lowest detected concentrations (100 pM) are shown to compare specific and non-specific target signals, for the SH-57 receptor in channel 1 (Figure 5.8) and for the SH-56 receptor in channel 2 (Figure 5.8). High differences between specific and unspecific signals have been shown even for the lowest detected concentration, demonstrating the efficiency of the use of formamide as denaturing agent.

5.3 Conclusions

We have developed a BiMW biosensor to detect the two isoforms generated from Fas pre-RNA alternative splicing. The specific oligonucleotide sequences for each isoform have been immobilized on different sensor area surfaces. Due to the similarity of both RNA isoform sequences, the strategy has been focused on the quantification of each isoform avoiding cross-talk processes by the modification of hybridization conditions. Results indicate that detection of both isoforms was selective enough to perfectly distinguish them even at the lowest concentration tested. The minimum concentration of specific detected has been 100 pM. Although detected targets were synthetic oligonucleotide sequences, the final aim of this application is the detection of real samples of Fas pre-RNA

isoforms. Moreover, this configuration may expand to the detection of other splicing isoforms originated from other gene pre-RNA sequences and can be a useful tool for the prediction of diseases caused by alternative splicing.

Bibliography

[1] Yong-Jun Li, Juan Xiang, and Feimeng Zhou. Sensitive and label-free detection of DNA by surface plasmon resonance. *Plasmonics*, 2:79 87, 2007. 10.1007/s11468-007-9029-8.

[2] L. G. Carrascosa, A. Calle, and L. M. Lechuga. Label-free detection of DNA mutations by SPR: application to the early detection of inherited breast cancer. *Anal Bioanal Chem*, 393:1173 1182, 2009.

[3] Hana S?i?pova?, Shile Zhang, Aime?e M. Dudley, David Galas, Kai Wang, and Jir?i? Homola. Surface plasmon resonance biosensor for rapid label-free detection of microribonucleic acid at subfemtomole level. *Analytical Chemistry*, 82(24):10110 10115, 2010.

[4] Laura G. Carrascosa, S. Gomez-Montes, A. Avino, A. Nadal, M. Pla, R. Eritja, and L. M. Lechuga. Sensitive and label-free biosensing of RNA with predicted secondary structures by a triplex affinity capture method. *Nucleic Acids Res.*, 2012. Advanced access.

[5] John S. Mattick. Deconstructing the dogma. *Annals of the New York Academy of Sciences*, 1178(1):29 46, 2009.

[6] Eric T. Wang, Rickard Sandberg, Shujun Luo, Irina Khrebtukova andLu Zhang, Christine Mayr, Stephen F. Kingsmore, Gary P. Schroth, and Christopher B. Burge. Alternative isoform regulation in human tissue transcriptomes. *Nature*, 456:470 476, 2008.

[7] Qun Pan, Ofer Shai, Leo J Lee, Brendan J Frey, and Benjamin J Blencowe. Deep surveying of alternative splicing complexity in the human transcriptome by high-throughput sequencing. *Nature Genetics*, 40:1413 1415, 2009.

[8] Ruberti G, Cascino I, Papoff G, and Eramo A. Alternative pre-mRNA splicing and regulation of programmed cell death. *Adv Exp Med Biol.*, 406:125 134, 1996.

[9] Peter H. Krammer. CD95(APO-1/Fas)-mediated apoptosis: Live and let die. *Advances in Immunology*, 71:163 210, 1998.

[10] Owen-Schaub L, Chan H, Cusack JC, Roth J, and Hill LL. Fas and Fas ligand interactions in malignant disease. *International Journal of Oncology*, 17(1):5 12, 2000.

[11] O'Connell J, Bennett MW, O'Sullivan GC, Collins JK, and Shanahan F. The Fas counterattack: cancer as a site of immune privilege. *Immunol Today.*, 20(1):46 52, 1999.

[12] L. M. Butler, P. J. Hewett, W. J. Butler, and P. A. Cowled. Down-regulation of Fas gene expression in colon cancer is not a result of allelic loss or gene rearrangement. *Br J Cancer.*, 77(9):1454 1459, 1998.

[13] Heather L Maecker, Zhong Yun, Holden T Maecker, and Amato J Giaccia. Epigenetic changes in tumor Fas levels determine immune escape and response to therapy. *Cancer Cell*, 2(2):139 148, 2002.

[14] Laurie B. Owen-Schaub, Kenneth L. van Golen, Laurie L. Hill, and Janet E. Price. Fas and Fas ligand interactions suppress melanoma lung metastasis. *JEM*, 188(9):1717 1723, 1998.

[15] Miroslava Cuperlovic-Culf, Nabil Belacel, Adrian S. Culf, and Rodney J. Ouellette. Microarray analysis of alternative splicing. *OMICS*, 10(3):344 357, 2006.

[16] Donny D. Licatalosi, Aldo Mele, John J. Fak, Jernej Ule, Melis Kayikci, Sung Wook Chi, Tyson A. Clark, Anthony C. Schweitzer, John E. Blume, Xuning Wang, Jennifer C. Darnell1, and Robert B. Darnell. Hits-clip yields genome-wide insights into brain alternative rna processing. *Nature*, 456(3):464 469, 2008.

[17] Stephen Tanner, Zhouxin Shen, Julio Ng, Liliana Florea, Roderic Guigo, Steven P. Briggs, and Vineet Bafna. Improving gene annotation using peptide mass spectrometry. *Genome Res.*, 17(2):231 239, 2008.

[18] Wenonah Vercouterea and Mark Akesonb. Biosensors for DNA sequence detection. *Current Opinion in Chemical Biology*, 6(6):816 822, 2002.

[19] Laura G. Carrascosa, Lidia Mart nez, Yves Huttel, Elisa Roman, and Laura M. Lechuga. Understanding the role of thiol and disulfide self-assembled DNA receptor monolayers for biosensing applications. *Eur Biophys J*, 119:1433 1444, 2010.

[20] Tonya M. Herne and Michael J. Tarlov. Characterization of DNA probes immobilized on gold surfaces. *J. Am Chem. Soc.*, 119(38):8916 8920, 1997.

[21] J. Sanchez del R o, L.G. Carrascosa, F.J. Blanco, M. Moreno, J. Berganzo, A. Calle, C. Dom nguez, and L. M. Lechuga. Lab-on-a-chip platforms based on highly sensitive nanophotonic Si biosensors for single nucleotide DNA testing. *Proc. of SPIE*, 6477:64771B1 64771B9, 2007.

Chapter 6

Future perspectives: towards the lab-on-a-chip device

One of the main limitations for achieving truly lab-on-a-chip (LOC) devices for point-of-care diagnosis is the incorporation of the "on-chip" detection. Although optical sensors based on evanescent fiel meet all the required characteristics to be integrated in a LOC device, very few stand-alone LOC platforms based on these sensors have emerged. Indeed, the transit from bulky and complex laboratory equipment to a small, portable and cheap LOC device with low consumption remains a challenge: even if the technologies for each component are mature, their integration into a single platform is complex. The device must be carefully designed since it is not merely the sum of the basic units [1].

One key issue in the development of LOC devices is the way to bring the sample in contact with the sensing area. The volume of the sample and the flow rate are critical parameters, especially for clinical testing where it is extremely important to reduce the sample volume. Recent technological efforts to combine the fields of photonics and microfluidics have led to the development of optofluidics, in which optical and fluidic systems are integrated together to provide improved functions and performances. The interest in this field is demonstrated by the increasing number of papers and reviews published over the last few years [2, 3].

In the case of evanescent wave sensors, the way to couple light into the WG is another critical aspect since an efficient coupling increases the sensitivity of the device through an improved signal-to-noise ratio. Common in-coupling techniques are the end-fired method, the prism coupling and the grating assisted coupling, the last one being the most suitable for future commercial devices as it provides better integration and stability. However, very few works have demonstrated the applicability of evanescent wave sensors incorporating grating couplers, especially in the visible range. An exception is with the multiplexed ring resonator array integrated with microfluidics and grating couplers developed by Carlborg et al [4] or the grating coupled with a waveguide interferometer recently optimized by Kozma et al. [5]. An important drawback of interferometric sensors comes from the periodic nature of the output signal which can give rise to wrong or ambiguous interpretations. This problem can be solved by implementing a phase modulation system.

However, when dealing with a biosensor LOC system, the first issue to solve is the choice of the transducer. The BiMW device meets all the required characteristics to be integrated in a LOC platform as they offer minituarization and the possibility of mass-production besides high sensitivity. In this context, we present our first steps towards the achievement of a portable LOC platform by using the BiMW device. The total biosensor system using the BiMW device (see Figure 6.1) is conceived by integrating the following parts: i) the transducer in a multiplexed configuration, ii) the flow cell and the flow delivery system (microfluidics), iii) a phase modulation system to convert the periodic interferometric signals into direct phase measurements, and iv) the light sources and photodetectors.

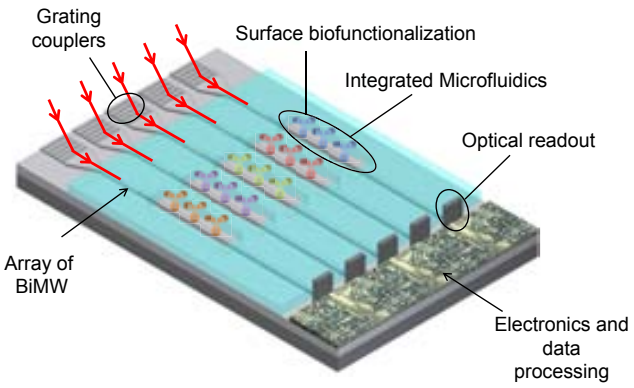

Figure 6.1: Scheme of our envisioned lab on a chip platform, with integrated interferometers array, microfluidics, grating couplers, optical detectors, and electronics.

The coupling of light into a waveguide is an important issue to solve when dealing with LOC based on evanescent wave sensors. Our solution is to integrate **grating couplers** at the input of the BiMW interferometers, making feasible better integration, stability and alignment tolerance when compared to the traditional end-fire method. Moreover, when coupling light with gratings, no polishing of the chip edges is required. Due to the sub-micronic cross-section of the BiMW transducer and to the operating wavelength (λ = 658 nm), the grating length cannot exceed 100 mm with a sub-micronic period which makes it suitable for high scale integration. To increase the coupling efficiency, the grating is associated to a tapered waveguide with an initial width of 20 mm that linearly reduces until reaching the BiMW width (4 μm). The gratings are directly written onto the Si_3N_4 waveguide by electron beam lithography and reactive ion etching processes. A grating written onto an interferometer (width ranging from 20 to 50 μm) is shown in Figure 6.2 A and an excited grating coupling light into a BiMW device at λ = 633 nm is shown in Figure 6.2 B. In Figure 6.2, it can be seen a scanning electron image of a grating with a period of 400 nm and with a duty cycle of 0.5 and a depth of 40 nm (total dimensions: 50 μm$\times$50 μm).

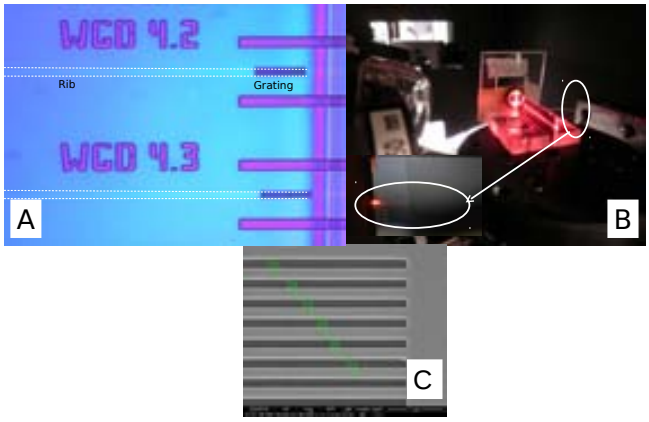

Figure 6.2: A) Optical microscope image of grating couplers fabricated on rib waveguides, B) image of light coupled to a BiMW by grating coupling ($\theta_{exc} = 9.15°$) for TE polarization), and C) Scanning electron microscope image of a grating.

Another issue to take into account is the cosine dependence of the interferometric signal, the response of interferometric sensors is affected by intrinsic problems that can be resumed in i) sensitivity fading, ii) signal ambiguities, and iii) intensity variations. Different solutions have been proposed to solve this problem. The most common involve the use of electro-optic [6], acousto-optical [7], or magneto-optical [8] working principles. However these techniques generally involve non-standard CMOS materials and rely on complex read-out equipment which clearly impedes their integration into LOC platform. To overcome these difficulties, we have recently proposed a new all-optical **modulation** approach which provides a real-time and direct read-out of the phase variation without additional fabrication processes and instrumentation [9]. We have expanded this idea to the BiMW sensors.

In this modulation scheme, the phase difference between the two modes propagating in the BiMW is controlled by tuning the input wavelength of the guided light by a few nanometers. According to our calculations, a wavelength variation of 2 nm is enough to induce a shift of 2 π rad between the two modes. This wavelength variation is easily obtained by taking advantage of a drawback of the commercial Fabry Perot laser diodes, i.e. the dependence of their emis-

sion wavelength with the driving current. Therefore, by applying a sinusoidal variation to the laser driving current, it is possible to induce a periodic phase change in the waveguide.

It can be demonstrated that the phase change induced by a surface modification on the sensor area can be extracted from the inverse tangent of the ratio between the third and the second harmonics of the output signal. In Figure 6.3 the signal response of a phase modulated BiMW can be observed for a concentration of 0.2 M, obtaining a $\Delta\Phi = 3.84{\times}2\pi$ rad. Figure 6.3 A represents the individual response of both harmonics while in Figure 6.3 B the unwrapped phase signal can be observed.

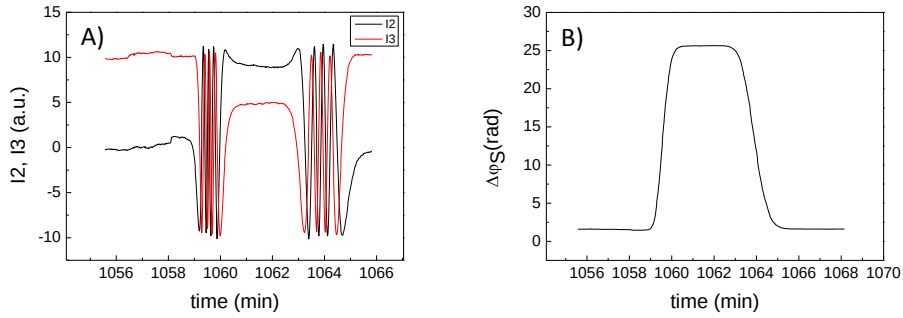

Figure 6.3: Signal response for 0.2 M HCl solution of a phase modulated BiMW device. A) Second and third harmonics of the detection and B) the inverse tangent of the ratio between both harmonics.

To enhance the performance of LOC biosensor, the detection of several analytes at the same time from a single sample is an important requirement. For this reason, **multiplexed sensing platforms** have to be implemented, to be sensitive to a broad spectrum of targets at the same time, in a compact structure, and by using the smallest amount of reagents possible.

Different solutions can be adopted to implement a performing multiplexed device. For example, in the case of our interferometric devices different cases can be distinguished: i) a single laser source scanning sequentially all the devices under test, ii) a multiple laser source approach, in which each interferometer has its own light source as we can see in Figure 6.4 A (that can be external to the chip, e.g. array of fibers or integrated, e.g. VCSELs) or, iii) a single input

source splitting into the different elements at wafer level as see in Figure 6.4 B (integrated beam splitters).

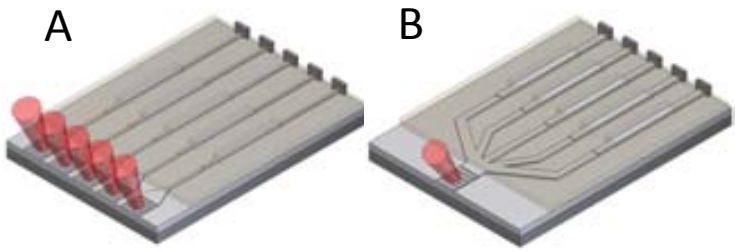

Figure 6.4: Sketch of different approaches for the multiplexing implementation in the case of BiMW device, A) each interferometer has its own light source and B) a single input source is splitted towards each interferometer.

One key issue in the development of a LOC biosensor detection is the way to bring the sample in contact with the sensing area. The volume of the sample and the flow rate are critical parameters, especially for clinical testing, where it is extremely important to reduce the sample volume as much as possible in order to increase the efficiency of the detection. **Micro uidics network** plays a fundamental role when implementing a multiplexed structure. Then, the size of the channels network, their design, fabrication, connection and alignment to the sensor area will be critical steps.

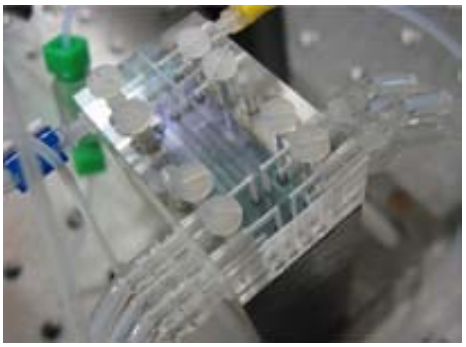

Figure 6.5: Complete fluidic platform picture, with external PMMA housing, connections and integrated polymeric microfluidics layer.

The microfabrication technique to generate the microchannels onto the interferometer devices developed by our group is based on two photolithographic patterned SU-8 polymeric resist layers on separate wafers. One of the wafers contains the interferometric devices, and the other one is a temporary top substrate. SU-8 from both wafers is bound and the temporary wafer is released. In this way 3-Dimensional microchannels are obtaining and vertical sidewalls for the channels are ensured [10]. The advantages of this approach can be found in the large alignment tolerance during fabrication and in the compatibility with further fabrication steps. . A PMMA housing provides connection to the macroworld and ensures robust leakage-free flow operation of the devices (see Figure 6.5). This macro-microfluidic module can operate at pressure drops up to 1000 kPa. With this integrated microfluidic layer on top of a MZI chip, a bulk refractive index detection limit of 3.8×10^{-6} RIU was obtained [10], demonstrating the success of the integration.

The integration of the BiMW biosensor with a microfluidic polymeric network at the wafer level is carried out using CMOS compatible processes. The channels measure 50 μm in height, 100 μ m in width, and 1.5 cm in length to ensure a long interaction length for the analyte on the sensing area of the interferometer. The mask for the microfabrication process can be seen in Figure 6.6.

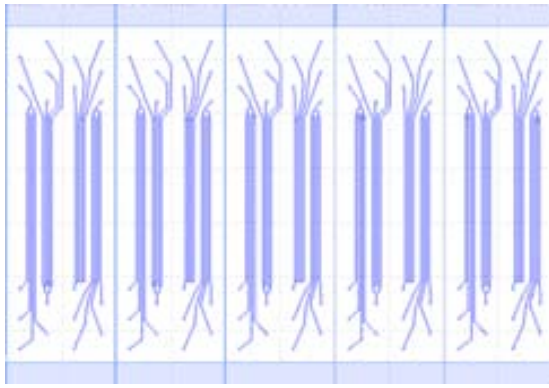

Figure 6.6: Mask for the microfluidics implementation of the BiMWs.

The complete integration is not trivial, since many requirements must be carefully considered. The elements of the array must be independent, not interfering among them, but must be subjected to the same variations with external agents (e.g. temperature). Furthermore, a proper sample delivery system (microfluidics) is required and a suitable detection method for multiple signal acquisition is of vital importance. In conclusion, a preliminary approach to a complete lab-on-a-chip device based on a novel two-mode interference device has been presented in this chapter. The suitability of the transducer for its integration in a LOC device has been demonstrated by the measurements obtained for the gratings couplers and for the modulation system [11]. The detection limits achieved by the transducer in these steps of the integration process are quite similar to the ones achieved for the BiMW device without any implementation. These are very promising results to develop a high sensitive lab-on-a-chip device by employing a BiMW transducer.

Bibliography

[1] F. S. Ligler. Perspective on optical biosensors and integrated sensor systems. *Anal. Chem.*, 81(2):519 526, 2009.

[2] Frank B. Myers and Luke P. Lee. Innovations in optical microfluidic technologies for point-of-care diagnostics. *Lab chip*, 8:2015 2031, 2008.

[3] Xudong Fan and Ian M. White. Optofluidic microsystems for chemical and biological analysis. *Nat. Photonics*, 8:2015 2031, 2011.

[4] C. F. Carlborg, K. B. Gylfason, A. Kazmierczak, F. Dortu, M. J. Ba nuls Polo, A. Maquieira Catala, G. M. Kresbach, H. Sohlstrom, L. Vivien T. Moh, J. Popplewell, G. Ronanandez C. A. Barrios, G. Stemme, and W. van der Wijngaart. A packaged optical slot-waveguide ring resonator sensor array for multiplex label-free assays in labs-on-chips. *Lab chip*, 10:281 290, 2010.

[5] Peter Kozma, Andras Hamori, Sandor Kurunczi, Kaspar Cottier, and Robert Horvath. Grating coupled optical waveguide interferometer for label-free biosensing. *Sens. Actuators, B*, 155:281 290, 2011.

[6] R. G. Heideman and P. V. Lambeck. Remote opto-chemical sensing with extreme sensitivity: design, fabrication and performance of a pigtailed integrated optical phase-modulated Mach-Zehnder interferometer system. *Sens. Actuators B*, 61(1-3):100 127, 1999.

[7] M. B. Duhring and O. Sigmund. Improving the acousto-optical interaction in a Mach-Zehnder interferometer. *J. Appl. Phys.*, 105:083529, 2009.

[8] B. Sepulveda, G. Armelles, and L.M. Lechuga. Magneto-optical phase modulation in integrated Mach-Zehnder interferometric sensors. *Sens. Actuators, A*, 134:339 347, 2007.

[9] S. Dante, D. Duval, B. Sepulveda, A. B. Gonzalez-Guerrero, J. R. Sendra, and L.M. Lechuga. All-optical phase modulation for integrated interferometric biosensors. *Opt. Express*, 20:7195 7205, 2012.

[10] F J Blanco, M Agirregabiria, J Berganzo, K Mayora, J Elizalde, A Calle, C Dom nguez, and L M Lechuga. Microfluidic-optical integrated CMOS compatible devices for labe-free biochemical sensing. *J. Micromech. Microeng.*, 16:1006 1016, 2006.

[11] Daphne Duval, Ana Belen Gonzalez-Guerrero, Stefania Dante, Johann Osmond, Rosa Monge, Luis J. Fernandez, Kirill E. Zinoviev, C Dom nguez, and L M Lechuga. Nanophotonic lab-on-a-chip platforms including novel bimodal interferometers, microfluidics and grating couplers. *Lab chip*, 12:1987 1994, 2012.

General conclusions

Simplicity means the achievement of maximum e ect with minimum means.

Albert Einstein.

In this thesis work, we have presented the development and characterization of the Bimodal Waveguide (BiMW) device based on two-mode interference. This new interferometric transducer emerges from the knowledge of our group acquired in the development of photonic waveguide devices such as the Mach-Zehnder biosensor device: although the impressive detection limits achieving by this biosensor, there is a need of a simpler interferometric configurations, compatible with the precision and reproducibility that offer actual microfabrication techniques. Thus, the research efforts of our group have led to a novel interferometric configuration based on a straight rib waveguide that avoids the Y-shape divisor of the MZI interferometer and replaces it with a modal splitter consisting in a jump in the core height of a hundred of nanometers: light propagating in a single-mode waveguide excites the first mode in coupling in a bimodal waveguide, the interference pattern of these modes will provide information about the processes occurring on the sensor area of the device. Although, previous works have demonstrated the development of devices based on two-mode interference, we have applied this principle as transduction mechanism for biosensing, for the first time.

The structure of the rib waveguide is designed by semi-analytical approximations and numerical methods in order to simulate the field profiles of the different

modes. Using the approximations, the important parameters of the layer structure (i.e. refractive index, dimensions of the rib, and the thickness of the core for the single-mode and bimodal part of the device) are calculated to obtain the required modal behavior and a high modulation of the output signal. The behavior of the light around the step junction is examined by numerical methods, evidencing low losses and the good performance of the waveguide structure.

The device has been produced using silicon-based technology which allows the processing of 200 transducers in the same wafer due to the previous experience of the group for the fabrication of waveguides. This invaluable inheritance from the MZI development has allowed the fabrication of highly reproducible nanometric rib structures, giving rise to a highly reliable devices.

Characterization of BiMW has been made by a standard optical set up including a light source, temperature controller, and photodetectors. The transport of liquid solutions to the sensor area involves the fabrication of a multichannel PDMS fluidic cell by soft-lithography that allows the measurement of 4 different devices in every chip. The detections limit demonstrated for small changes in the bulk refractive index (2.5×10^{-7} RIU) in the first stages of this work, led us to check the possibilities of the BiMW device as label-free high sensitive biosensor.

Notwithstanding, an extremely low detection limit is not the only important property that make a transducer a suitable element of a biosensor. The inertness of the surface to maintain the stability front solutions together with the enough reactivity for being chemically modified are essential requirements to obtain an stable covalent bond between the surface and the biorecetor. With this aim, silanization methods have been developed: a carboxylic-terminated silane (CTES) has been employed to immobilize proteins or antibodies to the sensor area surface and a thiol-terminated silane (MPTS) have been employed to achieve a covalent disulfide bond, between the SH-functionalized surface and a SH-modified synthetic DNA sequence used as receptor.

The first biosensing study carried out has been the evaluation of human Growth Hormone (hGH), an important biomarker for some illnesses related with the growth. The immunoassay was performed in a competitive format using monoclonal antibodies. The detection limit obtained for the detection of hGH detection was 8 pg/ml (160 fM), which overcomes the detection limits of existing methodologies in an order of magnitude and improves 1000 times the detection limit previously demonstrated by a home-made SPR device using the same

procedure. The analysis time has been reduced to a total of 13 min, a landmark for current clinical analysis that can take hours due to the amplification steps and use of additional equipments.

The device has been also tested for the detection of microorganisms by the detection of the bacterium Pseudomas aeruginosa using a direct immunoassay with polyclonal antibodies. Although culture assays are able to detect as low as one single bacterium, the technique takes days to provide the final results. Moreover, further analysis (normally immunoassays) are needed after the culture to appropriately identify the bacteria. The BiMW biosensor proposed for the detection of bacteria demonstrates an excellent response in a wide range of concentrations. The bacteria were previously deactivated by ultrasonication and thermal treatments, which break the bacteria liberating antigen and enhancing detection limits up to 10 cfu/ml. Furthermore, the specificity of the signal was very high when using Staphylococcus as control, which indicates the low cross-reactivity of the polyclonal antibody used. The extremely low detection limits obtained could situate the BiMW transducer on the top of the label-free detection techniques for pathogenic detection. In this direction, future experiments will involve the detection of entire harmless bacteria to investigate the single bacterium detection. The objective for this device is to achieve the detection limit of current culture techniques (1 bacterium) but reducing drastically the assay time to 12 min.

Finally, the selective oligonucleotide detection of the isoforms of the alternative splicing of the FAS gene has been demonstrated by the direct detection of DNA synthetic sequences equivalent to the real mRNA isoforms. The alternative splicing of this gene originates two different proteins, one induces apoptosis of the cells and the other avoids it. Alterations in the proportion of both isoforms have been related with cancer progression. Calibration curves for both isoforms have shown detection limits that improve 100 times those obtained by the SPR device for the same analytes using the same conditions, achieving the 100 pM.

The results presented in this work have highlighted the superior performance of this device in comparison with conventional diagnostics tests due to: i) the possibility of monitoring biomolecular interactions in real-time and by using a label-free scheme which reduce the time and cost of the assay, ii) the fabrication of the device using standard silicon microelectronics technology which opens the possibility for mass-production, iii) the high sensitivity demonstrated for the different bioapplications assessed achieving detection limits in the pg/ml

range (femtomolar), and iv) the device meets the specific requirements to be miniaturized and integrated in complex biosensing platforms.

The extremely low detection limits exhibited by the BiMW transducer for detection of proteins, bacteria, and DNA demonstrate that this biosensor has the appropriate characteristics to become the perfect transducer to be integrated in a lab-on-a-chip device. First work in this direction is presented, the measurements for this transducer using the gratings couplers and the modulation system have demonstrated similar sensitivity and performance than the obtained for the non-integrated transducer. The presented approach to a portable, highly sensitive, and fast detection biosensor system using a BiMW device could constitute a milestone in the development of commercially available interferometric biosensor for clinical diagnosis.